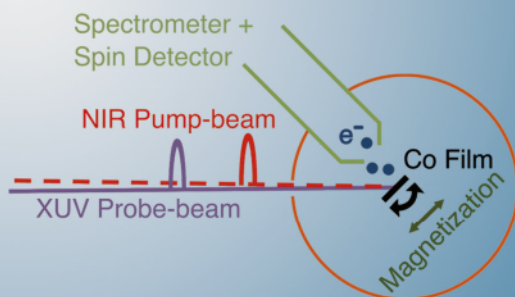
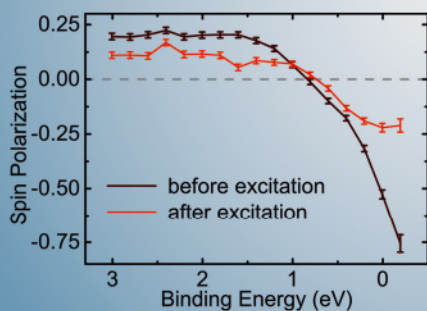
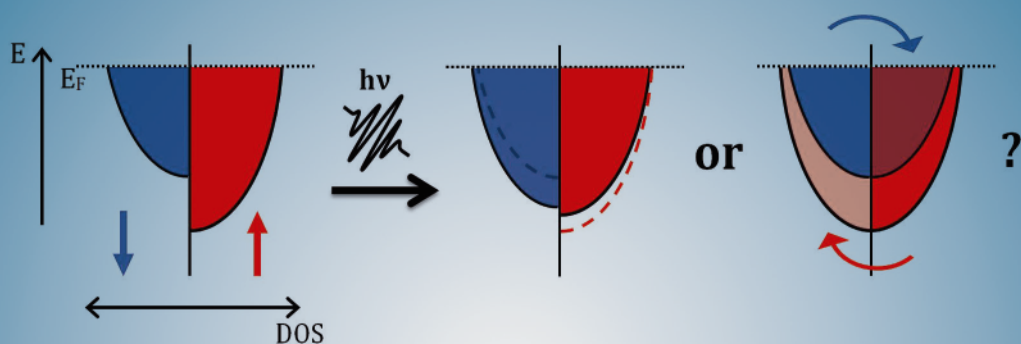


Laser-Induced Ultrafast Electron- and Spin-Dynamics in the Electronic Band Structure of Co(001)

Moritz Alexander Plötzing



Forschungszentrum Jülich GmbH
Peter Grünberg Institute (PGI)
Electronic Properties (PGI-6)

Laser-Induced Ultrafast Electron- and Spin-Dynamics in the Electronic Band Structure of Co(001)

Moritz Alexander Plötzing

Schriften des Forschungszentrums Jülich
Reihe Schlüsseltechnologien / Key Technologies

Band / Volume 131

ISSN 1866-1807

ISBN 978-3-95806-168-2

Bibliographic information published by the Deutsche Nationalbibliothek.
The Deutsche Nationalbibliothek lists this publication in the Deutsche
Nationalbibliografie; detailed bibliographic data are available in the
Internet at <http://dnb.d-nb.de>.

Publisher and
Distributor: Forschungszentrum Jülich GmbH
Zentralbibliothek
52425 Jülich
Tel: +49 2461 61-5368
Fax: +49 2461 61-6103
Email: zb-publikation@fz-juelich.de
www.fz-juelich.de/zb

Cover Design: Grafische Medien, Forschungszentrum Jülich GmbH

Printer: Grafische Medien, Forschungszentrum Jülich GmbH

Copyright: Forschungszentrum Jülich 2016

Schriften des Forschungszentrums Jülich
Reihe Schlüsseltechnologien / Key Technologies, Band / Volume 131

D 464 (Diss., Duisburg, Univ., 2016)

ISSN 1866-1807
ISBN 978-3-95806-168-2

The complete volume is freely available on the Internet on the Jülicher Open Access Server (JuSER)
at www.fz-juelich.de/zb/openaccess.



This is an Open Access publication distributed under the terms of the [Creative Commons Attribution License 4.0](https://creativecommons.org/licenses/by/4.0/),
which permits unrestricted use, distribution, and reproduction in any medium, provided the original work is properly cited.

Contents

| | |
|---|----|
| Zusammenfassung | 1 |
| Abstract | 3 |
| 1 Introduction | 5 |
| 2 Fundamental Considerations | 11 |
| 2.1 Magnetism in 3d Transition Metals | 11 |
| 2.1.1 Exchange Interaction | 12 |
| 2.1.2 Spin-Orbit Coupling | 16 |
| 2.2 Photoelectron Spectroscopy | 16 |
| 2.2.1 Three-Step Model of Photoemission | 17 |
| 2.2.2 Description within a One-Step Model | 26 |
| 2.2.3 Spin Detection of Photoelectrons | 27 |
| 2.3 Laser-Based High-Order Harmonic Generation | 32 |
| 2.3.1 Three-Step Model of High-Order Harmonic Generation | 34 |
| 2.3.2 Phase Matching Conditions | 38 |
| 2.3.3 Wavelength-Dependence of High-Order Harmonic Generation | 40 |
| 3 Experimental Setup | 43 |
| 3.1 Monochromatic Femtosecond-Pulsed Extreme Ultraviolet Light Source | 43 |
| 3.2 Experimental Chamber & Photoelectron Detection | 48 |
| 3.2.1 Spectrometer | 49 |
| 3.2.2 Spin Detector | 51 |
| 3.2.3 Sample Preparation Equipment | 53 |
| 4 Sample Preparation and Characterization: Co/Cu(001) | 55 |
| 4.1 Sample Preparation Procedure | 55 |
| 4.2 Characterization Using Photoelectron Spectroscopy | 57 |

CONTENTS

| | | |
|----------|--|---------------|
| 5 | Spin-Resolved Photoemission with Femtosecond Extreme Ultraviolet Light Pulses | 61 |
| 5.1 | Red-Driven Mode | 61 |
| 5.2 | Blue-Driven Mode | 66 |
| 5.3 | Vacuum Space-Charge Effects Induced by Extreme Ultraviolet Light Pulses | 69 |
| 6 | Towards Femtosecond Time-Resolved Photoemission | 75 |
| 6.1 | Temporal and Spatial Pump-Probe Overlap | 75 |
| 6.2 | Pump-Induced Photoelectrons & Resulting Space-Charge Contribution | 78 |
| 6.2.1 | Photoelectron Emission by Near-Infrared Light | 79 |
| 6.2.2 | Vacuum Space-Charge Contribution from Pump-Induced Photoelectrons | 84 |
| 6.3 | Temporal Stability of the Beam Positions | 91 |
| 7 | Photoemission Studies of the Electron- and Spin-Dynamics in Co During Ultrafast Demagnetization | 95 |
| 7.1 | Ultrafast Electron-Dynamics Probed with Time- and Angle-Resolved Photoelectron Spectroscopy | 97 |
| 7.2 | Ultrafast Spin-Dynamics Probed with Time- and Spin-Resolved Photoelectron Spectroscopy | 101 |
| 8 | Summary & Outlook | 107 |
| | Appendix | I |
| | List of Abbreviations | VII |
| | Bibliography | XXVI |
| | Publications and Conference Contributions | XXVII |
| | Curriculum Vitae | XXIX |
| | Acknowledgements | XXXIII |

Zusammenfassung

Obwohl auf dem Gebiet der ultraschnellen Magnetisierungsdynamik während der letzten zwei Jahrzehnte sowohl experimentell als auch theoretisch intensiv geforscht worden ist, konnte bisher keine einheitliche Erklärung des Phänomens etabliert werden. Das Ziel der vorliegenden Arbeit ist es, eine neue, tiefgehende Sichtweise auf die zugrunde liegenden Mechanismen zu ermöglichen, indem die Spin-Dynamik direkt in der elektronischen Bandstruktur beobachtet wird. Dies geschieht mittels zeit- und spinaufgelöster Photoelektronenspektroskopie des gesamten Energiebereichs der Valenzbänder auf einer Femtosekunden-Zeitskala.

Zu diesem Zweck wurde ein neuartiger Versuchsaufbau entwickelt und in Betrieb genommen. Dieser kombiniert einen hoch-effizienten Spin-Detektor mit einer modernen Labor-Lichtquelle, die ultrakurze Lichtpulse im extrem-ultravioletten (XUV) Spektralbereich generiert. Die Lichtquelle basiert auf der Erzeugung hoher Harmonischer von Laserlicht und kann auf zwei verschiedene Arten betrieben werden, um unterschiedliche Wellenlängen und Photonenflüsse bereitzustellen. In beiden Betriebsarten wurden statische, spinaufgelöste Photoemissionsspektren von Co(001) Filmen gemessen, um optimale Bedingungen für zeitaufgelöste Messungen zu finden. Weiterhin wurden Vakuum-Raumladungseffekte untersucht. Dies geschah sowohl in den dichten Elektronenwolken, die durch die ultrakurzen XUV Pulse erzeugt wurden, als auch in Bezug auf die Coulomb-Wechselwirkung zwischen dieser Elektronenwolke und Elektronen, die in Anrege-Abfrage-Experimenten durch nah-infrarote (NIR) Anrege-Pulse ausgelöst werden. Dadurch konnte der Einfluss dieser Effekte auf Photoemissionsspektren ermittelt und später minimiert werden.

Die NIR Anrege-Pulse wurden im Weiteren in zeitaufgelösten Messungen eingesetzt, um eine ultraschnelle Demagnetisierung in Co Filmen einzuleiten. Mit Hilfe unseres neuen Experiments konnten wir den zeitlichen Verlauf der Elektronendynamik verfolgen, indem spinaufgelöste Spektren über einen breiten Energiebereich, der die Valenzbänder vollständig einschließt, aufgezeichnet wurden. Solche Messungen wurden, nach unserem Wissen, erstmals durchgeführt. Die Experimente ermöglichen neuartige Einblicke in die zeitliche Entwicklung des Spinsystems während der ultraschnellen Demagnetisierung. Dabei konnten wir keine Reduzierung der Austauschspaltung, wie es vom Stoner-Modell vorhergesagt wird, beobachten. Stattdessen zeigen die Ergebnisse Anzeichen für eine Durchmischung der Spinzustände.

Abstract

In the last two decades, ultrafast magnetization dynamics has been the subject of a large number of experimental and theoretical investigations, however, without establishing a consistent picture up to now. The objective of the work presented in this thesis is to provide a new and profound perspective on the underlying mechanisms by a direct observation of the spin-dynamics in the electronic band structure of 3*d* ferromagnets using femtosecond time- and spin-resolved photoelectron spectroscopy of the full energy range of the valence bands.

For this purpose, a novel experimental setup has been developed and commissioned that combines a modern, highly efficient spin detector with a state-of-the-art, table-top light source creating ultrashort extreme ultraviolet (XUV) pulses by laser-based high-order harmonic generation (HHG). The light source can be used in two operation modes, which provide XUV radiation with different wavelengths and photon fluxes. Static spin-resolved photoemission spectra of Co(001) films have been measured in both operation modes to find the optimum conditions for time-resolved experiments. Moreover, vacuum space-charge (VSC) effects within the dense electron clouds emitted by the femtosecond XUV pulses as well as the Coulomb interaction between electron clouds generated by XUV probe- and near-infrared (NIR) pump-pulses in a pump-probe experiment have been investigated in detail. The findings are used to determine and later minimize the influence of VSC on photoemission results.

The NIR pump-pulses have been employed in time-resolved measurements to trigger ultrafast demagnetization in Co samples. Using the capabilities of the new experiment, we monitored the time evolution of the electron-dynamics by measuring spin-resolved spectra over a broad energy range fully covering the valence bands. To our knowledge, such measurements have been performed for the first time. The experiments lead to novel insights into the evolution of the spin system during an ultrafast demagnetization process, in particular by showing evidence of spin-mixing instead of a quenching of the exchange splitting as suggested by the Stoner-model.

1 Introduction

Nowadays, information technology (IT) is an essential component of our daily life. Since the first realization of computers in the 1940s, their performance is increasing fast, driven by an approximate doubling of the number of transistors per chip every two years ("Moore's law"). This development created the possibility to handle huge quantities of information. Due to the worldwide network of IT devices, the local and global amount of data is growing even more rapidly during the last two decades. In 2010, 1200 exabyte of data was stored worldwide and the amount is doubling every year [Gantz12]. This trend will continue because of the rising importance of, *e.g.*, online video/photo sharing, digital communication and the need for big data analysis in industry.

The increasing amount of data that has to be handled needs not only huge storage capacities, but also new, faster techniques to store and retrieve the information efficiently. To deal with these challenges, the interaction between magnetic storage materials and laser radiation is explored and suggests interesting and promising approaches. One possible way to realize higher storage capacities is to employ laser light to locally heat an otherwise magnetically hard and stable material and thus make it switchable with standard methods for a defined time interval. Using this technique, which is called heat-assisted magnetic recording (HAMR), materials with a very high anisotropy can be used allowing for smaller bit volumes and therefore higher storage densities while maintaining the energy barrier of the superparamagnetic effect. The concept has been already proven in prototype hard drives [Rausch13] and is planned to enter the consumer market in the next years. Concerning the optical writing of data it was demonstrated at the end of the last century, *e.g.* by Beaupaire *et al.* in 1996 [Beaupaire96], that a transient, laser-induced manipulation of the magnetization of a ferromagnetic material can occur on a sub-picosecond time scale. This process is significantly faster than the writing of information induced by magnetic field pulses [Tudos04]. From the point of view of technology, two important milestones have been reached since the first observations. First, full switching purely induced by a femtosecond light pulse¹ without the need

¹However, it takes tens of picoseconds until an equilibrium state is established again [Vahaplar09].

of a magnetic field was demonstrated in the ferrimagnetic alloy GdFeCo in 2007 [Stanciu07]. Second, this process was recently also proven in ferromagnets marking another important step towards a working device [Lambert14].

As suggested by Beaurepaire *et al.*, an ultrafast quenching of the magnetization can be phenomenologically described by assuming three interacting subsystems that account for the spins, the electrons and the lattice [Beaurepaire96]. Nevertheless, the mechanisms behind the spin-dynamics before the spins and electrons start to thermalize with the phonon system (for > 1 ps) is, despite of almost 20 years of intense theoretical as well as experimental research, not yet understood. For 3d ferromagnets, four models found most attraction during the last years.

First, the laser pulse can directly couple to the spins. This effects occurs in the first femtoseconds while the pump-pulse is still present [Bigot09].

Second, the angular momentum can be transferred from the spin, which supplies the dominant contribution to the magnetic moment, to the orbital part by spin-orbit coupling (SOC) [Zhang00]. Since no enhancement of the latter is observed [Stamm10], an ultrafast dissipation channel of the the orbital magnetic moment has to be considered in this case [Töws15].

Third, spin-flip processes can lead to a direct, ultrafast absorption of the spin angular momentum by the lattice. The most prominent suggestion for such a mechanism is Elliott-Yafet type scattering [Koopmans10]. An example is the scattering of an electron at a phonon when the initial and the final electronic state have a mixed spin character due to SOC (see step 1 in Sec. 2.2.1). Then, a scattering event can have a finite probability to occur even if the initial state is dominated by majority spins and the final state has mainly a minority spin contribution (or *vice versa*). This implies a change of the electron spin. Because the influence of the SOC on the band structure, especially concerning hybridization, depends strongly on the particular wave vector, also the strength of the spin-flip scattering is varying significantly for different positions in the Brillouin zone (BZ) [Pickel08].

Fourth, the spins can leave the sample volume that is probed. This approach is most successfully treated in a theory developed by Battiato *et al.*, which suggests pure spin-currents carried by hot electrons that propagate in an intermediate regime between diffusive and ballistic transport (super-diffusive) [Battiato10]. Corresponding charge currents are screened. The basic idea of this model is that mainly majority spin electrons can leave the optically excited sample volume since they have a longer mean free path in 3d ferromagnets [Aeschlimann97]. Clear evidence for such a spin transport was found in experiments, where excitation and probing are spatially separated [Malinowski08, Melnikov11, Rudolf12, Eschenlohr13].

Up to now, no general agreement about the applicability and importance of the particular models has been established. Currently, different theories can be used to explain different experimental results and their validity seems to depend strongly on the measurement conditions. The experiments, on their part, cover a wide parameter space making a comprehensive modeling difficult. This includes dif-

ferent pump fluences [Rudolf12], geometries like single- [Koopmans10, Stamm10] or multilayers [Turgut13, Eschenlohr13], pure materials [Pickel08, Hohlfeld97] or alloys [Radu09, Mathias12], and various contrast mechanisms including the magneto-optical Kerr effect (MOKE) [Beaurepaire96, Bigot09, Rudolf12], (magnetic) second harmonic generation (SHG) [Hohlfeld97], x-ray magnetic circular dichroism (XMCD) [Stamm07] or (spin-resolved) photoemission [Scholl97, Rhie03]. Nevertheless, most experiments have in common that the studies are dominated by optically triggered approaches because only light pulses can deliver the needed temporal resolution using a pump-probe technique. For a long time the investigations have been limited by the photon energies in the optical to near-infrared (NIR) spectral range of the available femtosecond light sources. Therefore, only the valence bands could be probed in the case of magneto-optical experiments and in photoemission measurements the photon energies just exceeded the work functions of the samples and only very small parts of the BZ and narrow energy windows were accessible. Within the last years, novel schemes for the generation of ultrashort light pulses with photon energies of several tens to hundreds of eV have been developed, namely high-order harmonic generation (HHG), free-electron lasers (FELs), and synchrotron femtoslicing (see Sec. 2.3). All of them were already used in order to create new, substantial insights into ultrafast magnetization dynamics by, *e.g.*, expanding known techniques like MOKE by introducing element-selectivity [Rudolf12] or supplying well-established methods like XMCD or x-ray diffraction with femtosecond temporal resolution [Stamm07, Pfau12]. Also, these new sources had already a huge impact on time-resolved photoelectron spectroscopy (PES) investigations [Hellmann12, Rohwer11, Gierz13].

Concerning magnetism, the photoemission studies performed up to now can be split into two types: first, experiments that study the energy distribution of photoelectrons and, second, experiments that study the spin of photoelectrons. In the last years, both branches profited from the new light sources mentioned above. While the feasibility of using a Mott detector (see Sec. 2.2.3) to analyze the demagnetization of secondary electrons emitted by FEL radiation was demonstrated only recently [Fognini14], angle-resolved photoelectron spectroscopy (ARPES) measurements using HHG light already lead to a better understanding of ultrafast magnetism in 4f materials [Carley12, Teichmann15]. The latter revealed a quenching of the valence band exchange splitting on an ultrashort time scale, when the sample is excited with an intense NIR laser pulse.

Such a mechanism is also discussed as a possible origin of the temperature-dependence of the magnetization in 3d ferromagnets, both if the sample is heated in equilibrium [Hopster83, Kisker84] and on ultrafast time scales [Rhie03, Mueller13]. In general, this understanding based on the Stoner model (see Sec. 2.1.1) is in competition with theories that suggest the conservation of the magnetic order and therefore the original band structure within microscopic regions, but reduce the magnetization due to temporal and spatial fluctuations of its orientation. In Ni,

which was up to now investigated in most detail, previous studies showed evidence that the reduction of the magnetization is accompanied by at least a partial quenching of the exchange splitting for both equilibrium and dynamical heating [Hopster83, Donath89, Rhie03]. In contrast, other experiments indicate that the reduction of the magnetization in Ni is not related to changes in the band structure [Kirschner88]. In addition, the dominant effect seems to depend on the location in the BZ that is probed [Kämpfer90]. In Co neither (Stoner-like) paramagnetic behavior nor peak shifts have been observed above T_C so far, which suggests an explanation purely based on magnetic short-range order effects [Schneider91b]. Here, static heating experiments are, however, difficult because Co changes its properties over the relevant temperature range including phase-transitions [Schneider91b] and diffusion of substrate materials [Allmers11].

The challenges in the static heating experiments can be prevented by investigating optically induced non-equilibrium states, where only the electron system is transiently heated. In general, disentangling the magnetic properties in the band structure of Fe, Co and Ni in a photoemission experiment is more difficult than in the measurements on $4f$ materials introduced above because of the strong correlation between the more delocalized electrons in the $3d$ ferromagnets (see Sec. 4.2). A significant improvement of the disentanglement can be achieved by spin-selective measurements of the photoelectrons. Consequently, we propose a combined spin- and energy-resolved photoemission experiment with femtosecond temporal resolution and photon energies largely exceeding the material work functions in order to obtain decisive results on the high temperature behavior of $3d$ ferromagnets.

Furthermore, Weber *et al.* found deviating demagnetization times on similar samples for measurements using MOKE and using spin-resolved, energy-integrated photoemission. The authors suggest a difference in the part of the BZ which is probed as a possible explanation [Weber11]. Our experiment is well-suited to address the question of deviating decay times of the spin polarization after optical excitation throughout the band structure. In particular, this also includes the role of spin-flips and the influence of SOC hybridization points on the spin-flip probability [Pickel08].

Besides the study of $3d$ ferromagnets, the experiment that we propose above may also be able to reveal further aspects of the dynamics in $4f$ materials, where recently discrepancies in the temporal evolution of different states were observed [Frietsch15]. This includes disjunct time scales for the quenching of the spin polarization and the exchange splitting of the surface state in Gd as well as differences in the behavior of equilibrium and laser-induced heating [Andres15]. Expanding these studies employing our experiment can help to develop a better understanding of the femtosecond dynamics of the band structure. In particular, addressing the time evolution of both the $4f$ and $5d$ states while simultaneously monitoring the spin polarization might deliver a deeper insight into the coupling mechanisms and underlying interactions. Furthermore, the experiment can provide new, direct insights

into the spin-dependence of transport properties of materials like MoS₂, which need high photon energies to be studied due to the shape of their band structure [Grubisic Cabo15] and show interesting magnetic properties [Gehlmann15]. The main challenge in the realization of the proposed experiment is to achieve electron count rates high enough for a reliable interpretation of the data, while still ensuring an energy resolution which is sufficient for the study of the magnetic properties in the band structure. In the presented work, this is addressed by constructing an experiment that combines the, for photoemission, superior properties of a modern HHG source (see Sec. 2.3) with a state-of-the-art spin detector employing highly efficient exchange scattering (see Sec. 2.2.3). Recent developments, like driving the HHG source with laser light of 390 nm wavelength, were incorporated to increase the performance of the experiment (see Sec. 3.1) leading, finally, to a successful demonstration of its feasibility. Proof of principle results have been acquired which provide new insights into the band structure dynamics of Co.

This thesis is structured in the following way:

Chapter 2 provides the theoretical basis for the following chapters. It gives an overview of the magnetism in 3d ferromagnets including the exchange interaction and the SOC. In the 2nd part, the basic concepts of photoemission, which are necessary for the understanding of this work, and different detection schemes for the photoelectron spin are presented. Finally, the properties of the HHG light and the processes that are fundamental for its generation are described.

Chapter 3 explains the different parts of the experimental setup. A special focus is put on the realization of the HHG source in two driving modes and the devices used for the energy selection and the spin detection.

Chapter 4 introduces the sample system that is studied: thin Co films grown on Cu(001). A brief review of the current state of knowledge is provided and the preparation procedure is presented. Furthermore, the samples are characterized using static photoemission measurements.

Chapter 5 shows static, spin-resolved measurements recorded using femtosecond pulses from the HHG source. The results are discussed with special emphasis on the feasibility of time- and spin-resolved experiments in both driving modes. Furthermore, the data is compared to measurements obtained with a continuous wave (cw) light source in order to characterize the light from the HHG source as well as possible differences in the spectra due to the pulsed excitation. This characterization then results in an analysis of vacuum space-charge (VSC) effects for our experimental conditions.

Chapter 6 describes the preparation of our setup for time-resolved measurements by introducing a pump-beam. First, techniques for finding the temporal and spatial overlap are presented. Second, photoemission induced by the NIR pump-pulses is studied by varying several laser parameters, and its influence on pump-probe measurements through additional VSC is recorded and analyzed with the help of simulations. Third, the stability of the setup for time-resolved studies with long acquisition times is estimated based on experimental results.

Chapter 7 presents results for the electron- and spin-dynamics in Co. Based on time-resolved ARPES data, the electron-dynamics in the face-centered tetragonal (fct) Co(001) samples is investigated. Furthermore, information about the spin-dynamics during an ultrafast demagnetization process is obtained by simultaneous time-, energy- and spin-resolved photoemission measurements in normal emission. The results are complemented by similar studies on hcp Co. The picture that we obtain from these experiments suggests a dominant role of a mirroring of the band structure rather than a quenching of the exchange splitting during the ultrafast demagnetization.

Chapter 8 gives a short summary of the presented work and suggests future studies as well as further experimental fields that can be explored with the setup.

2 Fundamental Considerations

This chapter will provide a short overview of some of the main concepts and basic considerations, which are necessary to understand the ideas and studies presented in this thesis. In particular, involved magnetic effects (Sec. 2.1), the photoemission process, its relevance for experimental studies and detection mechanisms for the photoelectron spin (Sec. 2.2), and the working principle of high-order harmonic generation (HHG) that is used in the light source (Sec. 2.3) are covered. The explanations are in general adapted from the mentioned sources and represent textbook knowledge.

2.1 Magnetism in 3d Transition Metals

The following section will give a brief introduction into some fundamental properties of ferromagnetism with special attention to the effects that induce changes in the electronic band structure. A more detailed description of magnetism in general and more details about the effects described here can be found, for example, in [Stöhr07].

The magnetic properties of the 3d transition metals Co, Ni and Fe are dominated by their ferromagnetic characteristic. In contrast to other magnetic mechanisms such as dia- or paramagnetism, ferromagnetism is characterized by a "spontaneous" magnetic order that not necessarily needs a magnetic field to be present and leads to the formation of magnetic domains. Starting from phenomenological observations of ferromagnetism, the most obvious detection is that two bars built of a ferromagnetic material can either attract or repel each other depending on their relative orientation. This behavior leads to the introduction of a (macroscopic) quantity called "magnetization" \vec{M} as a three-dimensional vector, which represents the collective behavior of the magnetic domains. For a bar magnet it usually points along or opposite to the long dimension of the bar and the direction can be induced by aligning the domains with an external magnetic field. If the external magnetic field is removed, \vec{M} is still (partly) present and creates an own magnetic field. The latter can then act on the magnetization of the second bar magnet and lead to an interaction. In order to relate this macroscopic magnetization to microscopic

properties, \vec{M} can be defined as the density of N (aligned) magnetic dipole moments \vec{m} in the volume V by

$$\vec{M} = \frac{N}{V} \vec{m}. \quad (2.1)$$

Since ferromagnetism is a phenomenon that is dominated by the collective behavior of the electrons in a material¹, the magnetic properties of the single electrons can be in good approximation assigned to the magnetic dipole moments in Eq. 2.1. In general, the electron magnetic momentum $\vec{m}_{electron}$ consists of two parts. The first is called "orbital magnetic moment" \vec{m}_{orb} , because it is based on the movement of the electron in the solid and can thus be related to the orbital angular momentum² \vec{l} . This relation can be expressed by

$$\vec{m}_{orb} = -\frac{e\mu_0}{2m_e} \vec{l} \quad (2.2)$$

with the elementary charge e , the electron mass m_e and the vacuum permeability μ_0 .

Furthermore, for example the Stern-Gerlach experiment showed that electrons have an additional intrinsic property that is called "spin" \vec{s} and creates another angular momentum. The resulting "spin magnetic moment" \vec{m}_{spin} can be given in an analogue form by

$$\vec{m}_{spin} = -\frac{e\mu_0}{m_e} \vec{s}. \quad (2.3)$$

However, \vec{s} can only take the value $+\hbar/2$ or $-\hbar/2$. Altogether, the electron magnetic moment is then given by

$$\vec{m}_{electron} = \vec{m}_{orb} + \vec{m}_{spin} = -\frac{e\mu_0}{2m_e} (2\vec{s} + \vec{l}). \quad (2.4)$$

2.1.1 Exchange Interaction

In order to generate a net magnetization $M \neq 0$, the orientation of the electron magnetic moments can not be randomly distributed and they have to be at least partly aligned. The fundamental mechanism behind this alignment in ferromagnets is called "exchange interaction" and is based on the quantum mechanical exchange between two indistinguishable electrons. In a simple picture, its working principle can be exemplarily explained using the covalent binding situation between two

¹Nuclei have much higher masses than electrons. Because the dependence of their magnetic moment \vec{m}_n on their mass is similar to the expression for the electrons in Eq. 2.4, \vec{m}_n is significantly smaller than $\vec{m}_{electron}$ and can be neglected.

²If a quantum mechanical picture is used, spins, orbital momenta and magnetic dipole moments are in the following given as vectors implicating that the quantum mechanical expectation value $\langle a \rangle_z$ of the quantity a along a quantization axis z is meant and that they might act as the corresponding operators.

hydrogen atoms³. By approximating the total wave function as a product of the single-atom wave functions ϕ_i of the atom i and neglecting terms with two electrons in the vicinity of one of the atom cores due to Coulomb repulsion ("Heitler-London approximation"), one achieves for the spatial wave function

$$\Phi(1, 2) = \phi_A(1)\phi_B(2) \pm \phi_A(2)\phi_B(1). \quad (2.5)$$

Here, (1)/(2) denotes that the first/second electron is in the vicinity of the particular atom core. The second term in Eq. 2.5 accounts for the (anti-)symmetrization that is necessary because of the indistinguishability of the electrons. Due to the spin-statistics theorem, the total wave function of a two-fermion system has to change its sign if the fermions exchange position. Since the total wave function can be expressed by a product of the spatial and the spin part, this antisymmetry is either achieved by an antiparallel spin configuration and a symmetric spatial wave function (+sign in Eq. 2.5) or a parallel spin configuration and an antisymmetric spatial wave function (-sign in Eq. 2.5). Calculating the energy expectation value for both resulting states shows that the values differ. The difference defines the "exchange constant" J . For $J > 0$, a parallel coupling between the two electrons is energetically favorable. These considerations show that the exchange interaction is dominated by the electron spin.

In order to use the picture developed above for the explanation of the ferromagnetism in 3d metals, it has to be generalized for the interaction of many electrons in a band model. For a visualization of the underlying processes, it is useful to regard only one electron and calculate the effect of all other electrons on it. This leads to an energy change induced by the exchange interaction for this electron (labeled with i) of

$$E_{ex,i} = -\vec{s}_i \sum_{j:j \neq i}^N J_{ij} \vec{s}_j = -\vec{s}_i \vec{H}_{eff} \quad (2.6)$$

with J_{ij} being the exchange constant of the interaction between electron i and j . The vectors \vec{s}_i and \vec{s}_j describe the corresponding spins. On the right side of the second equal sign, the single interactions with all other electrons are summarized in an effective field \vec{H}_{eff} . In general, the energy of electron i is reduced if \vec{H}_{eff} has a positive value and is aligned parallel to \vec{s}_i , meaning that the spin of most of the other electrons is pointing in this direction. The size of \vec{H}_{eff} depends on the ratio of electrons with parallel and antiparallel aligned spin with respect to electron i . Once an imbalance is present, it is in consequence energetically favorable/unfavorable for an electron to align along the spin direction that the majority (\uparrow)/minority (\downarrow) of electrons has (see left graph in Fig. 2.1). The resulting energy gain or loss is given by

$$E_{ex,\uparrow/\downarrow} = \mp I \frac{\Delta n}{2}. \quad (2.7)$$

³The following argumentation is along the explanations in [Ibach02, Opel04].

Here,

$$\Delta n = \frac{n_{\uparrow} - n_{\downarrow}}{n_{\uparrow} + n_{\downarrow}} \quad (2.8)$$

is the normalized difference in the number of majority/minority spin electrons $n_{\uparrow}/n_{\downarrow}$ and the proportionality constant I is called "Stoner parameter". Δn is directly related to the magnetization M .

On the other hand, the imbalance of majority and minority spins leads to a loss in energy because electrons can only change their spin if they move to unoccupied states that had originally a higher energy in the band structure (see middle graph in Fig. 2.1). The reoccupation can be taken into account by describing $n_{\uparrow}/n_{\downarrow}$ using

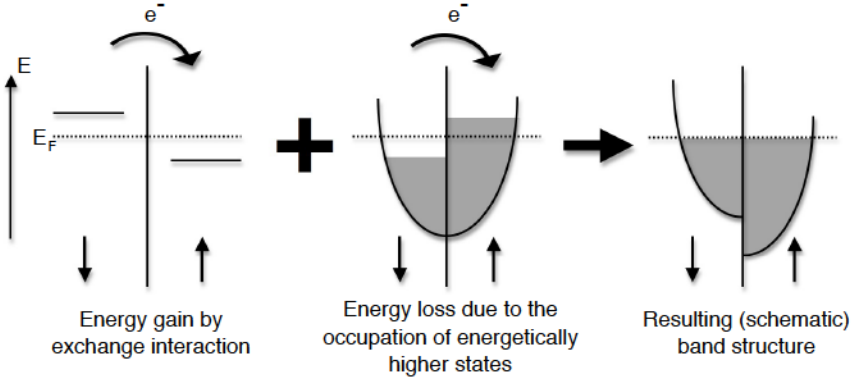


Figure 2.1: Energy contributions leading to ferromagnetic equilibrium. The left graph shows the lowering of the energy of an electron resulting from a spin alignment parallel to the majority (\uparrow) of the electrons due to the exchange interaction. In contrast, the spin flips lift the electrons to originally higher energy levels in the density of states (center). Both contributions can result in an equilibrium situation where the part of the band structures for majority and minority (\downarrow) spin electrons is shifted towards each other in energy. In the graphs, parabolas represent the density of states for free electrons at $T = 0$ K with shaded areas showing filled and white areas illustrating unfilled parts. (adapted from [Plötzing11])

Fermi-Dirac distributions $f(E_{ex,\uparrow/\downarrow})$ that take into account the energy shifts. This results in the self-consistency relation

$$\Delta n \propto \sum_k (f_{\uparrow,k}(\Delta n) - f_{\downarrow,k}(\Delta n)), \quad (2.9)$$

where the sum ensures the consideration of the full space of wave vectors k . It describes the competition between the energy gain due to the exchange interaction and the energy loss due to the occupation of energetically higher states for a parallel spin alignment. From Eq. 2.9 the "Stoner criterion"

$$I\tilde{D}(E_F) > 1 \quad (2.10)$$

can be derived⁴. It contains the density of states per atom and spin direction $\tilde{D}(E)$ at the Fermi level E_F . If the Stoner criterion is fulfilled, a material is predicted to be ferromagnetic. Despite its simplicity, the model is very successful in forecasting ferromagnetism for Fe, Ni and Co. These materials have a very high density of states close to the Fermi level and thus only a low amount of energy is lost for the "spin-flips" making a parallel alignment favorable.

Moreover, Eq. 2.9 can be used to give an explanation of the temperature-dependence of the ferromagnetic behavior. Since the Fermi-Dirac distributions, which describe the occupation of the energy levels, include the temperature T , the self-consistency relation can be evaluated for different T . For a qualitative understanding, it is a good approximation to model the band structure by Dirac delta functions representing the dominating 3d states (see left graph in Fig. 2.1). The results show a reduction of the (spontaneous) magnetization with increasing temperature. Above the so-called "Curie temperature" T_C , the ferromagnetic behavior vanishes⁵. The

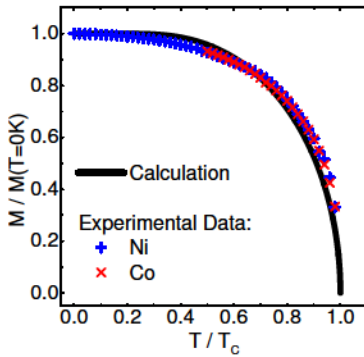


Figure 2.2: Temperature dependence of the magnetization. The line represents a calculation of the normalized magnetization for different temperatures T based on Eq. 2.9. Symbols are experimentally determined values for Ni and Co from [Crangle71].

full dependency is presented in Fig. 2.2 together with experimental data. It can be seen that the results mostly agree over a large temperature range.

Altogether, the exchange interaction causes a momentum-independent and in the Stoner-model temperature-dependent offset in energy between the valence band structure of majority and minority spin electrons in 3d ferromagnets (see right graph in Fig. 2.1).

⁴A more formal treatment including further information is given in [Ibach02].

⁵However, the prediction of T_C is very imprecise in this model.

2.1.2 Spin-Orbit Coupling

Another effect that can have a significant influence on the electronic band structure, however, not only in ferromagnets, is the "spin-orbit interaction" that describes the coupling between the electron spin and its orbital momentum in the Coulomb field of a nucleus. In a semi-classical picture of this interaction, the orbital momentum is interpreted as a relative movement between both particles. In the reference frame of the electron, the nucleus circles around it and produces a current that, according to Faraday's law of induction, creates a magnetic field [Gay92]

$$\vec{B} = \frac{Ze}{cr^3} \vec{r} \times \vec{v} = \frac{Ze}{m_e cr^3} \vec{l}. \quad (2.11)$$

Here, Z is the atomic number of the nucleus, \vec{r} the distance between the particles with the length r , \vec{v} the relative velocity between both, and \vec{l} the resulting orbital momentum. c , m_e and e represent the speed of light, the electron mass and the elementary charge, respectively. The magnetic field \vec{B} then acts on the spin moment of the electron \vec{m}_{spin} (see Eq. 2.3). Since the change of the potential energy is given by

$$V = -\vec{m}_{spin} \cdot \vec{B}, \quad (2.12)$$

this causes an increase or decrease of the electron energy depending on its spin direction.

A quantum mechanical approach leads to a description of the energy change induced by the spin-orbit coupling (SOC) described by the Hamiltonian $\mathcal{H}_{so} = k \cdot \vec{s} \cdot \vec{l}$ with \vec{s} being the spin and \vec{l} the orbital angular momentum. As in the semi-classical picture, the constant k depends on the atomic number and the radius of the electron orbit. In addition, the dependence of the energy on \vec{l} and \vec{s} is similar.

In the valence bands of 3d ferromagnets, the energy split due to the SOC has a value of around $\Delta E_{so} = 0.01 - 0.1$ eV and is thus small compared to the exchange-induced splitting ($\Delta E_{ex} \approx 1$ eV) [Stöhr07]. Nevertheless, the SOC is crucial for the properties of ferromagnets since it induces a symmetry breaking. This leads to, *e.g.*, magnetic anisotropies and influences the electronic band structure (see step 1 in Sec. 2.2.1).

2.2 Photoelectron Spectroscopy

In the presented work, the electronic band structure of ferromagnets is investigated, which contains valuable information about the exchange interaction and the SOC as described in the last section. For this purpose, the photoemission process is used. The basis of photoemission is the photoelectric effect that describes the release of an electron from a material after excitation with light. Today, photoelectron

spectroscopy (PES) is one of the most applied experimental techniques for studies of the behavior of electrons particularly in solid state materials. Its importance is underlined by two Nobel Prizes for Albert Einstein in 1922 and Kai Siegbahn in 1981, who were awarded for the explanation of the photoelectric effect by quantizing the light energy and for improvements of the resolution of PES, respectively.

Nowadays, photoemission allows one to look into many fundamental characteristics of a material, *e.g.* the optical or magnetic behavior, by measuring the properties of the photoemitted electron and relating them to the original state inside the material using conservation laws. The most fundamental observable in PES is the kinetic energy E_{kin} of the photoelectron that, if monochromatic light with the energy $h\nu$ is used, can be related to the binding energy E_B of the electron in the solid using energy conservation by

$$E_{kin} = h\nu - \phi - E_B. \quad (2.13)$$

Here, the material-specific "work function" ϕ is the minimum energy that is necessary in order to release electrons into the vacuum. Furthermore, the in-plane components of the original electron momentum can also be determined by measurements of the escape angle of the photoelectron due to momentum conservation (see Eq. 2.22). Another quantity that is often conserved during the photoemission process is the spin of the electrons (see Sec. 2.2.3, especially for detection schemes).

2.2.1 Three-Step Model of Photoemission

A simple (semi-classical) theory that is very successful in order to provide a qualitative understanding of the fundamental processes involved in photoemission is the "three-step" model⁶. Here, the full process is divided into three independently considered parts: (1) the excitation of the electron by the incoming light, (2) its travel through the crystal to the surface and (3) the emission from the surface into vacuum. In this model, the photoemission process is treated in a single electron approach ("independent particle picture") and the rearrangement of the electron system due to the leaving electron is neglected. Each of the steps will be discussed in more detail in the following paragraphs.

Step 1: Optical Excitation & Selection Rules

In the optical excitation step, an electron is lifted from an occupied initial state $|i\rangle$ with energy E_i into an unoccupied final state $|f\rangle$ with energy E_f due to the absorption of a photon. The energy difference between both states has to match the photon energy ($E_f - E_i = h\nu$). For the photon energies employed in the presented work, which are located in the extreme ultraviolet (XUV) spectral range, the photon wave

⁶The following explanations are based on [Hüfner95] and [Schneider10], where more details can be found. Another nice overview is given in [Smith71].

vector $k_{ph} = h\nu/(\hbar c)$ reaches values that are two orders of magnitude smaller than typical dimensions of the Brillouin zone (BZ) of metals⁷. Therefore, a momentum transfer from the photon can be neglected in the optical excitation process and only "direct" transitions are allowed, which are vertical in the reduced zone scheme.

In order to describe the transition of the electron in a quantum mechanical way, the electromagnetic field of the light represented by its vector field $\vec{A} = \vec{A}(\vec{r})$ has to be included in the Hamiltonian \mathcal{H} by extending the momentum operator from \vec{p} to $\vec{p} - e/c\vec{A}$ yielding

$$\mathcal{H} = \frac{1}{2m} \left(\vec{p} - \frac{e}{c}\vec{A} \right)^2 + eV + \mathcal{H}_{int}. \quad (2.14)$$

Here, the electrostatic potential $V = V(\vec{r})$ takes in particular into account the field of the crystal lattice. Moreover, \mathcal{H}_{int} can include several effects like relativistic corrections or the interaction of the spins with external fields, the lattice (through SOC) or themselves [Schneider10]. The additional terms

$$\Delta\mathcal{H} = \frac{1}{2m} \frac{e}{c} \left(-\vec{p}\vec{A} - \vec{A}\vec{p} + \frac{e}{c}\vec{A}^2 \right) \quad (2.15)$$

resulting from the extension of the momentum operator can be treated as a perturbation and the probability $P_{i \rightarrow f}$ for a transition from the state $|i\rangle$ to the state $|f\rangle$ is then given by Fermi's golden rule:

$$P_{i \rightarrow f} = \frac{2\pi}{\hbar} |\langle f | \Delta\mathcal{H} | i \rangle|^2 \delta(E_f - E_i - h\nu). \quad (2.16)$$

Here, $|i\rangle$ and $|f\rangle$ are represented by the corresponding eigenfunctions of the undisturbed Hamiltonian and the Dirac delta function $\delta(E_f - E_i - h\nu)$ ensures energy conservation. For moderate photon flux⁸ nonlinear contributions in \vec{A} can be neglected in the transition matrix element (linear response theory) $M_{fi} = \langle f | \Delta\mathcal{H} | i \rangle$. Furthermore, the electromagnetic field contribution can be approximated by the first, space-independent term of its Taylor series since the wavelength of XUV radiation is long compared to the lattice constant of metals. This leads, as described in [Schattke08], to the expression (dipole approximation)

$$M_{fi} = \frac{-ie}{\hbar c} A_0 (E_f - E_i) \langle f | \vec{e}\vec{r} | i \rangle \quad (2.17)$$

⁷The photon momentum is $k_{ph} \approx 5 \cdot 10^{-2} \text{ \AA}^{-1}$ for $h\nu = 100 \text{ eV}$. The BZ has a width of $k_{el,max} = 2\pi/a = 1.74 \text{ \AA}^{-1}$ for an in-plane lattice constant of $a_{\parallel} = 3.61 \text{ \AA}$ in Co(001) [Heckmann94].

⁸This is fulfilled for an excitation with the XUV probe-pulses from the HHG source (see Sec. 2.3 and Sec. 3.1). From the light properties presented in [Eich14] and with a spot diameter of $d = 100 \mu\text{m}$ a peak intensity (see Eq. 6.1) of the order of 10^7 W/cm^2 can be estimated. This value is within the validity of (first-order) perturbation theory (breakdown between 10^{10} W/cm^2 and 10^{13} W/cm^2 [Burnett93]) and the related neglect of higher orders in \vec{A} [Schattke08]. Moreover, the applicability of the assumption is confirmed by the agreement of the results between the pulsed and the continuous excitation presented in Chap. 5. In contrast, the assumption is not fully satisfied for the intense near-infrared pump-pulses used in the presented work (see Sec. 6.2).

for the transition matrix element. Here, the complex scalar A_0 is the amplitude of the electromagnetic field, \vec{r} is the position of the particle, and the unit vector \vec{e} represents the direction of the light polarization.

In order to get a basic understanding about which transitions contribute to the photoexcitation process, it is useful to first evaluate these findings within a single-atom picture. Using spherical coordinates, the angular part of the wave functions in Eq. 2.16 as well as the matrix element in Eq. 2.17 can then be expressed using spherical harmonics Y_{lm} . For the case of linearly polarized light, which is particularly important for the presented work (see properties of the used light sources in Sec. 3.1), the dipole operator has the form $\vec{e}\vec{r} \propto rY_{10}$. This leads to an angular part of the integral over the transition matrix element described by

$$\langle f | \vec{e}\vec{r} | i \rangle \propto \int Y_{l_f m_f}^* Y_{10} Y_{l_i m_i} d\Omega \quad (2.18)$$

with Ω being the solid angle and $Y_{l_f m_f}^*$ being the complex conjugate of $Y_{l_f m_f}$. The product of two spherical harmonics can be expressed⁹ as $Y_{l_1 m_1} Y_{l_2 m_2} \propto \Sigma_l \Sigma_m Y_{lm}$ with $l = l_1 + l_2$ and $m = m_1 + m_2$. Using in addition the orthogonality of the spherical harmonics $\int Y_{l' m'}^* Y_{l'' m''} d\Omega = \delta_{l' l''} \delta_{m' m''}$ with the Kronecker delta δ_{ij} , it can be shown that the transition matrix elements vanish unless

$$\Delta l = l_f - l_i = \pm 1 \quad (2.19)$$

and

$$\Delta m = m_f - m_i = 0. \quad (2.20)$$

These conditions are called "dipole transition rules".

Similar rules can be obtained for the transitions between bands in a solid depending on their symmetries in a group theory consideration. They are very useful in order to identify which transitions contribute to the photoemission spectra in certain experimental situations and thus help to understand the electronic band structure. In general, the symmetry properties of bands are described by the so-called "irreducible representations" of a symmetry group. For a treatment based on the spatial symmetries of a system, the corresponding group is determined by the crystalline structure of the material and the investigated direction. In this case, the representations are usually labeled according to the "single group notation". An example for fcc crystals, which are mainly studied in this work, is Δ_i , where the Δ indicates the $\Gamma - X \hat{=}$ [001] direction in the BZ (see left side of Fig. 2.3). The index i is used to distinguish between the different types of bands and labels the symmetry properties along this direction (see Appendix), which are also represented by the basis functions of the representation given in the right part of Tab. 2.1.

As for the derivation of the dipole transition rules in the atomic case, a photoexcitation is only possible for non-vanishing transition matrix elements M_{fi} in Eq. 2.17.

⁹See [Sakurai94] for a proof.

Table 2.1: Non-relativistic dipole selection rules. The results are determined for normal emission in an fcc crystal along the $\Delta \hat{\equiv} \Gamma - X$ direction. \perp (\parallel) indicates that a transition is possible with light having an electric field polarization perpendicular (parallel) to the sample surface. In the right part of the table, the basis functions of the initial states are shown with z pointing along the Δ -direction (selection rules taken from [Eberhardt80], basis functions taken from [Dresselhaus08]).

| Initial State | Final State | | | | | Basis Functions |
|---------------|-------------|---------------|-------------|---------------|-------------|--|
| | Δ_1 | $\Delta_{1'}$ | Δ_2 | $\Delta_{2'}$ | Δ_5 | |
| Δ_1 | \perp | | | | \parallel | $1, z, 2z^2 - x^2 - y^2$ $xy(x^2 - y^2)$ $x^2 - y^2$ xy x, y, xz, yz |
| $\Delta_{1'}$ | | \perp | | | \parallel | |
| Δ_2 | | | \perp | | \parallel | |
| $\Delta_{2'}$ | | | | \perp | \parallel | |
| Δ_5 | \parallel | \parallel | \parallel | \parallel | \perp | |

However, if the integrand, which consists of the dipole operator and the initial and final state, has in total odd symmetry¹⁰, M_{fi} is always zero. Moreover, the dipole operator for linearly polarized light has even symmetry for the polarization component perpendicular to the surface and odd symmetry for the parallel part. This immediately has the consequence that, in normal emission, transitions between states with the same symmetry are only possible using light with a polarization component perpendicular to the surface. Accordingly, a transition between a symmetric and an antisymmetric state can in general only be induced by an antisymmetric dipole operator, *i.e.* using light with a component that is polarized parallel to the sample surface. Furthermore, for several pairs of initial and final states the exact symmetry properties do not allow any transitions within the dipole framework. The results of these considerations for an fcc crystal along the Δ -direction are summarized in the (non-relativistic) selection rules presented in the left part of Tab. 2.1.

So far, magnetic effects were not taken into account in the consideration of the photoexcitation. Because the electron spin is not directly affected by the dipole operator, the exchange interaction (see Sec. 2.1.1) can be included in good approximation by a separate treatment of the processes in two disentangled band structures for the majority and the minority spin electrons. They are shifted with respect to each other in energy ($\Delta_{ex} \approx 1.55$ eV in the valence bands of Co(001) [Clemens92]). In 3d ferromagnets, the shifts induced into the valence bands by the spin-orbit interaction (see Sec. 2.1.2) are significantly smaller than the exchange splitting (≈ 100 meV in Co(001) [Pickel08]). Since they are below the energy resolution of the experiments performed in the presented work ($\Delta E > 200$ meV, see Sec. 5.2), they can not be directly seen in the results. However, the SOC induces an additional symmetry breaking in the system that is non-negligible for the band structure. It

¹⁰A function $f(x)$ has even symmetry if $f(x) = f(-x)$ and odd symmetry if $-f(x) = f(-x)$.

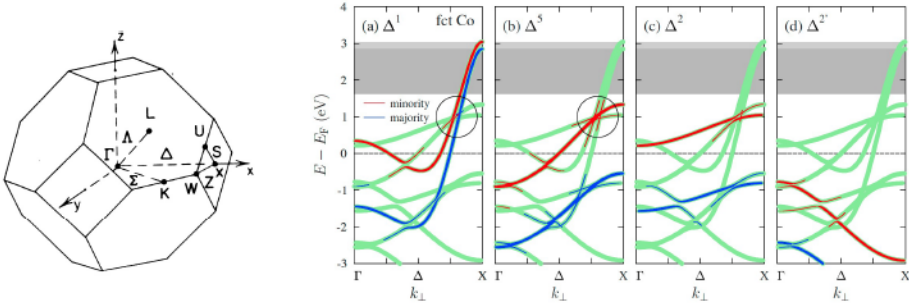


Figure 2.3: Left: Brillouin zone of an fcc crystal. The high-symmetry points and corresponding directions are indicated. (Reprinted with permission from [Eberhardt80]. Copyright by the American Physical Society. The CC license does not apply.) Right: Band structure of Co(001) along the Δ -direction. The green lines show the result of a relativistic band structure calculation including band hybridization induced by SOC. In the four graphs, the red/blue coloring represents contributions to the band structure of a majority/minority state that has, in a non-relativistic treatment, the symmetry properties indicated at the top. The weight of each contribution is illustrated by the thickness of the lines. (Reprinted with permission from [Chiang10]. Copyright by the American Physical Society. The CC license does not apply.)

leads to a hybridization of bands, which are otherwise not interacting¹¹. In particular, this removes the decoupling of the majority and minority spin band structure. As a result, the electronic bands can have mixed symmetry and spin character and also the shape changes close to hybridization points. On the right side of Fig. 2.3, the green lines in all graphs show a band structure that is calculated by Chiang *et al.* including SOC¹². In addition, the authors projected the spin and symmetry character of the hybridized bands to the contributions from the different spatial symmetries (blue/red parts in the separate graphs for majority/minority spin electrons). Having this knowledge about the single group character of the states involved in a band, the non-relativistic selection rules can still supply valuable information about the underlying transitions in a photoemission process.

Step 2: Travelling to the Surface & Information Depth

After the excitation of the photoelectrons into the final state inside the crystal, they have to propagate to the surface in order to be emitted. In PES one is mainly interested in the characteristics that the electrons have before the photoemission process happens. Therefore, the part of the photoelectrons that conserves the original properties is particularly important. However, during the transport to the surface

¹¹More details about the influence of the SOC and the resulting hybridization of states can be found in [Kuch01].

¹²Calculations taking into account the SOC are often called "relativistic".

the electrons interact with other electrons, phonons or defects. Among the scattering mechanisms that change the momentum or the kinetic energy of the excited photoelectron, the inelastic electron-electron interaction is dominant. The amount of electrons that reach the surface without an (inelastic) disturbance $I(d)$ can be described by an exponential damping

$$\frac{I(d)}{I_0} = \exp\left(-\frac{d}{\lambda_{IMPF}}\right), \quad (2.21)$$

where d is the propagation distance inside the crystal and I_0 the total number of created photoelectrons. The information depth in a photoemission experiment is then mainly determined by the inelastic mean free path (IMFP) λ_{IMPF} of the electrons. In Fig. 2.4, the so-called "universal curve" is shown, where λ_{IMPF} is plotted against the kinetic energy of the electrons for different materials.

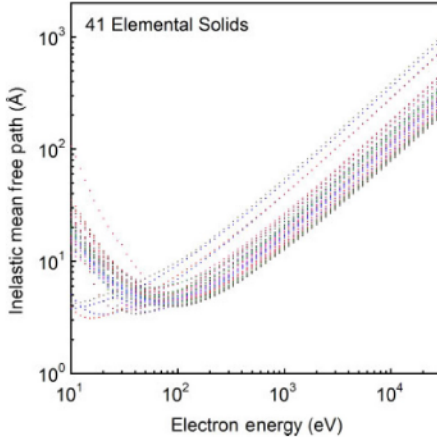
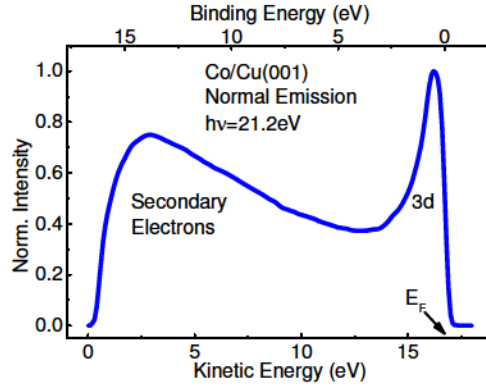


Figure 2.4: Inelastic mean free path of electrons in different materials. The calculated values are shown as a function of their kinetic energy. (Reprinted with permission from [Tanuma11]. The CC license does not apply.)

In general, the scattering probability and thus λ_{IMPF} for a specific kinetic energy of the excited electrons is determined by the amount of states to which the electrons can scatter. Therefore, an individual shape of the curve in Fig. 2.4 is expected for each material depending on its specific band structure. Surprisingly, the curves are only shifted for the different materials and the general shape is always the same: λ_{IMPF} shows a minimum at around 50 – 100 eV and increases for higher and lower electron energies. The universality of the curve is mainly given for kinetic energies above 20 eV because there the distinct band structure of the different materials induced by the crystal potential can be neglected to first order and the behavior of the electrons can be generally modeled by a free-electron gas. For kinetic energies below these values a more material-specific dependence is observed, especially for insulators and semiconductors [Hüfner95]. In Fig. 2.4, this influence can be seen for the alkali metals and diamond which lie below and above the set of curves, respectively.

Besides the inelastic mean free path, the effective attenuation length (EAL) is often used as a measure of the information depth. This parameter is based on the IMFP, but takes additionally into account that the effective path of the electrons to the surface can be elongated by elastic scattering events. Even though these events do not change the energy of the electrons, the longer path makes an inelastic scattering event more probable and thus reduces the information depth [Hofmann12]. It can be seen from Fig. 2.4 that PES experiments are, in particular for kinetic energies of valence band photoelectrons excited with XUV light, very surface sensitive due to the inelastic scattering processes.

Figure 2.5: Typical photoemission spectrum with XUV light. At high kinetic energies the spectrum is dominated by structures from undisturbed or only elastically scattered electrons, whereas for decreasing kinetic energies a rising background from inelastically scattered secondary electrons is contributing.



It has to be noted that all quantities used above to describe the information depth are only statistical parameters. Therefore, a part of the electrons always scatters inelastically. During these processes energy is transferred to electrons which were not excited before and that afterwards also contribute to the photoelectron spectrum. In addition, the electrons that are newly excited can scatter again during their propagation through the crystal. The resulting cascade of electrons with decreasing energy leads to the low energy tail of secondary electrons that is typically present in photoemission spectra (see Fig. 2.5). In contrast, the photoelectrons that originate from the valence bands and reach the surface without being inelastically scattered can be typically found at higher kinetic energies for an excitation with XUV light. The intensity of the secondary electron background is increased by effects that lead to additional scattering like defects in the crystalline structure or surface contaminations. Therefore, the ratio of the intensity of valence band electrons, which were not involved in inelastic scattering processes, and the intensity of the secondary electron tail can serve as an indicator for the sample quality.

Step 3: Emission of the Photoelectron & Determination of the Electron Wave Vector

In order to be detected, the photoelectrons have to leave the crystal when reaching its surface. Therefore, they need to overcome the potential gradient that connects the (periodic) potential inside the crystal to the potential-free vacuum surrounding. This "surface potential barrier" leads to a change of the electron wave vector component perpendicular to the surface k_{\perp} , *i.e.* along the potential gradient¹³. However, the two components of the wave vector parallel to the crystal surface, namely $k_{\parallel,x}$ and $k_{\parallel,y}$, are conserved during the escape process since the translational symmetry is not broken in these directions [Gobeli64, Damascelli04]. Consequently, the equation

$$k_{\parallel} = \frac{1}{\hbar} \sqrt{2m (E_{kin} \sin^2(\Theta))} \quad (2.22)$$

can be derived from geometrical arguments, where m is the electron mass, E_{kin} is the kinetic energy given by Eq. 2.13 and Θ is the escape angle of the photoelectron. Thus, observing E_{kin} and Θ experimentally allows a direct determination of both components of k_{\parallel} .

In contrast, a direct measurement of k_{\perp} is difficult due to the influence of the surface potential. In order to gain knowledge about this component of the electron wave vector, different approaches have been developed (see [Hüfner95]). The most common method to study the band structure in k_{\perp} direction is to use the wave vector-conserving nature of (direct) optical transitions. As a result, excitations can only happen for wave vectors, where the band structure allows a vertical transition while simultaneously fulfilling the energy conservation. Moreover, the conditions for the energy conservation vary for different photon energies resulting in a change of the position in the BZ where the excitation takes place. Therefore, different wave vectors can be probed if $\hbar\nu$ is modified. This approach has a high potential if the unoccupied final states above the Fermi level are already known from band structure calculations and/or measurements using, *e.g.*, inverse photoelectron spectroscopy (IPES) [Dietz79, Strocov96]. Often, a very successful way of predicting transitions is to assume a free-electron parabola for the final state. This "free-electron final-state model" is in particular valid, if the influence of the crystal potential on the final state can be neglected as for an excitation with high photon energies, especially in metals. Then, the perpendicular momentum component is given by (see [Damascelli04])

$$k_{\perp} = \frac{1}{\hbar} \sqrt{2m (E_{kin} \cos^2(\Theta) + V_0)} \quad (2.23)$$

¹³This can be easily shown, if the spatial pattern of the barrier is neglected and it is modelled as a step-like function connecting a constant potential V_0 inside the crystal to the potential-free area in the vacuum. Determining the wave functions of a planar wave propagating perpendicular to the surface plane in a simple one-dimensional Schrödinger equation framework (see, *e.g.*, [Nolting02]) leads to different wave vectors for both areas: $k_{crystal} \propto \sqrt{E - V_0}$ inside the crystal and $k_{vacuum} \propto \sqrt{E}$ in vacuum.

with E_{kin} from Eq. 2.13 and V_0 being the so-called "inner potential". V_0 accounts for the offset between the free-electron parabola inside and outside the crystal and can be determined from experiment (periodicity of the band structure), theory (minimum of the periodic potential) or a combination of both (adjustment of results). In general, the free-electron final-state model is not accurate at the boundaries of the BZ because in this region band gaps are present and lead to a bending of the bands. In addition, the parabolic shape of final states can be significantly distorted, *e.g.*, due to the hybridization of bands.

Besides the requirements for possible transitions due to the dipole selection rules (see left side of Tab. 2.1), the experimental geometry can further limit the available final states. In the presented work, most measurements are performed in normal emission from a fcc (001) surface. Here, only Δ_1 final states are allowed, because other symmetries do not support a propagation of the electron in the detector direction [001] [Day12]. For example, the Δ'_2 state, which has the same symmetry as the $3d_{xy}$ atomic orbital (see right side of Tab. 2.1) shown in Fig. 2.6, has no electron probability density along the [001]-direction.

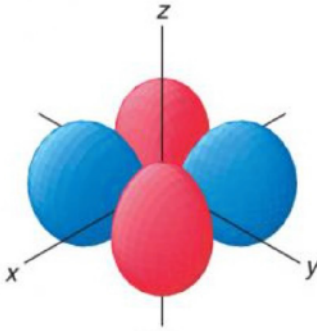


Figure 2.6: Angular distribution of an atomic orbital without component along the $z=[001]$ -direction. The red and blue spheres illustrate the angle-dependence of the electron density in a $3d_{xy}$ state. (Reprinted with permission from [Keeler08]. The CC license does not apply.)

Energy-Distribution of Spectral Features

As described at the beginning of this subsection, the photoexcitation process was so far only treated for a single electron in an environment which is not changing during the photoemission process. However, this assumption is not valid in reality, where electronic correlations play a significant role. Examples with properties that are dominated by electronic correlations are ferromagnets or high- T_C superconductors. In this case, Eq. 2.16 can not be used in the simple, single-electron form anymore, because the involved states correspond to a multiparticle system. The situation of this system differs for the initial state, where the electron is still at its origin in the system of N electrons, and the final state, where it is excited and leaves behind a

positive hole resulting in a rearrangement of the remaining $N-1$ electrons. Assuming that the situation of an $N-1$ electron system with a positive hole remains unchanged until the photoemission process is finished ("sudden approximation"), this effect can be treated by introducing an additional factor into Eq. 2.16 that replaces the Dirac delta function¹⁴. It is usually called "spectral function" $A_{sf} = A_{sf}(E)$ and takes into account the probability of the system to change from the ground to the particular excited situation. Within this framework, the description of the photoexcitation is again reduced to a single-electron process. Based on a Green's function approach, the form of A_{sf} can be determined [Schneider12]:

$$A_{sf} = -\frac{1}{\pi} \frac{\text{Im}(\Sigma)}{(E - E_0 - \text{Re}(\Sigma))^2 + (\text{Im}(\Sigma))^2}. \quad (2.24)$$

Here, $\Sigma = \Sigma(E)$ is the "complex self-energy" that can contain various interactions of the electron, *e.g.* with other electrons or phonons. Its real part $\text{Re}(\Sigma)$ introduces a shift of the energetic position of spectral features, which would be located at E_0 without electron correlations. Moreover, the imaginary parts $\text{Im}(\Sigma)$ introduces a line broadening compared to the sharp Dirac delta function in Eq. 2.16, which represents the life time of the excited state.

2.2.2 Description within a One-Step Model

The separation of the photoemission process into three independent steps as described in Sec. 2.2.1 is a very successful approach for a qualitative understanding of the underlying mechanisms. However, in reality this strict separation is not exact and for a proper quantitative modeling of experimental results it has some limitations, especially in dealing with the scattering of the excited electrons in the material and at the surface. Besides, some important effects like the SOC are not inherently included, as discussed in Sec. 2.2.1 (step 1). Therefore, a complete quantum mechanical treatment within one single step using a suited initial and final state is more appropriate for a quantitative picture.

In general, such models are based on the excitation described in Eq. 2.16 and approximate the initial state with a Bloch wave function and the final state using a so-called inverse low-energy electron diffraction (LEED) function (see Fig. 2.7). The latter combines a free-electron plane wave in the vacuum with an adequate wave function inside the crystal. This can be a Bloch state if a band is present at the given energy resulting in only a weak damping of the wave function from the surface into the crystal. Here, the damping is dominantly caused by electron-electron scattering and represents the situation described by the IMFP model in Sec. 2.2.1. In the case where no Bloch states are available, the wave function is strongly damped inside the crystal and only an evanescent part extends from the surface. Transitions into such

¹⁴Details are given, *e.g.*, in [Damascelli04].

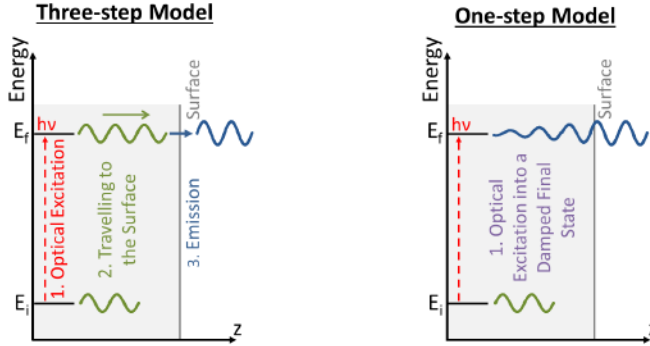


Figure 2.7: Comparison of the three- and the one-step model of photoemission. In the three-step model, the photoemission process is divided into three independent parts. In the one-step theory, on the other hand, these are treated all together within the excitation by an appropriate modelling of the involved states. (based on [Hüfner95])

states are thus only happening close to the surface. The name "inverse LEED state" is used, because the situation of the emitted electron in photoemission is similar to a LEED process with a suppressed reflection component and under time-reversal. Therefore, the corresponding theoretical framework can be applied.

2.2.3 Spin Detection of Photoelectrons

As already mentioned, experimentally observing the spin polarization \vec{P} of photoelectrons can provide valuable information about the magnetic properties of the electron system¹⁵. In general, during the excitation of the photoelectron its spin is conserved, because a transition is only possible between bands with the same spin character. However, a hybridization of bands due to the SOC can induce a significant amount of mixing between the spin properties of states that are otherwise purely polarized (see step 1 in Sec. 2.2.1). Moreover, the properties of the final band play an important role. If results are interpreted on the basis of band structure calculations in order to reveal the character of the initial state, these effects have to be considered. In addition, inelastic scattering processes during the transport to the surface can induce a change of the spin polarization of the photoelectrons especially in ferromagnets, because the band structure and thus the scattering probability is different for the majority and minority spin direction. Nevertheless, this effect is

¹⁵The following discussion only includes the effects leading to a change of the spin polarization, which are most relevant for the situation treated in this work. It is based on the more detailed considerations in [Osterwalder06], where also other mechanisms are reviewed.

not present for the undisturbed electrons, which are in particular interesting in PES (see step 2 in Sec. 2.2.1). Another mechanism that can induce a change of \vec{P} is the correlation inside the electron system. The influence of this correlation, which was described at the end of Sec. 2.2.1, can be strongly spin-dependent in ferromagnets and thus lead to significant changes in measured (spin-resolved) photoemission spectra (see Sec. 4.2).

Still, the mentioned effects are often not strongly disturbing the spin polarization of the photoelectrons or can be considered in the interpretation. Consequently, measuring the spin polarization disentangles the information about the magnetic properties of states in many cases. The concepts that are commonly used in order to detect \vec{P} are based on the creation of a spin polarization-dependent imbalance between two intensities I_1 and I_2 , *e.g.* measured at different positions in space or using different experimental conditions. Then, the asymmetry

$$A = \frac{I_1 - I_2}{I_1 + I_2} \quad (2.25)$$

and the spin polarization along the sensitive direction of the detector¹⁶

$$P = \frac{A}{S} \quad (2.26)$$

can be determined by measuring the corresponding intensities. S is often called "Sherman function" and is a property of the detector which varies with the kinetic energy of the photoelectrons. The value represents the ability of the detector to separate the photoelectrons with respect to the spin polarization ratio projected along or opposite to the sensitive direction of the polarimeter. S takes into account the characteristics of the scattering process under the given conditions. It is directly related to the asymmetry that is measured for a fully spin-polarized electron beam and can be experimentally determined using A recorded for a well-known spin polarization, for example of electrons created by a GaAs photocathode or in the secondary photoelectrons from a ferromagnet. For the comparison of the efficiency of different spin detectors a figure of merit (FoM)

$$FoM = \frac{I}{I_0} S^2 \quad (2.27)$$

is defined that takes into account S and the intensity I of electrons which are scattered into the detector (normalized to the incoming intensity I_0). The spin-orbit- as well as the exchange interaction in a target material are well-established detection mechanisms in spin polarimeters. In the following, the three most commonly used concepts of spin detectors will be introduced.

¹⁶In the following, the term "spin polarization" and all spin polarization values refer to this projection.

In a Mott detector, the spin-orbit interaction during a scattering process at single nuclei is used to create a spin polarization-dependent difference in the intensity on two electron counters. The differential cross section $d\sigma/d\theta$ of such processes can be calculated in analogy to the quantum mechanical treatment of scattering in textbooks [Nolting13]. However, since the spin properties of the electron are considered, the relativistic Dirac- and not the Schrödinger-equation has to be solved [Kessler85]. The result is given by

$$\frac{d\sigma}{d\theta} \propto (1 + S(\theta)P_{\perp}) \quad (2.28)$$

with a Sherman function S that depends on the scattering angle θ . P_{\perp} denotes the component of the spin polarization that is perpendicular to the scattering plane spanned by the trajectories of the incoming and outgoing electrons. For two fixed scattering angles $\theta_2 \neq \theta_1$ and particularly for $\theta_2 = -\theta_1$, the term introduced by the SOC can result in different scattering probabilities for spin-up and spin-down electrons¹⁷. This leads to the desired imbalance in the electron beam intensity. With two additional electron counters spanning the perpendicular scattering plane, two orthogonal components of \vec{P} can be measured simultaneously. In order to build an efficient Mott detector, the SOC-related part of the scattering has to be maximized [Huang93]. According to Eq. 2.11 and Eq. 2.12, the two main parameters determining the strength of the SOC are the speed of the electrons towards the target and the atomic number Z of the nucleus. Therefore, in Mott detectors the electrons are typically accelerated to several tens of keV and then hit a target with a high Z , *e.g.* a Au foil. The scattered electrons are measured at an angle of around $\pm 120^\circ$, where the FoM has a peak [Qiao97]. Typical values for the FoM that can be reached with non-radioactive targets are around $2 \cdot 10^{-4}$ [Huang02].

The second widespread detector design is based on spin-polarized low-energy electron diffraction (SPLEED). Here, also the SOC is used to create an intensity imbalance, but the scattering in this case is performed on a periodic crystal structure with electrons having a de-Broglie wavelength close to the lattice constant of the material. This leads to interference effects and thus a modulation of the angular distribution of the scattering cross section. The modulation helps to overcome a general problem of Mott scattering, where a high value of the Sherman function is connected to low cross sections [Kessler85]. SPLEED detectors have a FoM that is comparable to the one of Mott detectors ($\text{FoM} \approx 2 \cdot 10^{-4}$ [Johnson07]), but usually operate at lower electron energies (≈ 100 eV for the typically used $W(001)$ single crystalline scattering target) allowing a more compact design. On the other hand, the low kinetic energy and therefore short penetration depth makes the process extremely surface sensitive and small surface changes or contaminations significantly influence the detector properties. Consequently, a cleaning of the target is necessary after a few hours of operation.

¹⁷Spin-up and spin-down are here defined with respect to the direction of P_{\perp} .

The third type of detector, which recently started to play an important role for spin polarization detection and is used for the presented work (see Sec. 3.2.2 for details), is based on the influence of the exchange splitting on the reflection of electrons [Tillmann89, Hillebrecht90]. Here, the electrons are guided to a ferromagnetic material with very low kinetic energy (≈ 10 eV, very low-energy electron diffraction (VLEED)) and the intensity of the specular reflection is recorded. Since our detector employs an (oxidized) Fe(001) film for the scattering, the following explanations focus on this target material. A typical experimental situation is shown on the left side of Fig. 2.8. For a spin-polarized electron beam, the measured intensity differs for measurements with a parallel and an antiparallel alignment between the magnetization of the target and the dominant spin direction of the incoming electrons. Again, this imbalance can be used to calculate the spin polarization. In order to understand the underlying effect, the reflected intensities can be treated similar to an inverse photoemission process and thus directly related to the ferromagnetic band structure [Tamura86]. For the low electron energies, the relevant part of the band structure is still dominated by distinct bands at energies slightly above the vacuum level. Similar to the argumentation for normal photoemission in Sec. 2.2.1 (step 3), electrons that impinge on the target in normal incidence can only be absorbed if a coupling to a high symmetry state in the material is possible. In the top right part of Fig. 2.8, the k_{\perp} -dependence of the states with Δ_1 symmetry in Fe(001) is shown for $k_{\parallel} = 0$ as a function of the electron energy for several eV above the vacuum level. The band structure exhibits a shift of the majority and minority spin electrons towards each other due to the exchange interaction and a gap between the bands labeled with H_{15} and H_{12} is present. The influence of this band gap on the electron absorption can be seen in the IPES spectra taken by Bertacco *et al.* [Bertacco99a] for the relevant energy region, which are shown in the bottom right part of Fig. 2.8. Here, the two curves labeled with "IPES" represent measurements employing an electron beam with a spin polarization parallel and antiparallel to the magnetization direction of the target. In particular, at the onset of the H_{15} -band a clear enhancement of the IPES signal compared to the region of the band gap is visible (labeled "C"). In IPES, a higher signal means an increased absorption of the incoming electrons. In addition, the spin resolution of the IPES measurement reveals that the peak at feature C is shifted for the two incoming spin polarizations. This is in good agreement with the band structure calculation in the top part of the figure that predicts a different energetic position of the minority and the majority H_{15} -band. Therefore, at $E - E_F = 10$ eV only states for minority spin electrons are available for absorption, and the majority spin electrons are mainly reflected. In a direct measurement of the reflected electron current (RC), the resulting asymmetry function reaches values up to +20% at this energies (see inset in the bottom right part of Fig. 2.8, also shown: absorbed electron current (AC)).

The high asymmetry values, together with a high reflectivity for the electrons polarized parallel to the magnetization direction of the target, are well-suited for the

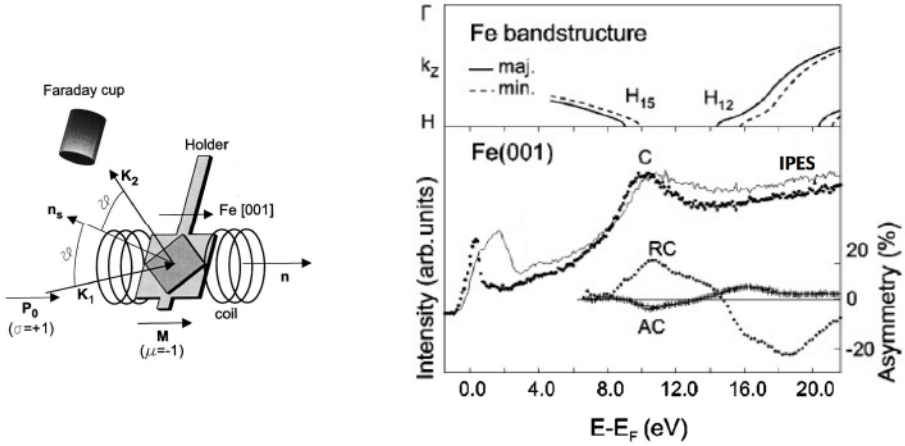


Figure 2.8: Left: Typical geometry of the exchange scattering used in spin detectors. The incoming electron beam K_1 is reflected from an Fe(001) target under a small angle ϑ . The intensity of the reflected beam K_2 is then measured. Using a field pulse induced by the coil, the magnetization M of the target can be adjusted parallel or antiparallel to the spin polarization P_0 of the incoming electrons. (Reprinted from [Bertacco99b] with permission of AIP Publishing. The CC license does not apply.) Top right: High-symmetry states available for the absorption of electrons entering an Fe(001) crystal in normal incidence. The states are shown as a function of the electron energy, spin character and momentum component perpendicular to the surface. (Adapted with permission from [Bertacco99a]. Copyright by the American Physical Society. The CC license does not apply.) Bottom right: Corresponding inverse photoelectron spectroscopy intensity. The two lines in the IPES spectra represent the results for two opposite spin directions of the incoming electron beam. As an inset, the asymmetry in the reflected electron current (RC) and the absorbed electron current (AC) between both measurements is shown. (Adapted with permission from [Bertacco99a]. Copyright by the American Physical Society. The CC license does not apply.)

application in a spin detector. The usability of spin detectors based on this principle was further enhanced by carefully oxidizing the Fe surface [Bertacco99a], since this passivates the reactive Fe and makes a usage over several weeks of operation possible without repreparing the target. Moreover, the oxidation even enhances the efficiency of the detectors [Bertacco99a]. The FoM then reaches up to $1 \cdot 10^{-2}$ per spin component¹⁸ [Okuda08]. In summary, the exchange interaction-based design is more than one order of magnitude more efficient than the SOC-based devices and in addition overcomes their problems like the need for high voltage (Mott-type) or the regular refreshing of the target (SPLEED-type). Furthermore, one of the key advantages of spin polarimeters employing exchange scattering is that so-called

¹⁸If two orthogonal spin directions have to be measured, the FoM reduces to half of the value, because two consecutive measurements are necessary in contrast to Mott- or SPLEED detectors.

“instrumental asymmetries” have negligible influence on the spin polarization because the intensity imbalance is created by switching the target magnetization in subsequent measurements. Therefore, no mechanical changes are necessary and the devices are, in contrast to SPLEED or Mott detectors, usually built with only a single electron counting system. Consequently, intensity differences between the measurements of I_1 and I_2 due to, *e.g.*, varying geometries or channeltron efficiencies are very small. This is in particular useful for measurements of magnetic effects in the band structure of materials that do not show ferromagnetism since in this case instrumental asymmetries can not be compensated by remagnetizing the sample. For the sake of completeness, a new development in the design of spin detectors has to be mentioned. In recent years, detectors that are capable of conserving the angular information of a photoelectron during the spin-dependent scattering process were developed (2D spin detectors). Their working principle is closely related to that of a conventional SPLEED detector. However, they use the target as an image-conserving electron mirror to carve out the spin information of the full picture from a real- or momentum-space microscope at the same time [Tusche11, Kutnyakhov13]. If a broad range of position or momentum values is of interest, this multi-channel detection approach allows far higher efficiencies than subsequent conventional, zero-dimensional spin detection measurements. Since their first realization employing W or Ir targets, which again have the disadvantage of a regular need for cleaning, the technique improved further and detectors providing stable conditions over several month using a Au-passivated Ir(001) surface have been demonstrated. For each pixel of a two-dimensional distribution, the FoM in this detector type can reach values above $1 \cdot 10^{-3}$ [Vasilyev15].

2.3 Laser-Based High-Order Harmonic Generation

In the photoemission process, which is the subject of the previous section, the photoelectron is released from a material by the absorption of light. In order to perform time-resolved studies, this light has to be provided in short pulses. Furthermore, a photon energy $\gg 5\text{ eV}$ is necessary for the investigation of the entire valence bands. Laser-based HHG is one of the most promising techniques for the creation of sub-picosecond light pulses in the XUV spectral range covering energies from 10 eV to 120 eV. Typical values for the key parameters of HHG sources are listed in Tab. 2.2 together with reference data for comparable light sources, namely free-electron lasers (FELs) and femtoslicing at synchrotron.

The table shows that FELs provide by far the highest photon flux of the introduced sources. On the other hand, the total number of photons is distributed over a small number of pulses resulting in a huge pulse intensity. For photoemission experiments,

2.3. LASER-BASED HIGH-ORDER HARMONIC GENERATION

Table 2.2: Key parameters of light sources for femtosecond extreme ultraviolet pulses. HHG sources provide a high photon flux at moderate energies per pulse.

| | HHG | FEL | Synchrotron Femtosing |
|----------------------------|----------------------------|-----------------------|---------------------------------|
| Photon Flux (photons/s) | $< 10^{14}$ [Hädrich14] | $< 10^{16}$ [SLAC] | $< 10^{13}$ [Quast07, BESSY] |
| Repetition Rate (kHz) | < 100000 [Gohle05] | < 0.12 [SLAC] | < 4 [ALS] |
| Pulse Duration (fs) | > 0.07 [Zhao12] | > 30 [FLASH] | > 75 [ALS] |
| Photon Energy (keV) | < 1.6 [Popmintchev12] | < 15 [SACLA] | < 14 [SLS] |

this is a clear drawback since the produced dense clouds of photoelectrons create artifacts in the measured energy- and angular distribution curves as will be shown in Sec. 5.3. Hence, only a limited number of photons per pulse can be used and the total intensity has to be reduced even below the photon flux of sources operating at higher repetition rates.

On the other side, the photon flux that can be reached using laser-based HHG still exceeds the intensity of synchrotron femtoslicing. In addition, the repetition rates that can be reached are high. For photoemission experiments several kHz are the standard [Mathias07, Rohwer11, Gierz13, Frietsch15] and even some MHz were already demonstrated in optimized schemes¹⁹ [Chiang12, Hädrich14]. This is significantly higher than the repetition rate of current FELs. A clear limitation of the light created by HHG compared to the other sources is the low maximum photon energy²⁰ of around 100 eV and that, so far, circularly polarized light is not available with reasonable high photon flux²¹.

However, the range of available photon energies exceeds typical work functions of metals still by far and opens up the full range of ultraviolet photoelectron spectroscopy (UPS) experiments exploring the valence band structure. In addition, even the $3p$ core-levels of the $3d$ ferromagnets Fe, Ni and Co, which are particularly interesting for magnetic studies, can be reached. The lack of circularly polarized light, which would enable magnetically sensitive measurement techniques like x-ray magnetic circular dichroism (XMCD), is also not limiting the presented studies, because our goal is a direct detection of the spin of the photoelectrons. In addition,

¹⁹It is further remarkable that Hädrich *et al.* achieved a high repetition rate and very bright harmonics at the same time.

²⁰Higher photon energies can be reached, but with a flux that is not sufficient for photoemission experiments at present [Popmintchev12].

²¹Recently, first experiments showed ways to produce bright XUV radiation with circular polarization from HHG [Vodungbo11, Grychtol14, Kfir15].

HHG can be realized in a laboratory-based tabletop arrangement whereas FELs and femtoslicing in synchrotrons need large-scale facilities. This fact results in an easier handling and individual tuning to match the experimental needs as well as a higher temporal availability of the photon beam without the dependence on limited beamtimes. Altogether, the combination of a bright average photon flux with high repetition rates and the superior temporal resolution makes laser-based high-order harmonic generation at the moment the technique of choice for ultrafast photoemission studies.

To trigger the HHG process, short and very intense laser pulses are focused into a noble gas, where a non-linear energy conversion takes place. In the presented setup (see Sec. 3.1), we use Ar gas as the conversion medium, which is confined in a capillary waveguide. The source can be driven by fundamental laser light with a wavelength of $\lambda_1 = 780$ nm or $\lambda_2 = 390$ nm. Nevertheless, the considerations in Sec. 2.3.1 and Sec. 2.3.2 are in general valid, whereas the special situation for the $\lambda_2 = 390$ nm light will be discussed in Sec. 2.3.3. A characteristic energy spectrum of the light created by HHG is shown in Fig. 2.9. It consists of a comb of intensity peaks that are separated by twice the fundamental photon energy of the laser. The amplitude drops fast for low harmonic orders ("perturbative regime"), then it stays almost constant over a wide range ("plateau") until it reaches the "cut-off" region, where it again decreases.

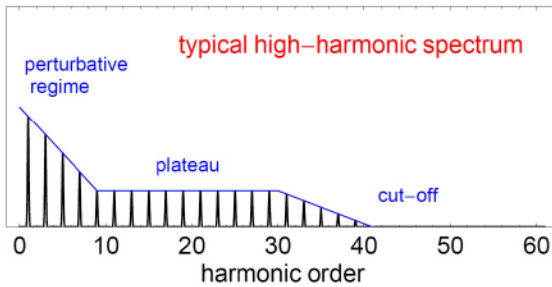


Figure 2.9: Typical light spectrum created by high-order harmonic generation. The intensity distribution is plotted as a function of the harmonic order. (Reprinted with permission from [Winterfeldt06]. The CC license does not apply.)

2.3.1 Three-Step Model of High-Order Harmonic Generation

The next paragraphs will introduce the so-called "three-step model", which is capable of explaining most of the key properties of HHG radiation by the reaction of a single electron to the laser field. The framework of this quasi-classical theory is based on [Corkum93, Kulander93], however, the argumentation in this section will follow the summary of Pfeifer *et al.* [Pfeifer06]. A quantum mechanical description of the

2.3. LASER-BASED HIGH-ORDER HARMONIC GENERATION

process has been developed as well. Nevertheless, the semi-classical approach relates the light properties more transparently to the underlying processes and yields results that differ only slightly from the quantum mechanical calculations. In the three-step model, the conversion process is divided into three independent parts: (1) the atom is ionized and releases an electron, (2) this electron is accelerated in the electric field of the laser pulse, and (3) the electron recombines with the parent ion under the emission of XUV radiation.

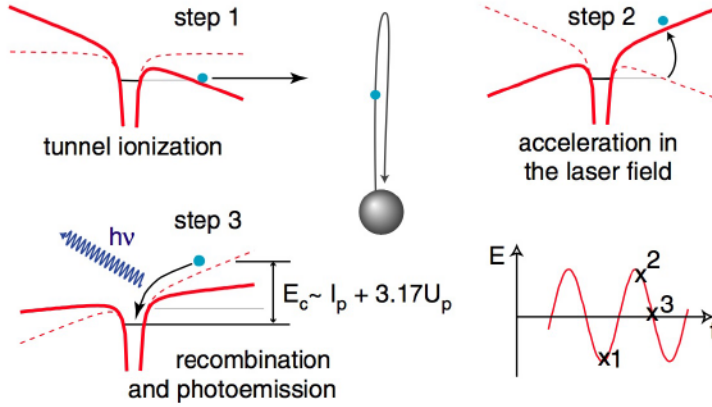


Figure 2.10: Three-step model describing high-order harmonic generation. First, the strong electric field of the laser pulse modifies the core-potential of the noble gas ion allowing for tunnel-ionization (step 1). Then, the freed electron is accelerated in the electric field of the laser. Due to its sinusoidal form, the laser field reverses its direction after some time and drives the electron back towards the ion (step 2). For the cases where the electron passes the position of the ion, there is a probability for recombination resulting in the emission of a photon carrying the potential energy and the kinetic energy that the electron gained in the laser field (step 3). (Reprinted with permission from [Pfeifer06]. Copyright by IOP Publishing. The CC license does not apply.)

Step 1: Tunnel-Ionization

In the first step, the electron has to be detached from the atomic core potential. Since this potential is higher than the used laser photon energy of 1.6 eV to 3.2 eV, two different mechanisms are most probable to trigger this process: multiphoton excitation or tunnel ionization. Which process is dominating in the regime of HHG can be estimated by the so-called "Keldysh parameter"

$$\gamma = \sqrt{\frac{I_p}{2U_p}}. \quad (2.29)$$

Here, I_p represents the ionization potential of the atom and

$$U_p = \frac{e^2 E_0^2}{4m_e \omega^2} \quad (2.30)$$

the ponderomotive potential of the laser with ω being the frequency and $E_0 = \sqrt{2/(c \cdot \epsilon_0)} \cdot I$ the amplitude of the electric field of the laser pulse. The intensity is denoted by I and the constants c , ϵ_0 , e and m_e have their usual meaning as the speed of light, the vacuum permittivity, the elementary charge and the electron mass, respectively. If the laser-induced potential U_p is much lower than the ionization potential I_p (and thus $\gamma \gg 1$), multiphoton absorption takes mainly place. On the other hand, tunnel ionization is dominant for laser fields causing ponderomotive potentials that strongly exceed the ionization potential ($\gamma \ll 1$).

Calculating the ponderomotive potential using Eq. 2.30 for laser parameters typically reached in our setup²² yields $U_{p1} \approx 134$ eV and $U_{p2} \approx 13$ eV for the fundamental wavelengths $\lambda_1 = 780$ nm and $\lambda_2 = 390$ nm, respectively. Together with the ionization potential of the Ar gas ($I_p = 15.8$ eV [Gibson04]), the Keldysh parameter can be determined as $\gamma_1 = 0.24$ and $\gamma_2 = 0.79$. Even though γ_2 is already close to unity and multi-photon processes start to be important here [Gkortsas11], both values are smaller than 1 and thus in the regime dominated by tunnel-ionization. Here, the core potential is bent due to the high electric field of the laser (see Fig. 2.10, step 1) and only an energy barrier with finite width holds the electrons back from leaving the core. An electron can then tunnel through the remaining barrier.

Step 2: Acceleration in the Laser Field

Once the electron has left the atomic potential, it can be treated as free and, for the laser intensities that are reached, it can be described non-relativistically. It is then accelerated by the electric field E of the laser pulse away from the ion. However, since the electric field follows a sinusoidal shape, its direction turns after some time and the electron travels back towards the parent ion. Using the Newtonian mechanics $F = eE = ma$ to describe this harmonic motion in the laser field, the expression

$$x(t) = \frac{eE_0}{m_e \omega^2} (\cos(\omega t + \phi) - \cos(\phi)) + \frac{eE_0}{m_e \omega} \sin(\phi)t \quad (2.31)$$

can be derived for the time-dependent position of the electron with ϕ describing the phase of the electric field at the time of ionization. The meaning of the other variables is identical to Eq. 2.30. Using the derivative of Eq. 2.31 and $E_{kin} = 0.5mv^2$, the expression for the ponderomotive energy in Eq. 2.30 can be derived by averaging

²²For the evaluation a pulse energy of $I_1 = 1.6$ mJ/ $I_2 = 0.6$ mJ for the 780 nm/390 nm beam is used. The pulse duration is considered as $\Delta t_1 \approx \Delta t_2 \approx 35$ fs and the focused beam diameter as $d_1 \approx d_2 \approx 50$ μ m.

over a cycle of the electric field²³. In addition, the maximum kinetic energy that the electrons reach can be determined as $E_{kin,max} = 8U_p$.

Step 3: Recombination

By plotting the position of the electron versus time, it can be illustrated for which values of ϕ a recombination with the parent ion is possible. Only trajectories that pass the position of the ion ($x = 0$) again, can contribute to the HHG process. In Fig. 2.11, electron trajectories calculated using Eq. 2.31 with $\omega = 1$ and $eE_0/m_e = 1$ are plotted for selected values of ϕ .

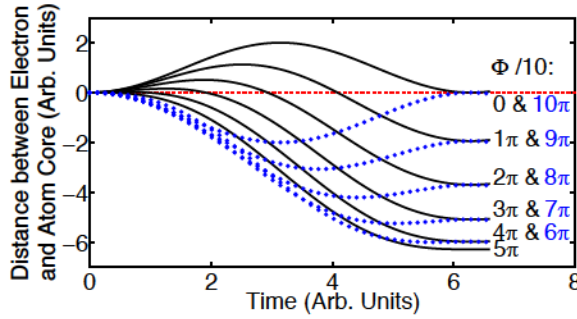


Figure 2.11: Electron trajectories in the HHG process for different phases of the electric field of the laser pulse at the time of ionization. For phases in the range of $0 \leq \phi < \pi/2$ (black lines), the electron returns to the position of the atom core and a recombination is possible. In contrast, the electron drifts away from the atomic core without returning to the position of the atom core for phases between $\pi/2 \leq \phi < \pi$ (blue dots). For ionization times with phases in the second half cycle of the electric field of the laser ($\pi \leq \phi < 2\pi$), the same behavior can be derived. (based on [Pfeifer06])

It can be seen that $x = 0$ has only a solution if $0 \leq \phi < \pi/2$. For the other phases, the constant drift velocity term ($x(t) \propto \sin(\phi)t$) prevents a recombination. The second half-cycle of the laser field ($\pi \leq \phi < 2\pi$) shows the same dependence and only electrons that are ionized at a phase of $\pi \leq \phi < 3\pi/2$ recombine. However, here the position of the electron has opposite sign compared to the first half-cycle. The fact that the HHG process can happen twice within one laser cycle explains already the separation of the harmonic peaks of the emitted light (see Fig. 2.9 again). Taking into account that, in our case, the HHG light is created by a laser pulse consisting of several full-cycles, the produced femtosecond XUV pulse is constructed by several light bursts that are produced twice each cycle. This results in a time

²³Any constant drift velocity is neglected since only the gained energy due to the wiggling in the laser field contributes to the ponderomotive energy.

delay between the bursts of $\Delta t = T/2$, with T being the period of the electric field. From this time structure, the separation of

$$\Delta f = 2\omega \quad (2.32)$$

in the spectral distribution results directly through a Fourier transform.

Besides the explanation of the separation between the harmonics, the maximum kinetic energy that the electron is able to reach at $x = 0$ can be determined numerically using the trajectories in Eq. 2.31. The result is $E_{max,x=0} = 3.17U_p$ for $\phi = 0.1\pi$.

Furthermore, the photon energy after recombination is given by the sum of the ionization potential of the atom I_p , which is gained when the electron recombines, and the kinetic energy that the electron has at the time of recombination E_{kin} . Consequently, the maximum photon energy that can be achieved with HHG ("cut-off energy") is

$$h\nu_{cut-off} = I_p + 3.17 \cdot U_p. \quad (2.33)$$

This quantity can thus be tuned by decreasing the laser frequency ω , by increasing the laser intensity E_0 or by changing the noble gas and therefore I_p . However, the cut-off energy can be significantly reduced by destructive interference due to a phase mismatch of the fundamental laser and the HHG light (see Sec. 2.3.2 and [Rogers08, Falcão-Filho10] for further details). It also has to be mentioned that not all electrons passing $x = 0$ will recombine and that most electrons will remain free.

2.3.2 Phase Matching Conditions

One important condition that has to be fulfilled for efficient HHG is that the fundamental laser light and the created XUV radiation travel in-phase through the gas because the high energy photons created at different positions along the capillary should interfere constructively. Hence, the difference between the wave vectors for both wavelength has to be minimized²⁴. A wavelength dependence of the wave vector in the case of HHG is mainly given in the terms accounting for the neutral dispersion in the gaseous conversion medium (k_{disp}), for the geometric situation defined by the capillary waveguide (k_{geom}) and for the plasma that is created by the ionization of the atoms (k_{plasma}). Altogether, this leads to the expression

$$\Delta k = \Delta k_{disp} + \Delta k_{geom} + \Delta k_{plasma} \quad (2.34)$$

for the total difference of the wave vector of the fundamental light and the m -th harmonic with the partial contributions

$$\Delta k_i = mk_i(\omega_f) - k_i(m\omega_f). \quad (2.35)$$

²⁴Again, the explanations in this subsection are based on the argumentation given in [Pfeifer06].

2.3. LASER-BASED HIGH-ORDER HARMONIC GENERATION

The wave vector k is directly related to the refractive index n via

$$k(\omega) = (n(\omega) - 1) \frac{\omega}{c}, \quad (2.36)$$

where c is the speed of light in vacuum. The wave vector mismatch in Eq. 2.34 can be minimized or even canceled out with a careful adjustment of the single terms since they have different signs ($\Delta k_{disp} > 0$, $\Delta k_{geom} < 0$, $\Delta k_{plasma} < 0$). This can be realized, *e.g.*, by varying the pressure of the noble gas or changing the position of the laser focal point. However, since the terms change for varying wavelengths, the phase matching can always only be perfectly achieved for one of the created harmonics. This, on the other hand, makes it possible to enhance or suppress parts of the HHG spectrum depending on the particular needs. In the following, the contributions to the wave vector mismatch will be explained separately in more detail.

Neutral Dispersion k_{disp}

According to Eq. 2.36, the wavelength-dependence of the refractive index leads to a difference in the wave vectors for the fundamental and the harmonic light. For wavelengths in and close to the visible range, the refractive index of a material can be approximately described by the Sellmeier equation. However, this fails for the situation close to or at resonances. A deeper insight into the refractive indices for the energy ranges relevant for HHG is given in [Rogers08]. In general, the refractive indices are smaller than 1 in the XUV range ($n_h < 1$) and larger than 1 in the visible and near-infrared (NIR) range ($n_f > 1$). Table 2.3 summarizes typical values for the refractive indices at photon energies relevant for the presented work. Using Eq. 2.35 and Eq. 2.36, the resulting difference in the wave vector is given by

$$\Delta k_{disp} = m k_{disp}(\omega_f) - k_{disp}(m\omega_f) = (n(\omega_f) - n(m\omega_f)) \frac{m\omega_f}{c} > 0 \quad (2.37)$$

and gives always a positive contribution to Eq. 2.34.

Table 2.3: Refractive indices for fundamental (n_f) and harmonic (n_h) radiation in the HHG process and the resulting wave vector mismatch. The values are calculated for Ar at room temperature. (taken from [Rogers08] and converted to a pressure of $P = 50$ mbar using $n = 1 + (n_0 - 1)P/P_0$ with n_0 being the refractive index at the reference gas pressure P_0)

| | $n_f - 1$ | $n_h - 1$ |
|---|----------------------|----------------------|
| $\lambda_1 = 780 \text{ nm}$ ($h\nu_h = 40 \text{ eV}$) | $1.4 \cdot 10^{-5}$ | $-0.7 \cdot 10^{-5}$ |
| $\lambda_2 = 390 \text{ nm}$ ($h\nu_h = 20 \text{ eV}$) | $1.45 \cdot 10^{-5}$ | $-2.6 \cdot 10^{-5}$ |

Geometric Dispersion k_{geom}

The second contributing to the wave vector mismatch, Δk_{geom} , is induced by focusing and confining the laser light into the capillary waveguide. Solving the Maxwell

equations for the laser beam inside the waveguide with the corresponding boundary conditions gives as a solution, according to [Marcatili64], a set of modes with wave vectors defined by

$$k_{geom} = \frac{2\pi}{\lambda} \left(1 - \frac{1}{2} \left(\frac{u_{nl}\lambda}{2\pi a} \right)^2 \right). \quad (2.38)$$

Here, a is the inner radius of the capillary, λ the light wavelength and u_{nl} is defined using the Bessel functions J by the l -th root of $J_{n-1}(u_{nl}) = 0$. For the difference of the wave vectors, this and Eq. 2.35 gives the expression

$$\Delta k_{geom} = mk_{geom}(\omega_f) - k_{geom}(m\omega_f) = \frac{u_{nl}^2 c}{2a^2 m \omega_f} (1 - m^2) < 0. \quad (2.39)$$

Obviously, the prefactor has only positive contributions and the harmonic order is > 1 , which results in a negative term for the wave vector mismatch.

Plasma Dispersion k_{plasma}

As explained in the three-step model, during the HHG process electrons are detached from their atomic core (step 1) and since most of them do not recombine (step 3) the formerly gaseous conversion medium is partly left in a plasma state. The resulting free charges (electrons and ions) are then separated spatially by the electric field and create a change of the refractive index leading to

$$n_{plasma}(\omega) = \sqrt{1 - \left(\frac{\omega_p}{\omega} \right)^2} \approx 1 - \frac{1}{2} \left(\frac{\omega_p}{\omega} \right)^2. \quad (2.40)$$

Here, ω_p is the plasma frequency, which is proportional to the square root of the density of free electrons N_e ($\omega_p^2 \propto N_e$). The linear approximation ($(1+x)^n \approx 1+nx$ for $|x| \ll 1$) in Eq. 2.40 is valid since the laser as well as the XUV radiation create only small electron densities N_e compared to the critical density $N_c \propto \omega^2$ ($N_c = 1.75 \cdot 10^{21} \text{ cm}^{-3}$ [Pfeifer06]). Calculating the wave vector mismatch from Eq. 2.40, Eq. 2.35 and Eq. 2.36 gives

$$\Delta k_{plasma} = mk_{plasma}(\omega_f) - k_{plasma}(m\omega_f) = \frac{\omega_p^2}{2cm\omega_f} (1 - m^2) < 0. \quad (2.41)$$

This term is again always negative since the regarded harmonic order m is always larger than 1 and the coefficients are all positive.

2.3.3 Wavelength-Dependence of High-Order Harmonic Generation

Driving the HHG source with a wavelength of $\lambda_2 = 390 \text{ nm}$ compared to the operation with $\lambda_1 = 780 \text{ nm}$ laser light leads to several notable differences. First, from

2.3. LASER-BASED HIGH-ORDER HARMONIC GENERATION

Eq. 2.33 and Eq. 2.30 follows a quadratic dependence of the maximum photon energy on the inverse of the wavelength of the fundamental laser ($h\nu_{cut-off} \propto 1/\omega^2$). Thus, the maximum cut-off energy is significantly reduced for shorter wavelengths. Second, the harmonics are still separated by twice the photon energy leading to a spacing of the intensity peaks that is doubled for the $\lambda_2 = 390\text{ nm}$ beam ($2\omega_{f2} \hat{=} 6.4\text{ eV}$) compared to the operation with 780 nm laser light.

Finally, the conversion efficiency in the HHG process scales with the wavelength. A dependence following λ^{-6} for the plateau and λ^{-5} for the cut-off region was found by Falcão-Filho *et al.* [Falcão-Filho10]. This leads to an increase of the photon flux by one to two orders of magnitude for changing the fundamental wavelength from 780 nm to 390 nm. Thus, the loss of intensity caused by the conversion efficiency of the second harmonic generation (SHG) in a $\beta\text{-BaB}_2\text{O}_4$ (BBO) crystal, which is typically around 30%, is by far overcompensated. Moreover, the authors in [Falcão-Filho10] show that the conversion efficiency reaches its maximum value already for low pumping powers if 400 nm light is used and stays constant over a broad intensity range. This saturated operation regime is preferable when pumping the energy-upconversion with a laser amplifier system, because (pulse-to-pulse) laser intensity fluctuations as well as intensity drifts are not enhanced in a non-linear way. Most of the features induced by driving the HHG source with shorter wavelengths and, in particular, the advantages for photoemission are further discussed and experimentally tested in [Eich14].

3 Experimental Setup

The considerations in the last chapter already outlined the main parts of the experiments. First, femtosecond extreme ultraviolet (XUV) light pulses have to be provided for the excitation of the photoelectrons from the valence bands. Second, a detection system capable of measuring their kinetic energy and spin is needed to disentangle the magnetic properties. These conditions are fulfilled by the setup sketched in Fig. 3.1, which is used for the photoemission experiments and described in the following¹. Section 3.1 deals with the light source based on high-order harmonic generation (HHG). The ultrahigh vacuum (UHV) environment containing the equipment necessary for the photoelectron spectroscopy (PES) experiments and *in situ* sample preparation is introduced in Sec. 3.2.

3.1 Monochromatic Femtosecond-Pulsed Extreme Ultraviolet Light Source

The basis of the femtosecond XUV light source is a laser amplifier system (Dragon, KMLabs). In order to create intense, ultrashort laser pulses it uses chirped pulse amplification. This means that single pulses from a femtosecond-pulsed seed laser are first stretched in time, then enhanced by guiding them several times through an additional, strongly pumped crystal, and finally compressed back to the desired pulse duration. As active media, our laser system uses Ti^{3+} -doped Al_2O_3 crystals (Ti:sapphire) in the seed laser as well as in the amplification stage. In the presented work, the laser was used to create light pulses with a duration of 35 fs, a central wavelength of 780 nm and a pulse energy of $\approx 2 \text{ mJ}/1.4 \text{ mJ}$ at a repetition rate of $f_{\text{rep}} = 3 \text{ kHz}/5 \text{ kHz}$. Further details about the system can be found, *e.g.*, in [Weier15]. The general setup for time-resolved measurements is based on a pump-probe scheme [Bauer05], where the original beam is split into two parts. One of them, the so-called "pump" beam, drives the system into an excited state from which it can then relax back. The second beam ("probe") measures the state of the system after a certain time delay. By repeating this procedure with varying

¹Note that parts of this chapter are also subject of [Plötzing16].

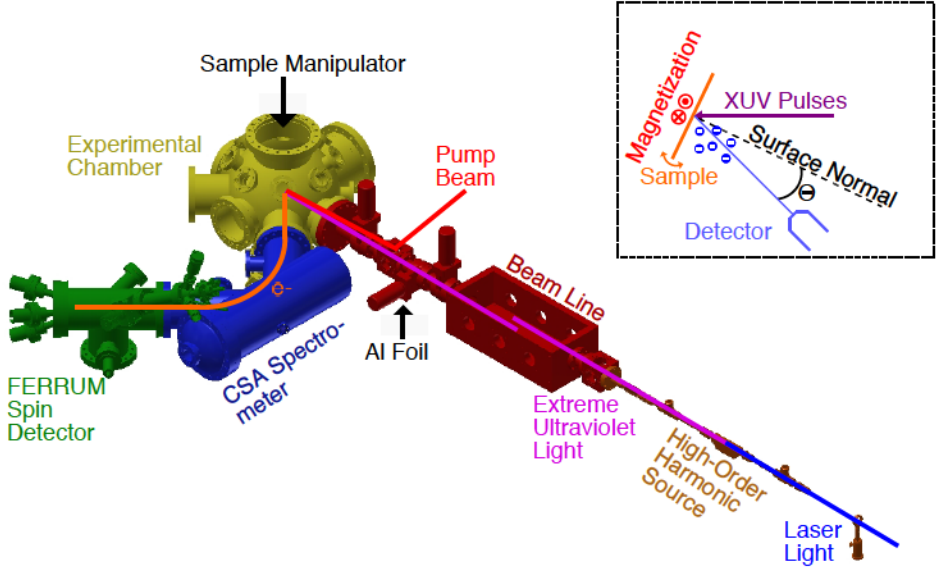


Figure 3.1: Setup for time- and spin-resolved photoelectron spectroscopy. The extreme ultraviolet light is generated in the high-order harmonic generation source (bottom right) and can be monochromatized, focussed and aligned in the evacuated beamline. Afterwards, it illuminates the sample in the experimental chamber leading to the emission of photoelectrons, which are then analyzed using the spectrometer and the spin detector (left side). (Adapted from [Plötzting16] with permission of AIP Publishing. The CC license does not apply.)

delay between the pump- and probe-pulses, the time evolution of the relaxation of a reversible process can be traced. In our system, the first part of the laser beam is used with its original photon energy as a pump to deposit energy into the system, and the second part is frequency-upconverted and then triggers the photoemission process for probing the transient state.

As already mentioned, a HHG source is used for the frequency-upconversion in our setup. It can be used in two different "driving" modes each requiring different elements in the beam path. In the first one, referred to as red-driven mode (RDM) in the following, the fundamental laser wavelength of 780 nm is directly used for the HHG process, whereas in the blue-driven mode (BDM) the light is first frequency-doubled in a 200 μm -thick $\beta\text{-BaB}_2\text{O}_4$ (BBO) crystal (Type 1, cutting angle $\theta_{\text{cut}} \approx 29.2^\circ$). In our experiments employing the BDM, the efficiency of the second harmonic generation (SHG) was above 30%. After the SHG, the remaining 780 nm light is separated by a dichroic beam splitter and used as the pump beam. In the RDM, usually around 10% of the laser light is split-off for the excitation before the light enters the HHG source. The part of the laser light that is intended

3.1. MONOCHROMATIC FEMTOSECOND-PULSED EXTREME ULTRAVIOLET LIGHT SOURCE

to drive the HHG process is in both cases focused by a lens into a glass-capillary with an inner diameter of $150\text{ }\mu\text{m}$ serving as a waveguide. Since for valence band photoemission an efficient energy conversion is more important than maximizing the cut-off energy (see Eq. 2.33), we use Ar gas in the BDM as well as in the RDM as the conversion medium [Falcão-Filho10]. In order to optimize the conversion efficiency and the spectral distribution of the XUV light, the phase-matching conditions (see Sec. 2.3.2) can be varied mainly by moving and tilting the capillary, shifting the focal point of the laser beam and changing the gas pressure. In general, the best results were obtained for gas pressures in the range of $p = 10 - 50\text{ mbar}$ in our setup. After its creation, the XUV light was kept in a low-pressure environment ($p < 1 \cdot 10^{-3}\text{ mbar}$) to avoid reabsorption. The beam path of the light is, however, different for both modes after leaving the HHG source, because the light spectra differ as already discussed in Sec. 2.3.3.

Using the 780 nm driving light, a broad comb of harmonic intensity peaks reaching up to $\approx 45\text{ eV}$ [Mathias07, Falcão-Filho10] is created. In order to use it for photoemission, one of the harmonics has to be isolated using a monochromator. This is achieved by constructive Bragg reflection at a pair of Si/Mo multilayer mirrors, which are specifically designed to select the harmonic peak centered at $h\nu_{RDM} = 42.7\text{ eV}$. The mirrors are arranged in a z-shape geometry with an incidence angle of 5° with respect to the surface normal (see top left side of Fig. 3.2) in order to obtain the desired energy selection. A curvature of the second mirror focuses the beam onto the sample. In this geometry, only around 4% of the light of the selected harmonic is transmitted. After passing the Bragg mirrors, remaining fundamental laser light is blocked by a 200 nm -thick, freestanding aluminum foil which transmits 65% of the XUV radiation (see right side of Fig. 3.2).

This Al foil is also used in the BDM. Here, the cut-off energy of the harmonics spectrum can be tuned by changing the phase-matching conditions in such a way that only one harmonic peak exceeds the low-energy cut-off of the Al [Eich14]. Thus, already one harmonic is singled out with, in our case, a photon energy of $h\nu_{BDM} = 22.5\text{ eV}$. Since no further monochromatization is necessary, the XUV light is only reflected from a SiO_2 wafer to suppress the fundamental laser light and a toroidal Au mirror in order to achieve focusing. Both reflections are carried out in grazing incidence (85° towards the surface normal, see bottom left side in Fig. 3.2) resulting in a total transmission higher than 70% (calculated with the software "REFLEC" from the BESSY II software library [Schäfers96]).

Typical light spectra arriving at the photoemission chamber are shown in Fig. 3.3 for the RDM as well as the BDM case. They show the first diffraction order measured with a self-constructed optical grating spectrometer using a $2\text{ }\mu\text{m}$ -period and a highly sensitivity charge-coupled device (CCD)². The spectrometer was also employed to monitor the XUV output during HHG optimization. The energy

²The spectrometer is similar to [La-O-Vorakiat09, Rudolf12], but using a non-magnetic grating.

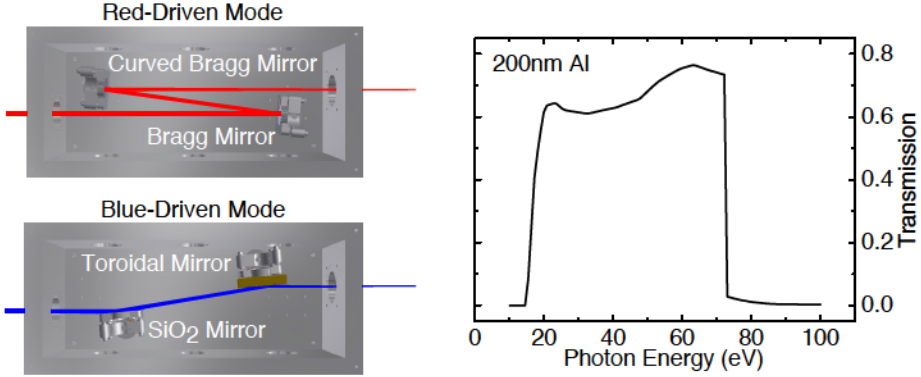


Figure 3.2: Left: Beam path in the monochromator chamber in the "red-driven mode" (top) and "blue-driven mode" (bottom). If the fundamental 780 nm light of the laser is used for the HHG process, one harmonic is selected from the XUV radiation by Bragg reflections. For already frequency-doubled light, no further monochromator is necessary resulting in a higher transmission. (Adapted from [Plötzing16] with permission of AIP Publishing. The CC license does not apply.) Right: Transmission of a thin Al foil for different photon energies. The cut-off at 17 eV causes a blocking of the fundamental laser light as well as harmonics with lower order. (data taken from [Henke93])

of the dominating harmonic peak in the spectra is determined by comparing the Fermi level cut-off of photoemission spectra measured with the HHG source and with a well-characterized He gas-discharge lamp (see the end of this section). A further calibration of the energy scale is then realized by using the knowledge about the separation of the neighboring harmonics (see Eq. 2.32). The central photon energies are 22.5 eV and 42.7 eV for the transmitted light in the BDM and the RDM, respectively, and the full width at half maximum (FWHM) of the main intensity peaks is below 500 meV in both cases. However, this value is only an upper limit and is influenced by the wavelength resolution of the grating spectrometer. A more precise determination is performed using the photoemission results (see Chap. 5). Moreover, Fig. 3.3 shows that neighboring peaks are suppressed by more than a factor of 10. The light provided by the HHG source has the same polarization as the fundamental laser beam. If not stated otherwise, the polarization is horizontal in the RDM and vertical in the BDM within the presented work. The XUV light generated by the HHG source propagates towards the sample in the horizontal plane with an angle of 45° with respect to the direction where the photoelectrons are detected. The photon energies can be translated into electron wave vectors perpendicular to the sample surface within a free-electron final state framework (see Sec. 2.3) according to Eq. 2.13 and Eq. 2.23. For the valence band electrons of Co measured in normal emission ($E_b = 1$ eV, $\Theta = 0$, $V_0 = 15$ eV from

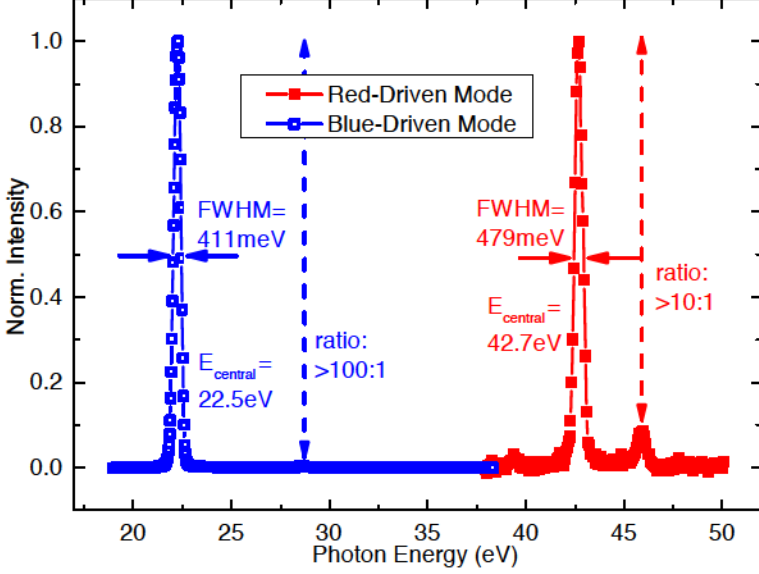


Figure 3.3: Photon energy distribution of the XUV radiation after monochromatization measured with a grating monochromator. The transmitted intensity peak in the BDM is located at a photon energy of $h\nu_{BDM} = 22.5$ eV and the selected harmonic in the RDM at $h\nu_{RDM} = 42.7$ eV. (Adapted from [Plötzing16] with permission of AIP Publishing. The CC license does not apply.)

[Miyamoto08a] and $\phi = 4.8$ eV from [Wallauer96]), this yields $k_{\perp} = 3.7 \text{ \AA}^{-1}$ in RDM and $k_{\perp} = 2.9 \text{ \AA}^{-1}$ in BDM. Assuming a lattice parameter in z-direction of 3.46 \AA for face-centered tetragonal (fct) Co [Heckmann94] and thus a distance between Γ and X of 1.82 \AA^{-1} , this is located close to Γ and in the middle of the Brillouin zone (BZ), respectively.

For time-resolved measurements, the pump-beam is passing a retroreflecting mirror pair, which can be moved in order to adjust the length of the beam path ("delay stage"). Thus, the arrival time of the pump-pulses and therefore the delay between excitation and probing of the process can be varied. The orientation of the linear polarization and the intensity is adjustable using a half-wave plate and a thin film polarizer. Then, the pump-beam is coupled into the vacuum system after the Al foil through a borosilicate glass window and guided almost co-linearly with the XUV radiation to the sample.

Comparing the advantages of both sources, the broad range of harmonics that is provided in the RDM makes it, in principle, possible to map the BZ in k_{\perp} -direction as described in Sec. 2.2.1 by using a grating monochromator or Bragg mirrors

designed for different photon energies. For this usually large-scale synchrotron facilities are necessary [Schneider12]. The energy range covered by a HHG source using a fundamental wavelength of 780 nm and Ar as the conversion medium can be translated as described above to values of 2.7 \AA^{-1} for 19 eV and 3.7 \AA^{-1} for 43 eV at the edges of a typical spectrum. This covers more than half of the $\Gamma - X$ direction. Using even higher photon energies that are available employing a different noble gas like Ne, which creates a harmonic comb exceeding the high-energy cut-off by the Al foil, this range can be expanded (4.6 \AA^{-1} for 70 eV). In this case, also the lowest energy core levels of the ferromagnets Fe, Co and Ni, the $3p_{1/2}$ and $3p_{3/2}$ states which are located around $E_{Fe} = 53 \text{ eV}$, $E_{Co} = 59 \text{ eV}$ and $E_{Ni} = 67 \text{ eV}$ [Williams01], can be reached and addressed in resonant photoemission experiments [Guillot77]. On the other hand, the BDM offers a significantly higher efficiency in the conversion process (see Sec. 2.3.3) leading to a brighter photon flux. This effect is enhanced even more by the higher transmission in the beamline since all optical elements can be used in grazing incidence and therefore have a better reflectivity. Altogether, the XUV photon flux at the sample is approximately two orders of magnitude larger in BDM than in RDM.

Besides the HHG source, the experimental setup is equipped with a continuous wave (cw) He-discharge lamp (UVS300, SPECS Surface Nano Analysis GmbH), which can produce spectrally sharp ($\Delta h\nu_{He} < 1 \text{ meV}$) light at the He-I ($h\nu_{He-I} = 21.2 \text{ eV}$) and the He-II ($h\nu_{He-II} = 40.8 \text{ eV}$) emission lines. The relative intensity of the two photon energies can be tuned by, *e.g.*, varying the gas pressure. Light provided from the gas-discharge source illuminates the sample under an angle of 45° with respect to the photoelectron detection direction within a vertical plane of incidence and is unpolarized. Using the same values as for the HHG source, the resulting perpendicular wave vectors that are addressed according to the free-electron final state model are $k_{\perp} = 2.8 \text{ \AA}^{-1}$ for the He-I and $k_{\perp} = 3.6 \text{ \AA}^{-1}$ for the He-II line.

3.2 Experimental Chamber & Photoelectron Detection

The light from the sources described above then impinges on the sample, which is located in the main experimental chamber during the measurements (yellow in Fig. 3.1). Due to the limited information depth (see Sec. 2.2.1), already a single monolayer of an adsorbate on the sample surface strongly influences the results of PES measurements. Assuming that an exposure to approximately $3.5 \cdot 10^{-6} \text{ mbar} \cdot \text{s}$ is sufficient to cover the sample surface with one monolayer [Hüfner95], a base pressure in the low 10^{-10} mbar range has to be established in the experimental cham-

ber to ensure comparable sample properties over several hours. This pressure is achieved by a combination of turbomolecular and ion pumps. The separation of the UHV in the photoemission chamber from the moderate vacuum in the HHG source ($p_{HHG} = 10 - 50$ mbar) is realized by a differential pumping scheme and the use of a pinhole-free Al foil for the blocking of the fundamental laser light (see Sec. 3.1).

3.2.1 Spectrometer

As shown in Fig. 3.1 (blue) and Fig. 3.4, the photoelectrons emitted from the sample are collected and filtered by their kinetic energy using a horizontally mounted cylindrical sector analyzer (CSA 300, Focus GmbH) after their emission from the sample. This spectrometer is based on deflection in an electric field and allows only electrons with a particular kinetic energy E_{kin}^{sel} to pass. Using such an energy-filter, the electrons are monochromatized and then the number is counted. Subsequent measurements that analyze a specific kinetic energy E_{kin}^{sel} are necessary in order to gain a complete spectrum. To obtain a wave vector-dependent picture, this procedure is repeated for all desired photoelectron emission angles by rotating the sample.

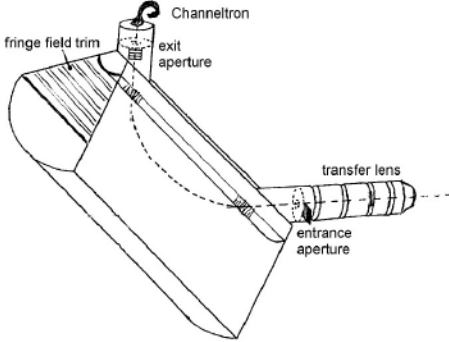


Figure 3.4: Schematic drawing of the cylindrical sector analyzer. The photoelectrons enter through the transfer lens and are deflected and energy-filtered within the cylinder sectors. In our setup, the channeltron behind the exit aperture is replaced by a spin detector. (Reprinted with permission from [Foc09]. The CC license does not apply.)

If no bias voltage is applied to the sample, the photoelectrons reach the energy-filter through field-free space. After entering the CSA, the electrons are accelerated by a voltage of $U_{acc} = 300 \text{ V} - E_{kin}^{sel}$ applied between two subsequent grids. Consequently, the kinetic energy of the electrons that are meant to pass is always increased to 300 eV and the adjustable voltage between these grids determines which kinetic energy will be selected. Then, the photoelectrons propagate through a lens system that images them onto a slit defining the transversal spread of the electron bunch in the direction of deflection ("entrance slit"). Simultaneously, the kinetic energy of the desired photoelectrons (originally propagating with E_{kin}^{sel}) is reduced to the "pass energy" E_{pass} that is constant during the acquisition of a spectrum. However, its value can be adjusted before the measurement in order to adjust the energy resolution (see following paragraph). Afterwards, the electrons enter the deflection

region between two electrodes, which are shaped like sectors of concentric cylinders with different radii (see Fig. 3.4). Here, an electric field is applied that bends the trajectory of the electrons with E_{pass} by an angle of 90° , whereas electrons with a different kinetic energy are deflected stronger or weaker. Using a second slit ("exit slit") at the end of the interaction region, which is also oriented perpendicular to the deflection plane, the electrons with E_{pass} are selected from the dispersed beam. The design of the spectrometer, which accelerates the electrons with E_{kin}^{sel} always to a constant pass energy, ensures that their trajectories stay the same during a scan of different E_{kin}^{sel} . Consequently, the imaging properties as well as the transmission of the lens system and the energy resolution in the deflection part are maintained. According to [Foc09, Risley72], the base energy resolution³ of the CSA is given by⁴

$$\frac{\Delta E_{CSA,base}}{E_{pass}} = \frac{w_1 + w_2}{D} + 2.7 \cdot (\Delta\theta)^3 + \left(\frac{r_c}{R_i}\right)^2. \quad (3.1)$$

In Eq. 3.1, the three summands represent the main factors influencing the energy resolution. The first term takes into account the finite width of the two slits at the entrance and the exit of the deflection region. Here, the parameter D describes the dispersion properties of the spectrometer and is mainly given by the size of the spatial spread induced by the electric field for an electron beam with a given kinetic energy distribution. The width of the entrance slit w_1 allows electrons with an offset from the beam axis in the deflection direction to enter the electric field, which then can be dispersed to the same point as on-axis electrons with E_{kin}^{sel} even if they have a different kinetic energy. Moreover, electrons entering at the same position but with slightly different kinetic energies are able to pass due to the width of the exit slit w_2 . The contribution treated within this summand can be adjusted by changing the size of the slits (w_1/w_2), but a reduction also decreases the electron transmission. In the second term, the influence of the angular distribution of the photoelectrons entering the deflection area is described. This induces a contribution to the spectrometer energy resolution, because electrons with different kinetic energies can again end up at the same position after passing the electric field. Therefore, the corresponding term depends on the acceptance angle of the CSA $\Delta\theta$ (given in rad). It can be reduced by decreasing the accepted emission angles, which again leads to a lower electron count rate. The third term accounts for the spread of the electron beam perpendicular to the deflection plane. These electrons additionally feel an acceleration towards

³Regarding the broadening of an initially sharp feature into a spread peak in the spectrum, the base energy resolution is determined from the width of the peak at its basis. It can usually be approximated by twice the FWHM [Risley72, Rubio-Zuazo11] of this peak.

⁴Rubio-Zuazo *et al.* [Rubio-Zuazo11] in general confirm the shape of Eq. 3.1 and quantify the effects by more precise numerical simulations. This in particular leads to a slight redefinition of the third term. In addition, they promote a different prefactor for the second term, which however can not be explained by the small deviations in the underlying parameters and the difference is also not obvious from their remarks.

this plane leading to a trajectory that ends on its opposite side. Thus, their path is tilted towards the normal deflection trajectory, which defines the entrance and exit slit position, and the projection is not representing the full kinetic energy of the particles. The influence of this term can be (phenomenologically) described using the ratio of the radius of the inner cylinder R_i and the distance of closest approach of the electrons to the analyzer symmetry axis r_c . Values for the single terms can be found in [Foc09] for the spectrometer that is used in this thesis.

The absolute energy resolution ΔE is in addition affected by the pass energy since E_{pass} defines how long the electrons stay within the deflecting electric field and thus how strong electrons with different kinetic energies are separated when they arrive at the second slit. Again, a better energy resolution (meaning lower E_{pass}) is leading to a decrease in the count rate, because a smaller energy window with less electrons is selected by the exit slit. The pass energy can be selected between values of 1 eV to 32 eV in the ultraviolet photoelectron spectroscopy (UPS) mode of the CSA.

3.2.2 Spin Detector

After the selected photoelectrons passed through the spectrometer, they are guided into the spin polarimeter⁵ (FERRUM, Focus GmbH). As shown on the left side of Fig. 3.5, the electron beam can be either deflected into channeltron 1, which measures the spin-integrated intensity, or focused to the scattering target by an electrostatic entrance lens.

The detector creates the spin imbalance via exchange scattering at an Fe(001)-p(1x1)O surface (see Sec. 2.2.3). This surface is created by depositing a thin Fe film on a W(001) crystal and afterwards passivating it by oxygen dosing [Bertacco99a]. It has a magnetic anisotropy leading to in-plane remanence [Winkelmann08] and can be magnetized along and contrary to the two perpendicular magnetic easy axes [100] and [010] by magnetic field pulses as illustrated on the right side of Fig. 3.5. This defines then the spin quantization direction. The scattering potential for spin-resolved measurements is adjusted to 6.4 eV using electrostatic lenses, where the figure of merit (FoM) (see Eq. 2.27) of the detector has an experimentally determined maximum value of $\text{FoM} = 4.4 \cdot 10^{-3}$ for the measurement of one spin direction (see bottom of Fig. 3.6). In general, in a ferromagnetic scattering target both the spin-orbit coupling (SOC) and the exchange interaction give a contribution to the spin asymmetry (Sherman) function. With the help of asymmetry measurements of a ferromagnet magnetized in two opposite directions, these contributions can be disentangled [Escher11]. The center part of Fig. 3.6 shows the resulting values, which are converted to the situation of an incoming electron beam with 100% spin polarization. Here, the Sherman function resulting from the exchange interaction is $A_{ex} = S_{eff} = 0.29$ at the selected scattering potential of 6.4 eV. Furthermore, the

⁵The polarimeter is described in more detail in [Escher11].

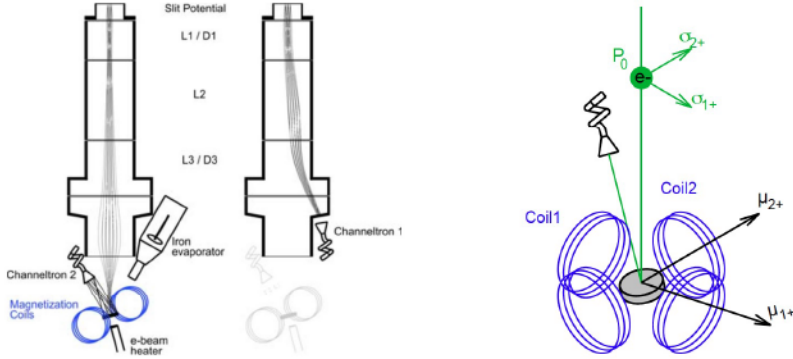


Figure 3.5: Left: Operation Modes of FERRUM. The left side shows the spin-resolved mode, where the electrons are scattered at the Fe target. In the spin-integrated case (right side), all electrons are deflected into channeltron 2 immediately after entering the polarimeter. (Reprinted from [Escher11], licensed under [CC-BY].) **Right: Scattering geometry of FERRUM.** The Fe target can be magnetized in two perpendicular directions μ_1/μ_2 by coil 1 and coil 2. In each case, the spin detector is mainly sensitive to the corresponding spin direction σ_1/σ_2 . (Reprinted from [Escher11], licensed under [CC-BY].)

measurement reveals that the influence of the SOC (A_{so}) is negligible at this energy. After the scattering at the target, channeltron 2 collects the electrons that are specularly reflected under an angle of 15° from the Fe film. The reflectivity is $\approx 10\%$ for the adjusted scattering potential. In order to protect the low-energy electrons from the influence of external magnetic fields, the detector is surrounded by a mu-metal shield. Due to the oxygen passivation, the scattering crystal can be used for several weeks under UHV conditions without a degradation of its performance before a new preparation of the surface is necessary.

In spin-resolved measurements, the electron intensity is counted for a parallel (\tilde{I}_+) and an anti-parallel (\tilde{I}_-) alignment of the Fe magnetization with respect to the spin component of interest. Due to the horizontal 90° deflection of the CSA, the spin detector can access the vertical in-plane or the out-of-plane magnetization direction of the sample in our setup. In order to compensate for linear drifts, the sequence ($\tilde{I}_+, \tilde{I}_-, \tilde{I}_-, \tilde{I}_+$) is repeated for every measurement cycle [Winkelmann08]. From the summed up intensities for both Fe magnetization directions I_\pm , the asymmetry A and the spin polarization P can be calculated according to Eq. 2.25 and Eq. 2.26. Using the spin polarization, the so-called "partial intensities"

$$N_\pm = \frac{1}{2}(I_+ + I_-) \cdot (1 \pm P) \quad (3.2)$$

can be determined. They represent the real ratio between spin-up and spin-down electrons taking into account the influence of the detector asymmetry function S_{eff} .

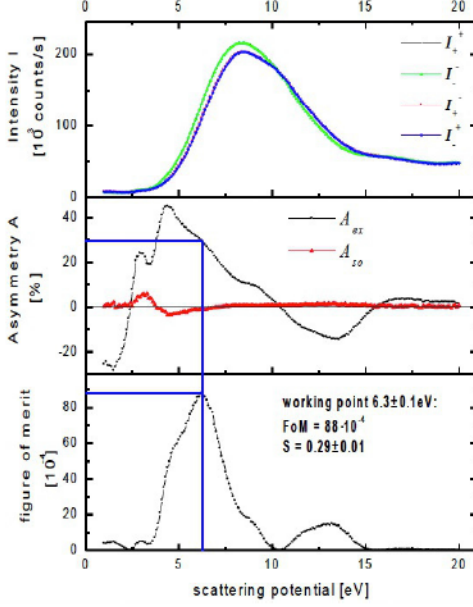


Figure 3.6: Reflectivity of the scattering target and the corresponding asymmetry and FoM as a function of the scattering potential. In the measured intensities I_{μ}^{σ} , the μ indicates the magnetization direction of the target and the σ the dominant spin direction in the electron beam. Curves for measurements with differing μ as well as σ are overlapping. The asymmetry, normalized to a fully polarized beam, is split into the contribution from SOC A_{so} and exchange interaction A_{ex} (see text). (Reprinted from [Escher11], licensed under [CC-BY].)

The error bars of all values are determined by the law of error propagation from the error on the sum intensities $\sigma_{I\pm}$. Here, the $\sigma_{I\pm}$ are calculated as the sum of $\sqrt{I_{\pm}}$ and the standard deviation from several measurement cycles. Consequently, the Poisson characteristics of the measurement (first term) as well as additional fluctuations of the light intensity (second term) are considered. The latter are in particular relevant for measurements with the laser-based HHG source.

3.2.3 Sample Preparation Equipment

Due to the high requirements of surface quality, the samples have to be prepared *in situ*. For this purpose, sample preparation and characterization equipment has been installed inside the UHV environment. In addition, a load lock and a sample storage have been mounted. For the sample preparation, a resistive heater reaching up to 950°C, an ion sputtering source, and electron beam evaporators are available. In order to inspect the grown films, an electron gun allows for both low-energy electron diffraction (LEED) to check the crystalline quality and Auger electron spectroscopy (AES) to verify the chemical purity (ErLEED150, SPECS Surface Nano Analysis GmbH).

4 Sample Preparation and Characterization: Co/Cu(001)

In the following, the sample preparation and photoelectron detection capabilities of the setup introduced in Chap. 3 are tested. For this purpose, the sample system studied in this work, namely Co layers on Cu(001), is introduced and its preparation procedure is described (Sec. 4.1). In the second part of the chapter, the samples are characterized employing the devices for spin-resolved photoelectron spectroscopy.

4.1 Sample Preparation Procedure

Thin Co films deposited on a Cu(001) crystal provide a very good model sample system for the investigation of spin dynamics in the electronic band structure of a 3d ferromagnet. The Co grows in a pseudomorphic, metastable face-centered tetragonal (fct) structure following the fcc structure of the Cu(001). Here, the in-plane lattice parameter of the Cu is conserved ($a_{\parallel} = 3.61 \text{ \AA}$) and also kept within additional Co layers. Perpendicular to the surface, the lattice parameter is $a_{\perp} = 3.46 \text{ \AA}$ [Clarke87, Kief93, Heckmann94]. Almost perfect epitaxial layer-by-layer growth is observed [Schmid92, Li90, Schneider90b] when the Co is deposited at substrate temperatures below 490 K. For higher growth or post-deposition annealing temperatures, interdiffusion processes lead to intermixing of the Cu and Co atoms [De Miguel91, Allmers11]. Studies of the magnetic properties reveal that a ferromagnetic order at room temperature (RT) is achieved above two monolayers of Co with a magnetic easy axis along the $[110]$ and $[1\bar{1}0]$ in-plane direction. A spin-reorientation for increasing film thickness d has not been observed [De Miguel91, Krams92]. With rising d , the Curie temperature of the Co films increases reaching already more than 500 K for 3 ML [Schneider90b].

In order to prepare an appropriate Cu surface, we cleaned the crystal by Ar-ion bombardment for 30 min with a particle kinetic energy of 1 kV. Furthermore, the crystal was annealed for 10 min above 850 K to reduce its surface roughness. After cooling down close to RT again, the magnetic film was evaporated from a

high purity Co rod.

The deposition rate was calibrated by the information depth of photoemission using the intensity of the remaining signal from the 3d bands of the Cu crystal underneath the deposited Co. As an example, the left side of Fig. 4.1 shows energy distribution curves (EDCs) measured for different Co evaporation times. The gray box marks the energy range of the characteristic Cu 3d bands. While the thickness of the Co layer increases, less electrons from the Cu reach the surface and the corresponding photoemission intensity in normal emission I_{Cu} decays. This intensity can be described by [Hofmann12]

$$I_{Cu} = I_{Cu,0} \cdot \exp\left(-\frac{d}{\lambda_{EAL,Cu,14\text{eV}}}\right) + I_{BG}, \quad (4.1)$$

with the effective attenuation length (EAL) λ_{EAL} (see Sec. 2.2.1), the height of the signal from Cu without a Co overlayer $I_{Cu,0}$, and the background intensity I_{BG} . Assuming a linear film growth with time, the evaporation duration τ_{evap} , which is necessary to create a Co layer with a thickness corresponding to the EAL, can thus be determined from the results on the left side of Fig. 4.1. It is done by extracting the height of the Cu peak and fitting an exponential function to the decaying intensity with increasing deposition time as presented on the right side of Fig. 4.1. The fit yields $\tau_{Co,14\text{eV}}^{evap} = 5.10 \pm 0.07$ min.

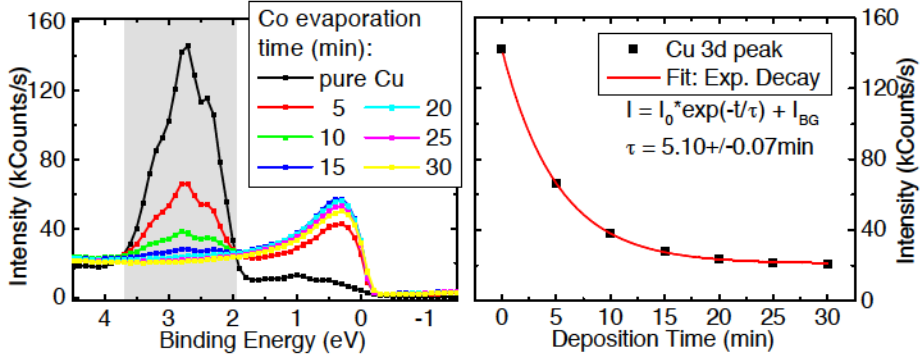


Figure 4.1: Left: Photoemission spectra of Cu(001) with a Co overlayer after different deposition times. The data was measured in normal emission using the He-discharge lamp at a photon energy of $h\nu = 21.2\text{eV}$. For the increasing film thickness, additional Co was evaporated on top of the existing sample. The binding energy is calculated with respect to the Fermi level ($E_B = 0$). Right: Peak intensity of the characteristic Cu features as a function of the Co deposition time. The data is extracted from the spectra shown on the left side and the red line represents a fit of the exponential function presented in the inset.

In order to calculate the deposition rate, a reference measurement of the EAL with

4.2. CHARACTERIZATION USING PHOTOELECTRON SPECTROSCOPY

a similar photon energy is needed. In Fig. 4.2, the value

$$\lambda_{EAL,Co,17\text{eV}}^{ref} = 5.02 \pm 1.31 \text{ ML} \quad (4.2)$$

is extracted for the EAL by fitting the exponential decay function shown in Eq. 4.1 to data taken from [Schneider90a].

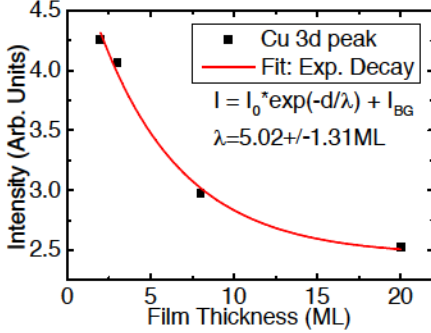


Figure 4.2: Damping of the Cu photoemission intensity in a Co overlayer as a function of the overlayer thickness. The underlying measurements were performed in normal emission using synchrotron radiation with a photon energy of $h\nu = 24 \text{ eV}$. (data extracted from [Schneider90a])

Since the kinetic energies are high enough to neglect non-parabolic band effects of the Co (see Sec. 2.2.1), the variations in the EAL within small changes of the kinetic energy are negligible. Consequently, $\lambda_{EAL,Co,14\text{eV}}^{meas} \approx \lambda_{EAL,Co,17\text{eV}}^{ref}$ can be assumed and the deposition rate is

$$r = \frac{\lambda_{EAL,Co,17\text{eV}}^{ref}}{\tau_{Co,14\text{eV}}^{evap}} = 0.98 \pm 0.26 \frac{\text{ML}}{\text{min}} \quad (4.3)$$

for the shown example. All deposition rates and film thicknesses in the presented work are determined in the described way using $\lambda_{EAL,Co,17\text{eV}}^{ref}$ from Eq. 4.2. In general, an analog analysis is possible with the corresponding Co peak ($E_{kin} = 16.5 \text{ eV}$), which has an increasing spectral weight for thicker overlayers. However, its height is influenced by the nearby Fermi level and thus the analysis is less accurate. The individual film thicknesses for the samples under investigation are given in the corresponding sections. For all measurements presented in this thesis, the thickness is well above $3\lambda_{EAL,Co}$ (see Eq. 4.2) in order to suppress photoemission contributions from the Cu substrate. After preparation, the Co films were magnetized along the vertical [110] (in-plane) direction if not otherwise stated.

4.2 Characterization Using Photoelectron Spectroscopy

In order to test the sample preparation procedure and characterize the capabilities of the photoelectron analysis devices in our setup, we performed photoemission

measurements using the He gas-discharge lamp¹. First, we analyzed the orientation of the magnetization of the Co films. In Fig. 4.3, the spin polarization measured over the full energy range accessible by the He-I line is shown for both spin directions that can be addressed by the detector.

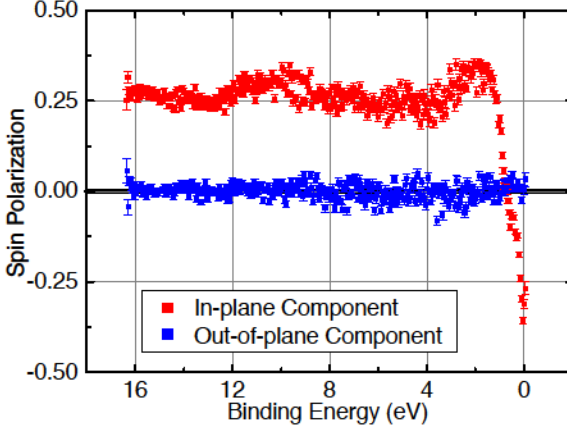


Figure 4.3: In-plane and out-of-plane component of the spin polarization in fct Co plotted against the electron binding energy. The photon energy is $h\nu = 21.2\text{ eV}$, the photoelectron emission angle $\Theta = 0^\circ$ and the thickness of the Co film $d = 40 \pm 12\text{ ML}$. The Fermi level is located at $E_B = 0$. The error bars, determined as described in Sec. 3.2, underestimate the real errors because of additional noise in the electron count rate caused by insufficient shielding of the cables, which were used for this measurement.

It shows a clear non-zero value for the direction corresponding to the (vertical) in-plane component of the sample, whereas no spin polarization is present within the uncertainty of the data for the out-of-plane component. Consequently, the Co films are, as expected, in remanence fully in-plane magnetized. In addition, the measurement proves that the detector is able to separate both spin polarization components.

In order to further characterize the setup as well as the samples, the in-plane component of the spin polarization was studied by angle-resolved photoemission. For this purpose, measurements were performed at a range of chosen angles by rotating the sample in steps of $\Delta\Theta = 2.5^\circ$ around the vertical axis ([110]). This leads to a variation of the detected wave vectors within the plane spanned by Γ , K and L in the bulk Brillouin zone (BZ) (see left side of Fig. 2.3 and [Miyamoto08a]). The results are shown in Fig. 4.4. For normal emission ($k_{\parallel} = 0$), the photoemission spectra close to the Fermi level ($E_B = 0$) are dominated by a minority electron band that bends towards higher binding energies for increasing wave vectors (Fig. 4.4, left). By a comparison with theoretical band structure calculations, it can be assigned to a $\Delta_{5\downarrow}$ symmetry [Clemens92, Schneider91a]. Therefore, transitions are allowed using light with a polarization parallel to the sample surface according to the dipole selection rules (see step 1 in Sec. 2.2.1), which is given for the high-order harmonic

¹Note that parts of this section are also subject of [Plötzing16].

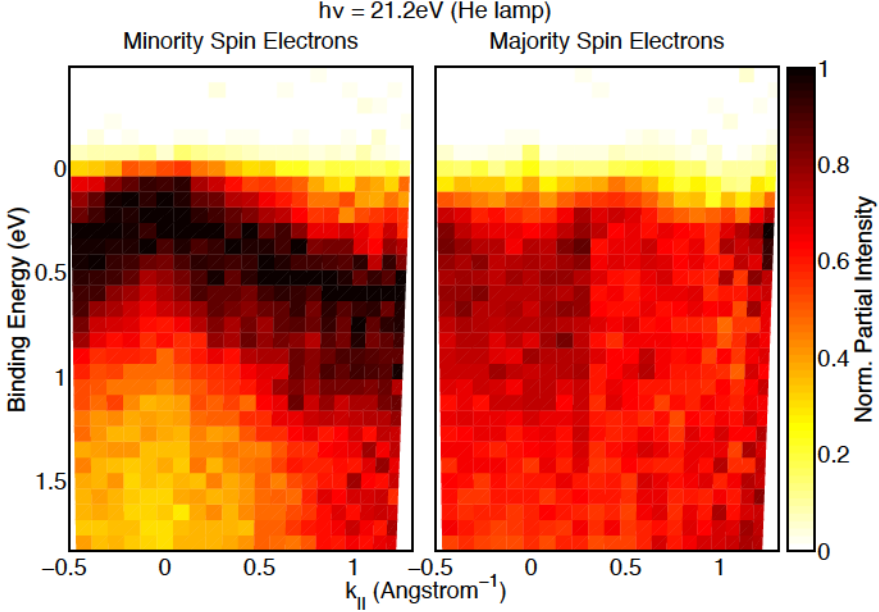


Figure 4.4: Partial intensities of fct Co as a function of the in-plane wave vector and the electron binding energy for minority (left) and majority spin electrons (right). The measurements were performed employing the He-I line ($h\nu = 21.2$ eV) and the electron wave vector k_{\parallel} was calculated using Eq. 2.22 from the photoelectron emission angle. The partial intensities for each angle are normalized to the maximum of the minority spin component and the Co film was $d = 30 \pm 8$ ML thick. $E_B = 0$ corresponds to the Fermi level.

generation (HHG) source as well as the He lamp in our setup².

For the majority spin direction (Fig. 4.4, right), the measurement results are significantly smeared due to electron correlations (see Sec. 2.2.1) [Grechnev07, Ellguth15]. In general, electron correlation effects almost completely quench valence band features for $E_B > 2$ eV in the majority spin channel [Monastra02]. Thus, only a broad peak can be observed ($E_B = 0.9$ eV at $k_{\parallel} = 0$), which is approaching E_F for higher k_{\parallel} . In band structure calculations [Schneider91a], only a band having $\Delta_{2\uparrow}$ symmetry is present at the corresponding energies. Even though an optical transition from a pure $\Delta_{2\uparrow}$ band is forbidden by the non-relativistic dipole selection rules, the effect of spin-orbit coupling (SOC) and resulting band hybridization with a nearby $\Delta_{5\uparrow}$ band (see right side of Fig. 2.3 [Chiang10]) can lead to a significant contribution in photoemission spectra [Kuch95]. The observed spectral densities in the valence

²Note that the presented dipole selection rules and the reduction of the final state to Δ_1 -symmetry are only strictly valid for $k_{\parallel} = 0$.

band region are in good agreement with published results for similar experimental conditions [Miyamoto08a]. Due to the dispersion of the minority spin band away from E_F and of the majority spin band towards E_F for increasing k_{\parallel} , both contributions are most separated at normal emission. Thus, all upcoming measurements are performed for $k_{\parallel} = 0$.

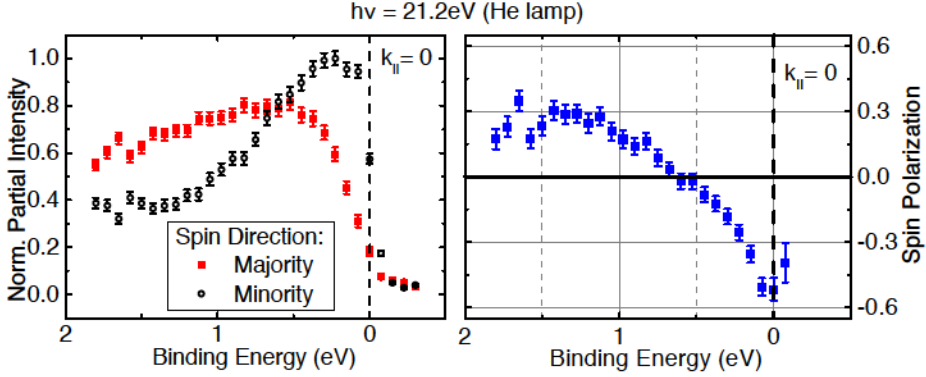


Figure 4.5: EDCs of the partial intensities for both spin directions recorded on fct Co(001) and the corresponding spin polarization distribution. The data is taken from the measurement shown in Fig. 4.4 for $k_{\parallel} = 0$.

The EDCs of the partial intensities at $\Theta = 0^\circ$ are shown in Fig. 4.5 (left). At the high binding energy flank ($E_B = 0.7$ eV) of the peak belonging to the already identified $\Delta_{5\downarrow}$ minority spin band ($E_B = 0.2$ eV), an additional shoulder is visible³. It can be attributed to a surface resonance that strongly disperses to lower binding energies for increasing k_{\parallel} [Miyamoto08b]. This resonance was found to have even symmetry and is thus only accessible with p-polarized light according to the dipole selection rules. The spin polarization in this measurement (see Fig. 4.5, right), shows a positive value of $P \approx 0.3$ eV in the energy range that is dominated by the majority spin electrons ($E_B > 1$ eV). For smaller binding energies, the value is reduced and reverses sign ($E_B = 0.5$ eV) due the rising influence of the minority spin electrons. The shape of this change of sign shows a step, which is induced by the double-peak character of the minority spin electron spectrum. Close to E_F , the $\Delta_{5\downarrow}$ band and the lack of majority spin electrons leads to a high negative spin polarization.

³The underlying peak is already partly suppressed due to slight contaminations of the sample surface, *e.g.* resulting from residual gas in the vacuum chamber. The possibility to conduct an Auger electron spectroscopy (AES) measurement or a residual gas analysis with a mass spectrometer was not available at the time when this photoemission study was performed. However, we expect contaminations from H_2 , CH_4 , CO or CO_2 molecules, which are in general mainly present in a baked vacuum chamber [Fremerey99].

5 Spin-Resolved Photoemission with Femtosecond Extreme Ultraviolet Light Pulses

After proving the functionality of the photoelectron detection devices as well as a good quality of the *in situ* prepared thin Co(001) films in the previous chapter, the influence of an excitation with femtosecond pulses on the photoemission results is studied in the following¹. For this purpose, spin-resolved measurements were performed using the high-order harmonic generation (HHG) source (red-driven mode (RDM) in Sec. 5.1, blue-driven mode (BDM) in Sec. 5.2) and compared to data that was acquired with the continuous wave (cw) gas-discharge lamp under similar conditions. A key challenge in photoemission with light pulses are vacuum space-charge (VSC) effects due to the Coulomb repulsion in the dense photoelectron clouds, which are created at the sample surface. In the last part of this chapter, the resulting spectral distortions are addressed and quantified for our setup.

5.1 Red-Driven Mode

As already stated in Sec. 3.1, the HHG source in RDM provides photons with an energy of $h\nu_{RDM} = 42.7\text{ eV}$, which is close to the He-II line of the gas-discharge lamp ($h\nu_{He-II} = 40.8\text{ eV}$). Therefore, the spectra measured with both light sources can be directly compared.

In order to reach electron count rates sufficient for the recording of spin-resolved spectra within reasonable acquisition times using the RDM of the HHG source, the measurements were performed with a high pass energy ($E_{pass} = 32\text{ eV}$) and slit width ($w_1 = w_2 = 9\text{ mm}$) and thus, according to Eq. 3.1, a limited energy resolution of the spectrometer ($\Delta E_{CSA} \approx 1\text{ eV}$ is determined experimentally, see below). In addition, a sample bias of $U_{sample} = 16\text{ eV}$ was applied guiding more electrons to the detector at the expense of a reduced angular selection. The results of the spin-resolved photoelectron spectroscopy (PES) measurements with both light sources

¹Note that parts of this chapter are also subject of [Plötzing16].

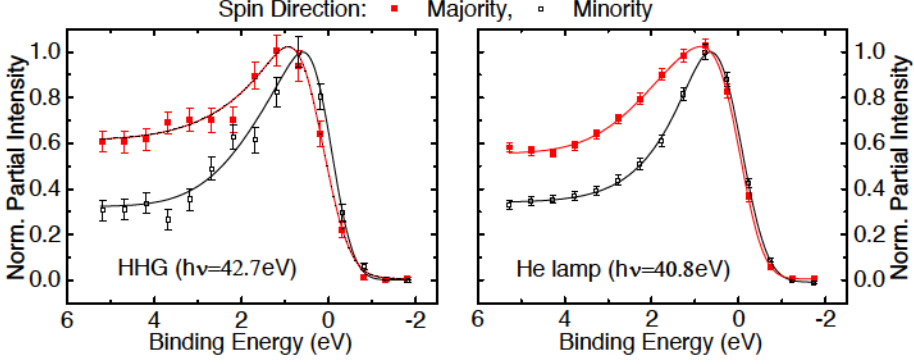


Figure 5.1: Partial intensities for minority and majority spin direction plotted against the electron binding energy. The results on the left side are measured with XUV pulses generated by the HHG source in RDM, the data on the right side with the He-II line of the cw photon source. In both cases a sample bias of $U_{\text{sample}} = 16$ eV was applied. In the plots, $E_B = 0$ is located at the Fermi level and the lines have been calculated from fits to the raw data (see text). (Adapted from [Plötzing16] with permission of AIP Publishing. The CC license does not apply.)

are shown in Fig. 5.1 and Fig. 5.2. The spectra were measured in normal emission on a 40 ± 12 ML thick Co(001) film. For the HHG source in RDM at a repetition rate of 3 kHz, a count rate of 10 counts/s is reached at the maximum of the valence band. At this energy, the total intensity per spin channel is > 1700 counts in the presented measurement.

In order to extract the energy resolution and the spectral width of the XUV light generated by the HHG source in RDM, the broadening of the Fermi edge was determined from the spectra obtained with both light sources. Therefore, the raw

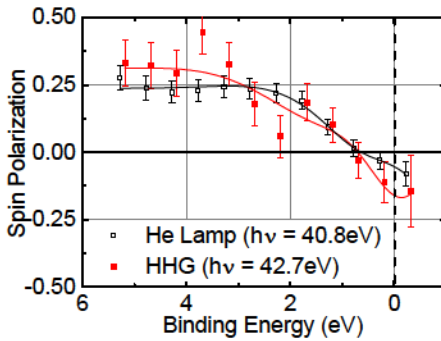


Figure 5.2: Spin polarization in Co(001) as a function of the electron binding energy. The results correspond to the data shown in Fig. 5.1. In the plots, $E_B = 0$ is located at the Fermi level and the lines have been calculated from fits to the raw data (see text). (Adapted from [Plötzing16] with permission of AIP Publishing. The CC license does not apply.)

intensity data was fitted with a convolution of a Gaussian peak function

$$f_b(E) = \exp\left(-\frac{E^2}{2c_b^2}\right) \quad (5.1)$$

and the function

$$f_s(E) = \left(\exp\left(\frac{E - E_F}{k_B T_{TR}}\right) + 1\right)^{-1} \cdot \left(a_p \cdot \exp\left(-\frac{(E - E_0)^2}{2c_p^2}\right) + y_0\right). \quad (5.2)$$

Here, $f_b(E)$ accounts for the total energy resolution of the setup including the spectrometer and the bandwidth of the light source. On the other hand, f_s represents the product of a Fermi-Dirac distribution for $T_{TR} = 300$ K with the sum of a constant background y_0 and another Gaussian peak function, which models the intensity peak from the $3d$ bands in the spectrum². Fitting the intensity distribution using only a single peak is justified, because the energy resolution used in the experiment does not allow the observation of further details in the band structure or the energetic separation of minority and majority spin contributions. In the equations, k_B is the Boltzmann constant, E_0 is the energetic position of the intensity peak and the coefficients $c_{b/p} = \Delta E_{b/p} / (2\sqrt{2 \cdot \ln(2)})$ represent the width of the Gaussian peaks with $\Delta E_{b/p}$ being the full width at half maximum (FWHM).

The total energy resolution of the setup ΔE_b is given as the quadratic sum of the contribution from the spectrometer (ΔE_{CSA}) and the light source ($\Delta h\nu_{RDM}$). The broadening in the measured spectra was determined from the data acquired with the detector being mainly sensitive to the minority spin electrons, because the density of states is higher for the minority channel in Co at E_F (see also Fig. 5.3). Neglecting the spectral width of the cw gas-discharge lamp, the spectrometer resolution for the settings in the RDM is given by $\Delta E_{CSA} = \sqrt{(\Delta E_{b,He-II})^2 - (\Delta h\nu_{He})^2} \approx \Delta E_{b,He-II} = 1.05 \pm 0.03$ eV. Since the total energetic broadening $\Delta E_{b,RDM} = 1.00 \pm 0.10$ eV for the measurement with the HHG source in RDM has the same size, we conclude that the spectrometer contribution dominates the energy resolution and the influence of the spectral width of the XUV pulses is significantly smaller. This is supported by the findings for $\Delta h\nu_{RDM}$ using the grating spectrometer in Sec. 3.1.

Within the limited energy resolution, the results obtained with the HHG source and the He-II line are in good agreement. The small deviations can be related to the low count rate and intensity fluctuations, which are considered in the error bars

²Note that the spectral lines intrinsically have a Lorentzian shape, which can be in addition asymmetrically broadened towards higher binding energies by inelastic scattering. However, this shape is washed out, *e.g.* because of the angular integration of the spectrometer or photoemission contributions from additional bands, making a Gaussian peak function better suited for the fitting procedure. Moreover, the shape of the spectra is dominated by the (Gaussian-shaped) instrumental energy resolution.

(see Sec. 3.2). For both measurements, the partial intensities (see Fig. 5.1) show a featureless part at binding energies $E_B > 3$ eV, which is dominated by majority spin electrons resulting in a spin polarization of $P \approx 0.25$ (see Fig. 5.2). In the region of the valence bands, the minority spin contribution increases, until the intensity for both spin directions is equal at $E_B = 0.7$ eV leading to $P = 0$. Then, both peaks decrease almost simultaneously at the Fermi edge. The strong negative value of the spin polarization close to E_F , which is observed in the measurements in Sec. 4.2, is not present. However, the experimental conditions for the data presented in this section differ from the ones used for the results in Fig. 4.5 not only by the energy resolution, but also by the photon energy.

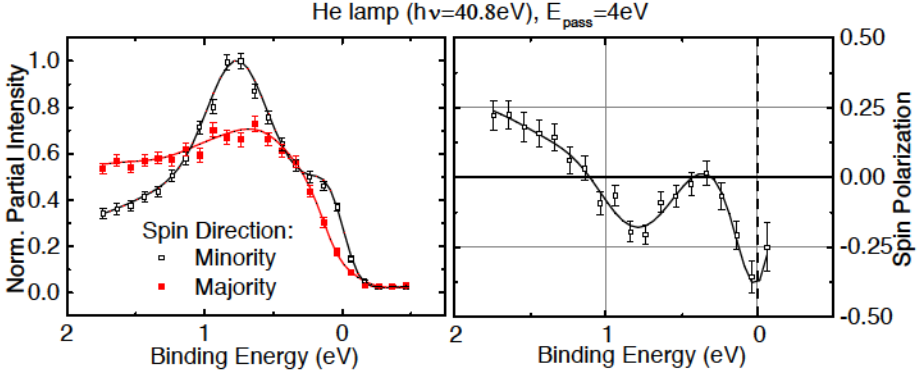


Figure 5.3: Partial intensities and spin polarization distribution from Co(001) as a function of the electron binding energy measured with a high spectrometer resolution. The measurements were performed using the He-II line of the gas-discharge lamp with a pass energy of 4 eV and no sample bias. In the plots, $E_B = 0$ is located at the Fermi level and the lines have been calculated from fits to the raw data (see text).

In order to understand the influence of the photon energy, measurements with a better spectrometer energy resolution and without sample bias were performed using the He-II line on similar samples (see Fig. 5.3). Decreasing the pass energy to 4 eV leads to an energy resolution of $\Delta E_{b2, He-II} = 0.22 \pm 0.03$ eV for the obtained results, which was again determined by a fit to the data similar to the one presented before. However, this time the sum of two separate Gaussian peak functions was used in order to account for the separation of the majority and minority spin electron peaks. The results show that the minority peak moves to higher binding energies ($E_B = 0.8$ eV) compared to the measurements with the He-I line in Sec. 4.2. Assuming a free-electron final state model (see Sec. 2.2.1 and Sec. 3.1), electrons with a wave vector k_{\perp} close to Γ are excited by the He-II line, whereas the He-I line selects electrons from the middle of the $\Gamma - X$ direction of the bulk Brillouin zone (BZ). The observed change of the position of the minority peak is in

good agreement with the dispersion of the $\Delta_{5\downarrow}$ band predicted by band structure calculations (see Fig. 2.3 [Chiang10]).

Besides, the difference in the EDCs leads to a more complex structure of the spin polarization (see right side of Fig. 5.3), which flips its sign already at $E_B = 1.2$ eV, but is then reduced again to $P = 0$ in the range where the influence of the minority band is vanishing ($E_B = 0.3$ eV). Close to E_F , no majority spin contribution is left and thus P has a high negative value again.

Figure 5.4 shows the results of a similar measurement as in Fig. 5.3, but recorded using a pass energy of 32 eV. Due to the resulting inferior energy resolution, the features are smeared out. The dip in P at $E_B = 0.3$ eV found in the measurements with $E_{pass} = 4$ eV is strongly suppressed and only the change of the sign at $E_B = 1.2$ eV is still clearly visible. Furthermore, the spin polarization and therefore the difference of the partial intensities at the position of the minority spin electron peak ($E_B = 0.8$ eV) was significantly reduced.

However, a comparison of the results shown in Fig. 5.4 with the data presented in Fig. 5.1 reveals still a difference for the values close to E_F even though the spectrometer setting have been the same. A possible explanation is the influence of the sample bias, which is present only for the measurements in Fig. 5.1. The resulting electric field bends the trajectories of additional electrons with higher emission angles into the detector causing an additional smearing over a broader part of the BZ.

The results in this section show that the HHG source in RDM can be used for spin-resolved photoelectron spectroscopy without fundamental restrictions. Nevertheless, it provides only low photon flux resulting in a limited energy resolution and

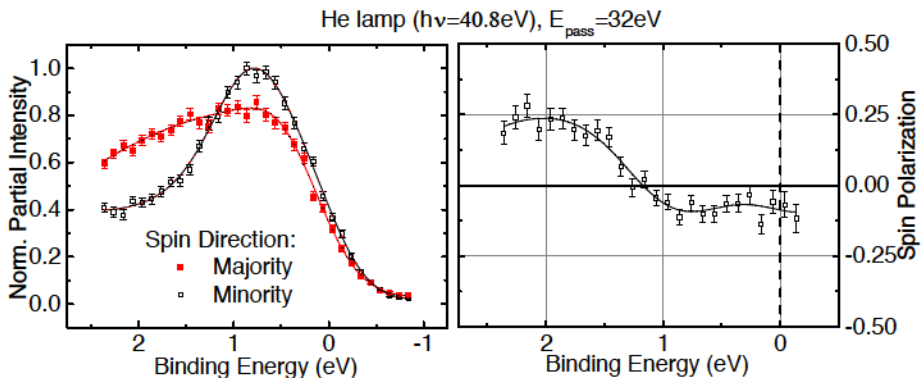


Figure 5.4: Spin-resolved EDCs of Co(001) and corresponding spin polarization, measured without sample bias. The settings of the spectrometer were similar to the measurements in Fig. 5.1 and Fig. 5.2 but without sample bias. In the plots, $E_B = 0$ is located at the Fermi level and the lines have been calculated from fits to the raw data (see text).

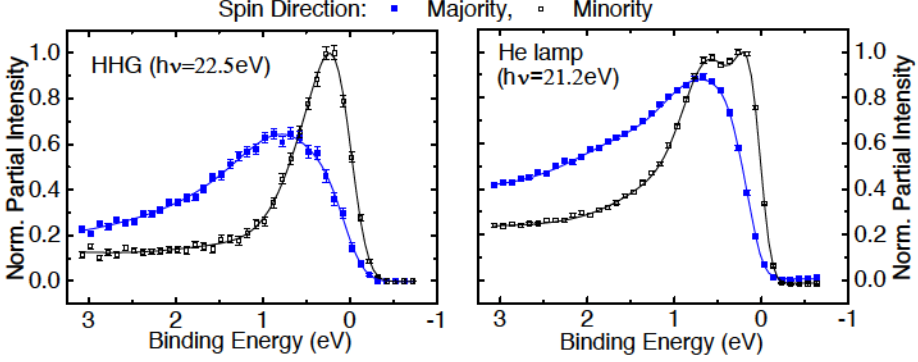


Figure 5.5: Energy distribution of the partial intensities for the minority and majority spin direction. The measurements were performed using the pulsed HHG source in BDM (left) and the He-I line of the cw gas-discharge lamp (right) under the same conditions. In the plots, $E_B = 0$ is located at the Fermi level and the lines have been calculated from fits to the raw data (see text). (Adapted from [Plötzing16] with permission of AIP Publishing. The CC license does not apply.)

long acquisition times. This makes it at present impossible to map optically induced changes in the band structure by recording full valence band spectra. However, time-resolved traces at special, interesting binding energies may be still possible. In addition, this mode will become more important with improving HHG sources and spin detectors, because of the broad range of accessible photon energies (see Sec. 3.1).

5.2 Blue-Driven Mode

The findings presented above demonstrate that the photon flux limits the usability of the RDM for time-resolved studies. In contrast, the HHG source in BDM provides significantly more flux (see Sec. 3.1). Thus, the measurements were performed in this case without sample bias and with a pass energy in the spectrometer of $E_{pass} = 4$ eV. The results for a Co(001) film with a thickness of $d = 20 \pm 5$ ML at $k_{\parallel} = 0$ are presented in Fig. 5.5 and Fig. 5.6. In the BDM, the photon energy is $h\nu_{BDM} = 22.5$ eV (see Sec. 3.1), which is close to the He-I emission line ($h\nu_{He-I} = 21.2$ eV) produced by the gas-discharge lamp.

A comparison between the partial intensities obtained with the HHG source (left side of Fig. 5.5) and the He-I line (right side) reveal two major differences: the data acquired using the gas-discharge lamp shows more intensity for both spin directions at higher binding energies and a second peak in the minority spin electron channel. Since both measurements were performed consecutively on the same sample, a

change of the crystalline order or a different influence of overlayers from adsorbed material can be excluded. As discussed in Sec. 3.1, the HHG source provides linearly polarized light, which had a vertically aligned field vector for the measurements in this section, whereas the radiation from the gas-discharge lamp is unpolarized. According to the dipole selection rules (see Sec. 2.2.1), the light from the HHG source can thus only excite electrons from an initial state with Δ_5 symmetry. In contrast, Δ_5 - and Δ_1 -states are accessible using the He-I light. Therefore, additional states can contribute to the photoemission spectra measured with the gas-discharge lamp and cause the difference in the intensity at high binding energies. Especially for the majority spin direction, bands with Δ_1 character are present in the corresponding region of the BZ (see Fig. 2.3 [Chiang10]). The double-peak structure for the minority spin electron direction that is observed with the light from the He-I line can be assigned to a $\Delta_{5\downarrow}$ band ($E_B = 0.2$ eV) and to a surface resonance ($E_B = 0.7$ eV), as already discussed in Sec. 4.2. In contrast, the even symmetry of the surface resonance makes it inaccessible for the light from the HHG source and thus the corresponding feature is missing in the EDC plotted on the left side of Fig. 5.5.

For the spin polarization (see Fig. 5.6), a constant value of $P = 0.3$ is observed at high binding energies ($E_B > 2.5$ eV) in both measurements. However, in the data acquired with the HHG source the flank of the majority spin electron peak ($E_B = 0.9$ eV) increases the spin polarization starting at $E_B = 2.5$ eV to a value of almost $P = 0.5$ at $E_B = 1.2$ eV. In the results obtained with the He-I line, this effect is equalized and even overcompensated by the flank of the surface resonance. Here, the latter causes a decrease of P to ≈ -0.05 at $E_B = 0.6$ eV, which is then followed by the dominance of the $\Delta_{5\downarrow}$ band leading to an even higher negative P between $E_B = 0.4$ eV and the Fermi edge. In contrast, the spin polarization decreases for the data measured with the HHG source in one step between $E_B = 1.1$ eV and the Fermi edge crossing zero at $E_B = 0.5$ eV. At E_F the spin polarization has a value of $P \approx -0.6$ eV for both light sources.

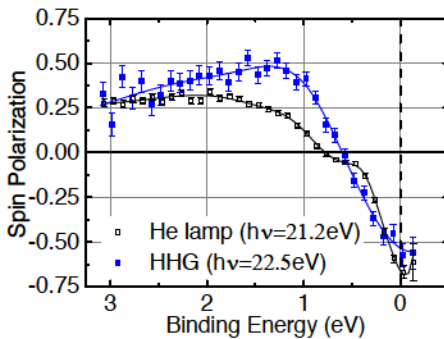


Figure 5.6: Spin polarization as a function of the electron binding energy. The corresponding partial intensities are shown in Fig. 5.5. In the plots, $E_B = 0$ is located at the Fermi level and the lines have been calculated from fits to the raw data (see text). (Adapted from [Plötzing16] with permission of AIP Publishing. The CC license does not apply.)

The raw intensity data is fitted similar to Sec. 5.1. However, this time two Gaussian functions are used to model the spectrum for the HHG measurement in order to take into account both the peak in the minority and the majority spin direction. For the results obtained with the He-I light, another, third Gaussian peak function is included to consider the surface resonance. Again, from the fits to the EDC dominated by minority spin electrons, the influence of the spectrometer and the light source on the energy resolution can be determined. Values of $\Delta E_{b,BDM} = 0.35 \pm 0.01$ eV and $\Delta E_{b,He-I} = 0.23 \pm 0.02$ eV are extracted. Assuming a spectrally sharp He-I line and thus $\Delta E_{CSA} \approx \Delta E_{b,He-I}$, the bandwidth of the HHG source in BDM can be calculated as

$$\Delta h\nu_{BDM} = \sqrt{(\Delta E_{b,BDM})^2 - (\Delta E_{CSA})^2} = 0.26 \pm 0.02 \text{ eV}. \quad (5.3)$$

For the measurement with the HHG source in BDM that is presented in Fig. 5.5, the count rate at the maximum intensity is 400 counts/s (spectrum dominated by the minority spin direction). The total intensity at this point summed up over the entire integration time is > 9500 counts. It has to be noted that the repetition rate of the source was increased to $f_{rep} = 5$ kHz compared to the measurements in RDM and that the photon flux was reduced in order to decrease the influence of vacuum space-charge (VSC) effects. A more detailed explanation of VSC and a corresponding characterization of our setup will be given in the next section (Sec. 5.3). Using already the results of this characterization, the additional energetic broadening caused by VSC can be approximated to $\Delta E_{vsc} = m_{broadening} \cdot \rho < 0.08$ eV (see Eq. 5.8 for $m_{broadening}$) for the (linear) photoelectron density³ (see Sec. 5.3) $\rho \approx 3.5 \cdot 10^4 \text{ mm}^{-1}$ that was achieved in the experiment. Therefore, it is low enough to avoid a significant degradation of the energy resolution.

In general, a further reduction of the total energy resolution in the measurements performed with the XUV pulses is possible by decreasing the spectral width of the light. This can be achieved using, *e.g.*, a grating monochromator [Carley12] or a further improvement of the light source [Eich14, Wang15]. However, this can increase the pulse duration due to the time bandwidth product (TBP) and therefore reduce the time scale accessible with the experiment. The TBP states that the minimum duration of a pulse Δt_{pulse} is related to its spectral width $\Delta h\nu$ by [Diels06]

$$\Delta t_{pulse} \cdot \frac{\Delta h\nu}{h} = 0.441 \quad (5.4)$$

for pulses having a Gaussian distribution in time. For the given parameters in the BDM ($h\nu = 22.5$ eV and $\Delta h\nu_{BDM} = 0.26$ eV), the minimum pulse duration is $\Delta t_{pulse} = 7$ fs. Thus, for further reductions of the broadening induced by the spectral width of the HHG source, the necessary temporal resolution has to be

³The spot area of the driving laser on the sample was $A = 2.6 \text{ mm}^2$.

considered.

The acquisition time for the spin-resolved spectra presented in this section of ≈ 1 h shows that simultaneous energy- and spin-resolved investigation of the valence bands at several time steps are possible before the sample quality degrades under ultrahigh vacuum (UHV) conditions (see Chap. 3). Therefore, the HHG source in BDM is well-suited for studies of the temporal evolution of optically induced processes on the femtosecond time scale in a pump-probe experiment.

5.3 Vacuum Space-Charge Effects Induced by Extreme Ultraviolet Light Pulses

The results presented in the previous section reveal that one of the main challenges in photoemission experiments with ultrashort pulses is vacuum space-charge (VSC) caused by the Coulomb repulsion between the photoemitted electrons. The left side of Fig. 5.7 shows two typical EDCs of the Cu(001) $3d$ valence bands obtained with different intensities of the XUV light. Like all measurement in this section, both spectra have been recorded using the HHG source in BDM with a repetition rate of 3 kHz. For the higher intensity (black open circles), the peak is shifted and broadened compared to the spectrum acquired with lower photon flux (blue filled squares).

The described effects are accompanied by a distortion of the angular and spatial information of the photoelectrons [Zhou05] and have been reported for time-resolved electron diffraction [Srinivasan03] as well as photoemission experiments using pulsed lasers [Passlack06], free-electron lasers (FELs) [Pietzsch08] or HHG sources [Frietsch13]. However, the parameters (intensity, pulse width, pulse power) of these light sources are widely spread and thus a criterion where VSC effects start to occur can not be universally derived. In general, the excitation with sub-picosecond light pulses leads to the emission of quasi-two-dimensional electron disks [Hellmann09]. This is in contrast to photoemission experiments based on cw light sources, where the excitation is homogeneously spread in time. For the same average count rate, the distance between the photoelectrons is thus much smaller for the ultrashort bunches leading to a significant Coulomb repulsion between the electrons. Depending on its individual environment and the distribution of neighbors, each electron experiences a repulsive force along, opposite or of a certain angle with respect to its direction of motion. Therefore, electrons can be either accelerated or decelerated causing the broadening of the observed spectral features [Zhou05]. On the way to the spectrometer, the photoelectrons arrange in the order of their kinetic energy. The valence band electrons measured in our experiments leave the sample with the highest E_{kin} . Thus, they are mainly located at the leading part of the elec-

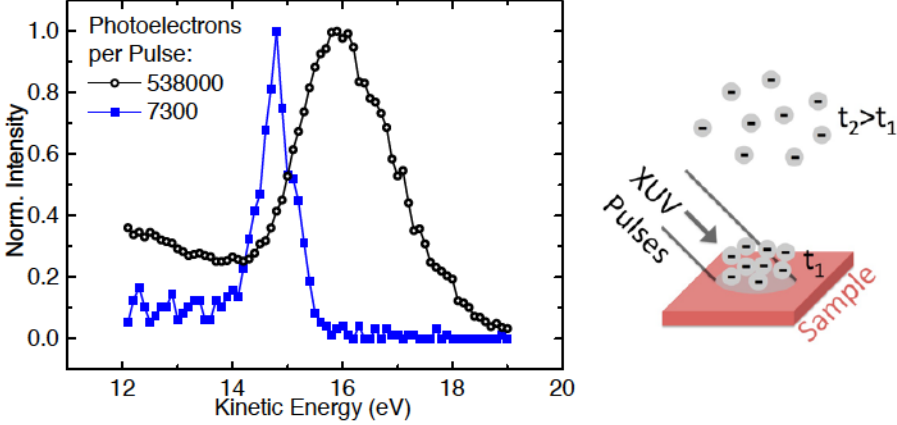


Figure 5.7: Left: Photoemission spectra measured with different flux of the femtosecond XUV pulses. The data was acquired in normal emission using the HHG source in BDM on Cu(001). In the measurement represented by the black open circles over 70 times more photoelectrons are created per pulse than for the one displayed by blue filled squares. This leads to spectral distortions. (Adapted from [Plötzing16] with permission of AIP Publishing. The CC license does not apply.) **Right: Scheme of the effect of vacuum space-charge.** A dense photoelectron cloud is created in front of the sample (t_1). While propagating (t_2), it is enlarged due to the Coulomb repulsion between the electrons. (Adapted from [Plötzing16] with permission of AIP Publishing. The CC license does not apply.)

tron cloud and are followed by a larger number of slower electrons containing the secondary electrons generated by scattering inside the sample. Consequently, the latter repel and thus accelerate the valence band electrons during their propagation to the spectrometer leading to the observed shift to higher kinetic energies (see right side of Fig. 5.7 and [Zhou05, Hellmann09]). At the same time, a positive potential can be present in the sample that partly compensates the acceleration by the VSC. On ultrashort time scales below 100 fs [Campillo00], the holes left behind by the photoelectrons generate such a positive potential. Moreover, the electric field of the electron cloud propagating in front of the surface is shielded by a charge redistribution inside the metallic sample that creates a counteracting field.

In order to characterize the influence of VSC for our experimental conditions, we recorded spectra of the Cu(001) 3d bands in normal emission for a broad range of XUV light intensities. In addition, we varied the spot size to verify results of previous studies [Passlack06, Hellmann09] that found a dependence of the peak shift and broadening on the ratio

$$\rho = \frac{N_{pulse}}{d_{FWHM}}. \quad (5.5)$$

Here, N_{pulse} is the number of electrons per laser pulse and d_{FWHM} is the diameter

5.3. VACUUM SPACE-CHARGE EFFECTS INDUCED BY EXTREME ULTRAVIOLET LIGHT PULSES

of the electron disk. This dependence can be related to the Coulomb potential that charges feel in the initial disk due to the surrounding electrons and that has the same form [Hellmann09]. The diameter of the electron disk is approximated using the size of the light spot, which can be extracted from pictures of the sample crystal taken with a charge-coupled device (CCD) camera, where the spot of the impinging light is visible. However, a direct observation of the XUV spot employing fluorescent material (see Sec. 6.1) is challenging if the HHG source is not used with maximum photon flux. Instead, the spot of the driving laser was monitored assuming a similar size as the XUV spot, because both beams were defined by the same iris aperture placed in front of the toroidal mirror. d_{FWHM} was then determined by fitting a rotated two-dimensional Gaussian peak function⁴ to the intensity data of the picture (see Fig. 5.8). Pixel values were converted into distances taking the known crystal size for reference. Furthermore, the number of photoelectrons N_{pulse} was

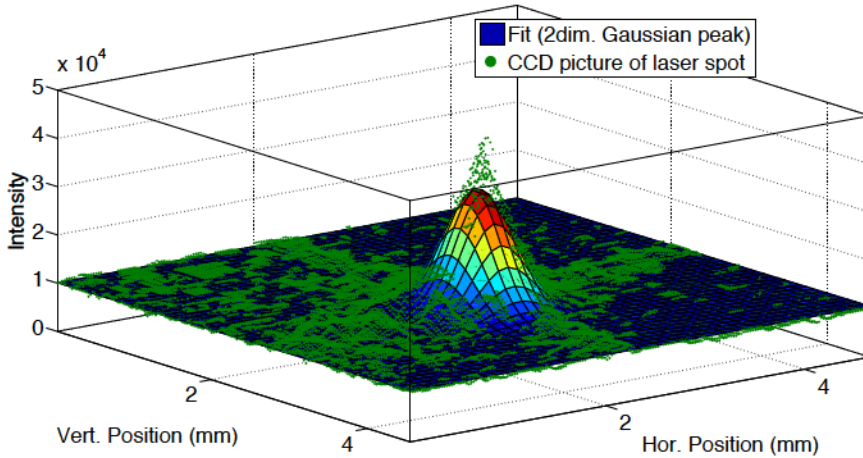


Figure 5.8: Determination of the laser spot size. The z-values of the green dots represent the light intensity on a CCD camera. They are plotted as a function of the position. Then, the FWHM of a rotated two-dimensional Gaussian peak function fit (colored plane) is taken as the spot size.

calculated from the photocurrent, which we recorded during the experiment with a femto-amperemeter. The determination of the error bars for the photoelectron

⁴Rotated means that the two independent width directions of the Gaussian profile do not have to be collinear with the x- and y-axis of the CCD picture.

density ρ is performed by error propagation based on the standard deviation of the photocurrent measurements.

The FWHM of the Cu(001) 3d peaks E_{FWHM} and their positions E_{pos} are determined from Gaussian peak function fits to the EDCs and the values extracted from the measurement with the lowest photon flux are taken as the intrinsic width $E_{FWHM,0}$ and position $E_{pos,0}$. Then, the energy shift

$$S_{sc} = E_{pos} - E_{pos,0} \quad (5.6)$$

is calculated by linear subtraction of the intrinsic value. In contrast, the broadening is given by quadratic subtraction as

$$\Delta E_{vsc} = \sqrt{E_{FWHM}^2 - E_{FWHM,0}^2}, \quad (5.7)$$

because it is treated, similar to an energy resolution contribution, as a convolution of two Gaussian peak functions that model the intrinsic peak in the spectrum and its widening.

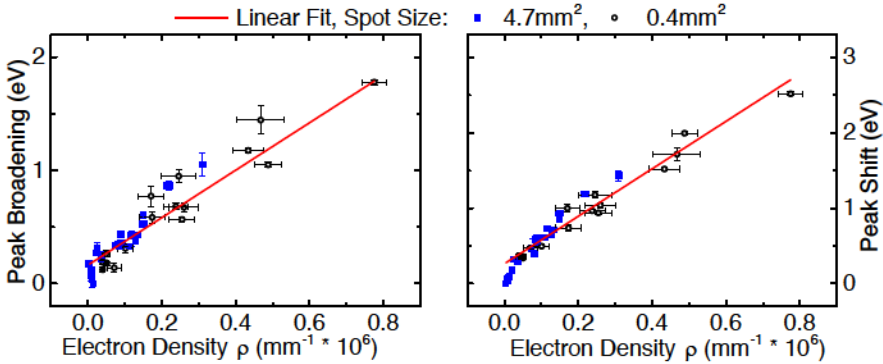


Figure 5.9: Distortion of spectral features by VSC effects. Peak broadenings (left) and shifts (right) are plotted against the (linear) photoelectron density per pulse ρ (see Eq. 5.5). The results were determined from photoemission spectra of the Cu(001) 3d peak (see left side of Fig. 5.7). Blue filled and black open symbols indicate measurements with different spot sizes and the red line represents a linear fit to all values with $\rho > 2.5 \cdot 10^4 \text{ mm}^{-1}$. (Adapted from [Plötzing16] with permission of AIP Publishing. The CC license does not apply.)

In Fig. 5.9, the broadening (left side) and shift (right side) of the electron peak created by the 3d electrons in Cu(001) are presented as a function of ρ (see Eq. 5.5). The curves show a good agreement between the values measured with the smaller ($A = 0.4 \text{ mm}^2$, blue filled squares) and the larger spot area ($A = 4.7 \text{ mm}^2$, black open circles) for both the peak broadening and the peak shift even though A differs by more than a factor of 10. This confirms the suggested linear dependence on

5.3. VACUUM SPACE-CHARGE EFFECTS INDUCED BY EXTREME ULTRAVIOLET LIGHT PULSES

d_{FWHM}^{-1} [Hellmann09].

Furthermore, the photoemission peak broadening as well as the shift show a linear dependence on the photoelectron density for $\rho > 2.5 \cdot 10^4 \text{ mm}^{-1}$ if the number of photoelectrons is varied. The deviation from this behavior for $\rho < 2.5 \cdot 10^4 \text{ mm}^{-1}$ can be explained, because below this value the measurement of the photocurrent approaches the background level and in addition the peak shift and broadening are close to the intrinsic width of the peak⁵ (see blue filled squares on the left side of Fig. 5.7). A linear regression in the region $\rho > 2.5 \cdot 10^4 \text{ mm}^{-1}$ yields the slopes

$$m_{\text{broadening}} = 2.10 \cdot 10^{-6} \text{ eV} \cdot \text{mm} \quad (5.8)$$

for the peak broadening and

$$m_{\text{shift}} = 3.15 \cdot 10^{-6} \text{ eV} \cdot \text{mm} \quad (5.9)$$

for the peak shift. Here, the dependence of the shift on ρ shows a steeper slope than the corresponding dependence of the broadening. However, a comparison with literature suggests that this particular behavior depends crucially on the exact experimental conditions. In experiments using synchrotron radiation with significantly lower ρ the opposite was observed and the authors suggest that the energy difference between the interacting electrons determines which effect is dominant [Zhou05]. Similarly, Frietsch *et al.* reported a larger peak broadening than shift in valence band photoemission experiments, but here the authors relate the effect to an additional broadening contribution due to fluctuations of the light source [Frietsch13]. Core-level photoemission experiments as well as corresponding simulations also revealed a steeper slope for the peak broadening compared to the shift [Hellmann12]. In contrast, simulations performed with the same code as used in the core-level investigations suggest the behavior that we observed for valence band spectroscopy [Hellmann09]. The slopes that the authors of [Hellmann09] determine for the case of valence band photoemission are a factor of 2 smaller for both the broadening and the shift than our experimental findings. Nevertheless, similar differences in the slopes between their model and experimental results find Hellmann *et al.* also for other examples. The authors attribute the deviations to uncertainties in the determination of the exact experimental conditions. In our case, the uncertainties are most likely dominated by the measurement of the spot size, where the driving laser and not the XUV beam is taken into account. Moreover, in reality the measured distribution of the light intensity within the spot slightly differs from the ideal Gaussian shape assumed for the fit (see Fig. 5.8) due to, *e.g.*, the presence of higher-order transverse laser modes or reflectivity inhomogeneities of the crystal surface.

The results discussed above give us an indication of the maximum photoelectron density that can be achieved without significant distortions of the photoemission

⁵The uncertainties induced by the photocurrent background level are not included in the determination of the error bars.

spectrum due to VSC. In order to keep the broadening $m_{\text{broadening}} \cdot \rho$ at ≈ 0.1 eV, which is far below the energy resolution of the measurements with the HHG source in BDM (see Sec. 5.2), the photoelectron density should not exceed $\rho_{\text{max}} = 5 \cdot 10^4 \text{ mm}^{-1}$. In general, the maximum count rate in photoemission while staying below this limit can only be reached by carefully adjusting the experiment to the requirements of the particular study. For example, the spot size can be increased allowing for a higher number of photoelectrons per pulse. On the other hand, this will decrease the momentum resolution in angle-resolved photoelectron spectroscopy (ARPES) experiments. Moreover, it will lead to further complications in time-resolved experiments, because high pump fluences of the order of 10 mJ/cm^2 are necessary for, *e.g.*, demagnetization experiments. Such fluences can only be reached with focused beams for common laser systems.

A second approach to minimize VSC contributions while still improving the detected photoemission intensity is to distribute the photoelectrons over a larger number of pulses by increasing the repetition rate of the XUV source. This approach is very successfully applied for HHG light sources (see Sec. 2.3), but it requires a modification of the repetition rate of the laser system which at the same time leads to smaller pulse energies available for the HHG process. Below a certain threshold, the conversion efficiency of the frequency-upconversion depends nonlinearly on the incoming pulse intensity (see Sec. 2.3.3 and [Falcão-Filho10]). In this region, the XUV photon flux significantly drops for a small decrease of the pulse intensity and, in addition, pulse-to-pulse fluctuations of the laser lead to strong variations of the XUV intensity.

6 Towards Femtosecond Time-Resolved Photoemission

In the previous chapter, the photoemission from extreme ultraviolet (XUV) light pulses created with the high-order harmonic generation (HHG) source is characterized and experimental conditions that allow time-resolved measurements are determined. For pump-probe experiments, additional near-infrared (NIR) pump-pulses are used to excite the transient process under investigation in our setup. The XUV and NIR pulses have to overlap both spatially and temporally at the sample surface. The first part of this chapter addresses the question of how these two conditions can be fulfilled. In the second part, the influence of the pump-beam in terms of vacuum space-charge (VSC) effects (see Sec. 5.3) is characterized, because it creates additional photoelectrons contributing to the Coulomb interaction. Finally, the time interval providing stable conditions for pump-probe measurements is investigated. All experiments in this chapter that use XUV radiation are performed with the HHG source in the blue-driven mode (BDM) (see Sec. 3.1).

6.1 Temporal and Spatial Pump-Probe Overlap

In order to achieve the temporal overlap between the XUV pump- and NIR probe-beam, the delay stage position (see Sec. 3.1), for which the pulses of both beams arrive at the sample at the same time (zero delay (ZD)), has to be determined. This position can be roughly approximated using sum frequency generation in a β -BaB₂O₄ (BBO) crystal (Type 1, $\theta_{cut} = 44.3^\circ$) from the 390 nm driving laser of the HHG process and the 780 nm pump-beam. Since for this purpose the 390 nm beam has to enter the photoemission chamber, the Al foil which is usually used to block it (see Fig. 3.1) can be replaced by a borosilicate glass window. For the measurement, the BBO crystal is placed behind the photoemission chamber as shown in Fig. 6.1. The beams then propagate through the chamber and leave it again via another borosilicate glass window. In the non-linear process in the BBO, light with a wavelength of 260 nm is produced by summing up a photon from each of the original

beams if both pulses are present at the same spot and the same time on the crystal¹. Consequently, the position of the ZD can be found by scanning over the delay stage positions and monitoring the appearance of the additional beam. This technique allows one to scan a delay range of several hundreds of picoseconds within minutes and, consequently, it is very useful to find the ZD after applying changes to the beam path.

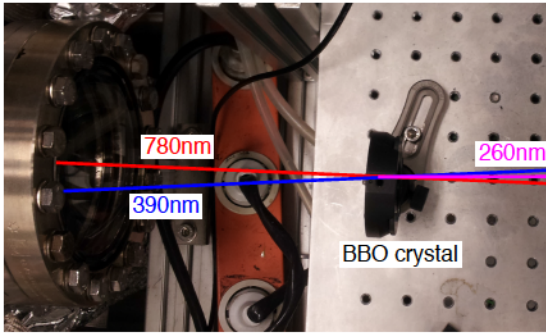


Figure 6.1: Experimental geometry of the zero delay measurement via sum frequency generation. If pump- and probe-pulses overlap in the BBO crystal, a third outgoing beam is generated that has a photon energy determined by the sum of the incoming beams. In order to improve the clarity, the angles are enlarged in the illustration compared to the real situation.

From the position where both beams arrive at the same time on the BBO crystal, the ZD at the measurement position is only approximately known because the spatial overlap of the beams has to be varied and because both beams propagate with different velocities through the borosilicate exit window. A more accurate determination of the ZD on the sample can be realized using multiphoton-photoemission. However, this method is more time consuming and thus only reasonable for scanning a small delay range in the vicinity of the ZD measured using the BBO crystal. It is based on the idea that typical metallic work functions ϕ (for Co, $\phi = 4.8$ eV [Wallauer96]) can not be overcome by a single photon of the 780 nm or 390 nm light having a photon energy of 1.6 eV and 3.2 eV, respectively. Nevertheless, a photoelectron can be released if several photons are absorbed. This is more probable at the ZD, where photons of both beams are present in the sample at the same time leading to an enhancement of the signal. A typical measurement² of this count rate enhancement is represented by the black squares in Fig. 6.2. The background signal (triangle symbols) is generated by multiphoton processes from the single beams. As already introduced in Sec. 5.3, a charge-coupled device (CCD) camera has been used to monitor the beams on the sample surface and to ensure the spatial overlap. Besides the determination of the ZD, the cross-correlation signal of the two-photon-photoemission enhancement can be used to estimate the temporal resolution

¹The 260 nm light can be detected by fluorescence from paper.

²A result for Ni is shown because for this measurements data for the background count rate from the single pulses as well as a corresponding determination of the pump-pulse duration is available. The enhancement effect for Ni and Co is similar since both materials have comparable work functions.

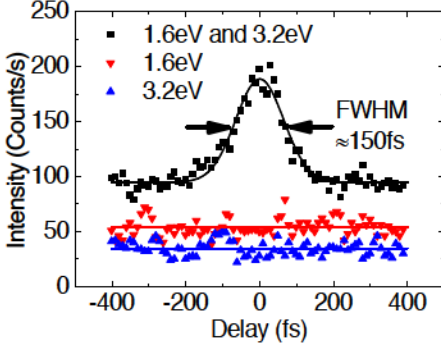


Figure 6.2: Enhancement of the multi-photon photoemission count rate at the zero delay. The red down-pointing (blue up-pointing) triangles show data acquired with only the pump (driving laser of the HHG source) arriving at the sample. For the black data points both beams (vertically polarized) are present on the same spot on the sample surface. The full lines represent fits of a constant value for the single beam measurements and a Gaussian peak function for the measurement with both beams. Photoelectrons with $E_{kin} = 0.8$ eV are detected. The sample is a thin Ni film (see text/footnote) grown on Cu(001) having a work function comparable to Co/Cu(001) [Huang84].

in our experiment assuming a negligible lifetime of the intermediate state. The fit of a Gaussian peak function yields a full width at half maximum (FWHM) of the cross-correlation signal of 150 fs for the measurement presented, being dominated by the pump-pulses, which have a comparable duration at the sample position³. This finding is also valid if the XUV pulses from HHG are used instead of the 390 nm driving-beam (see Sec. 7.1) because the HHG process generally reduces the pulse duration [Miaja-Avila06].

Compared to the ZD between the 780 nm pump- and 390 nm driving-pulses, the ZD between the 780 nm pump- and the XUV probe-pulses exhibits still a shift of the order of 1 ps, because the 390 nm pulses are slowed down in the borosilicate glass window which is significantly thicker than the Al foil. The accurate position of the ZD between these pulses can be measured using the laser-assisted photoelectric effect (LAPE) [Miaja-Avila06] as shown in Sec. 7.1.

In order to establish the spatial overlap between the NIR pump- and the XUV probe-pulses, again pictures from the CCD camera were used. For this purpose, the XUV light is transferred into the visible spectral range using a sample covered with a film of fluorescent material placed at the sample position. A typical picture of the XUV spot taken with this method is shown in Fig. 6.3. It additionally shows the position of the laser beam driving the HHG process (blue ellipse). Both beams are in general guided to almost the same position on the sample. Nevertheless, fits of rotated two-dimensional Gaussian peak profiles⁴ reveal an offset of ≈ 0.2 mm. Therefore, the spatial pump-probe overlap can not be established using the 390 nm

³Before entering the vacuum through the borosilicate window, the pump-pulse duration was determined to be 131 fs using an optical autocorrelation measurement via frequency-doubling in a BBO crystal. While passing through a lens and the dispersive glass window, the pulses are further stretched to > 145 fs.

⁴An example of such a fit is shown in Fig. 5.8.

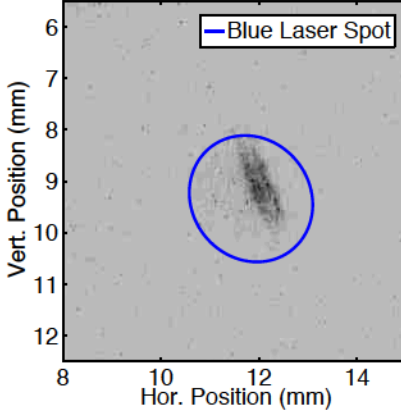


Figure 6.3: Picture of the XUV spot. It is taken with a CCD camera and the XUV light is converted to the visible spectral range using a film of fluorescent powder. Real dimensions at the measurement position are calibrated using the known size of the sample holder. The blue ellipse represents the FWHM border of the spot from the 390 nm driving laser on the sample, determined with a rotated two-dimensional Gaussian peak function fit (see Fig. 5.8).

driving laser that is directly visible on the sample, but has to be adjusted using the NIR and the XUV light on a surface covered with fluorescent pigments. It has to be placed exactly at the measurement position.

6.2 Pump-Induced Photoelectrons & Resulting Space-Charge Contribution

For the high fluences of the order of 10 mJ/cm^2 , which are necessary to trigger demagnetization processes, it is known that the femtosecond pump-pulses excite photoelectrons even though the photon energy of $h\nu = 1.6 \text{ eV}$ is far below the work function of $\text{Co}(001)$ ($\phi = 4.8 \text{ eV}$ [Wallauer96]) [Yen80, Riffe93, Aeschlimann95]. When arriving at the spectrometer, these photoelectrons can reach kinetic energies of several tens of eV. Thus, they are as fast as the photoelectrons excited from the valence band using XUV light.

In general, the underlying effects have been studied to some extent, but are not fully understood yet and several competing mechanisms have been proposed⁵. At small peak intensities ($< 1 \text{ GW/cm}^2$ [Riffe93]), purely multiphoton photoemission processes are believed to be dominant for the electron emission. In the intermediate intensity range, the electron system is significantly excited by the ultrashort laser pulses leading to a transient states where electrons are present above the Fermi level (see Sec. 7.1). The excited electrons can strongly support the multiphoton photoemission because they have a reduced energy difference to the vacuum level and therefore multiphoton processes of a lower order can be sufficient to emit them

⁵A more detailed review of the state of research is given, *e.g.*, in [Ferrini09].

[Yen80]. This process is called "thermally assisted multiphoton photoemission" since the electron system can be regarded as heated during the transient state. However, it is not in equilibrium with the lattice. The influence of the transient heating of the electron system increases for higher peak intensities and even pure thermionic emission has been observed [Riffe93]. In addition, tunnel-ionization occurs for high peak intensities exceeding 300 GW/cm^2 [Ferrini09]. Assuming a Gaussian temporal structure, the peak intensities of our pump-pulses are in the range of

$$\frac{I_{peak}}{A} \approx 0.94 \frac{F}{\tau_p} \approx 100 \frac{\text{GW}}{\text{cm}^2} \quad (6.1)$$

for a laser fluence of $F = 10 \text{ mJ/cm}^2$ and a duration of the pump-pulse of $\tau_p = 100 \text{ fs}$ (A : spot size). Thus, our experimental conditions are mainly located in the regime of thermally assisted multiphoton photoemission, which can be described by a generalized Fowler-DuBridge approach [Yen80].

However, the latter excitation mechanism is not capable of satisfactorily explaining the photoelectrons, which were observed in the spectra at kinetic energies far higher than expected for multiphoton processes. The effects leading to these fast photoelectrons are still under debate⁶. The discussion includes the possibility of acceleration, *e.g.*, by the ponderomotive force of the electric field of the laser pulse, especially if it is enhanced by surface-plasmons [Kupersztynch01, Dombi13], or by VSC (see Sec. 5.3). A strong contribution from surface-plasmons, in particular propagating ones, is not probable in our Co films, because the coupling of the light to surface-plasmons is in general weak for flat metal-vacuum interfaces and additionally surface-plasmons are strongly damped in $3d$ ferromagnets [Zayets12]. In contrast, VSC effects can cause energetic distortions of several eV for the photoelectron densities of the order of $10^5 - 10^6 \text{ mm}^{-1}$ that are reached in our experiments (see Fig. 5.9). Therefore, we believe that the latter mechanism is giving the dominant contribution in our studies. Nevertheless, it is beyond the scope of this thesis to develop an advanced understanding of the underlying processes. Thus, the investigations conducted in the first part of this section mainly focus on the reduction of the amount of pump-induced photoelectrons in our experiment by varying relevant parameters. In the second part, the influence of the additional photoelectrons on our time-resolved measurements is characterized, in particular concerning their contribution to VSC.

6.2.1 Photoelectron Emission by Near-Infrared Light

In order to study their influence on the NIR pump-induced emission of photoelectrons, we subsequently varied the measurement position, the light polarization, the pulse duration, and the laser fluence. The results of the measurements for the single parameters will be presented in the following paragraphs.

⁶Several mechanisms are considered, *e.g.*, in [Banfi03].

First, spectra were recorded for different positions of the NIR laser spot on the sample⁷ (see Fig. 6.4). We find that the change of the position strongly affects the photoelectron yield. This can be seen from the sample current I , stated in the legend of the plot, which varies significantly for the different spot positions. It has to be noted that the spot was moved by realigning the laser beam on the fixed sample, which lead to slightly different focusing conditions and thus spot sizes and peak intensities. However, a strong influence of the peak intensity on the yield can be excluded because the spot is smaller for the positions 1 and 2 ($A_1 = 0.73 \text{ mm}^2$ and $A_2 = 0.60 \text{ mm}^2$) than for position 3 ($A_3 = 0.90 \text{ mm}^2$). A similar position-dependence as in our results was measured by Aeschlimann *et al.*, who suggest an explanation based on (localized) surface-plasmons [Aeschlimann95]. However, this mechanism is still controversially discussed [Shalaev96, Banfi03] and even the influence of the surface roughness is not yet clear [Rhie03, Banfi03].

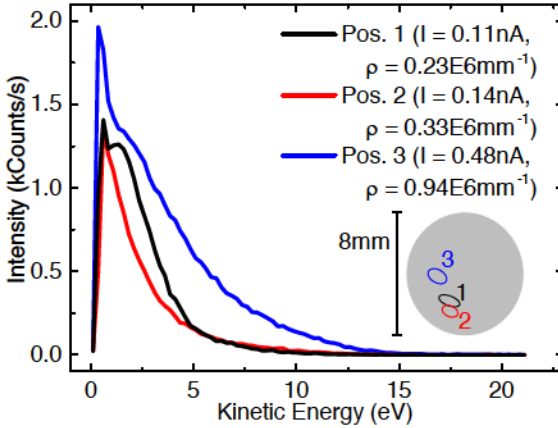


Figure 6.4: Dependence of the NIR pump-induced photoelectron spectrum on the position of the laser spot. The measurements were performed with s-polarized light on thin Ni films (see text/footnote) grown on Cu(001). A pulse duration of 131 fs was used and the laser fluence was 34 mJ/cm^2 , 42 mJ/cm^2 and 28 mJ/cm^2 at position 1, 2 and 3, respectively. The different positions of the laser spot on the round sample with a diameter of 8 mm are indicated in the inset.

Moreover, the energy distribution curves (EDCs) plotted in Fig. 6.4 show that not only the yield of photoelectrons but also the shape of the energy spectrum depends on the sample position. In general, the (linear) photoelectron density ρ given in the legend of the plot is high enough to expect a significant acceleration of photoelectrons by VSC (see Sec. 5.3). However, this explanation can only be employed for the EDC measured at position 3. The enhancement of fast photoelectrons at position 1 compared to position 2 has probably a different origin because ρ and thus the shifts due to VSC effects are larger for the latter measurement. Another possible explanation for the different shapes of the spectra at position 1 and 2 are the slightly

⁷The characterization measurements of the position- and light polarization-dependence were performed on Ni films. However, the strong position-dependence was also consistently observed for the Co films. Moreover, the findings for the polarization-dependence should be generally valid because the explanation is not based on material-specific properties.

6.2. PUMP-INDUCED PHOTOELECTRONS & RESULTING SPACE-CHARGE CONTRIBUTION

different emission angles of the photoelectrons that are detected by the spectrometer.

In order to further investigate the influence of the electric field on the photoelectrons emitted by the NIR pump-beam, the polarization of the light at the positions 2 and 3 was rotated. The resulting counts integrated over the full spectra and the sample currents, which are both related to the photoelectron yield, are summarized in Fig. 6.5. For position 2 and 3, the counts as well as the currents show a strong dependence on the direction of the light polarization vector. They change periodically and follow almost perfectly the 180° periodicity of the light polarization. The measurements show that the photoelectron yield has a maximum for p-polarized and a minimum for s-polarized light. This can be explained by the difference in light absorption for the incident light angle of 45° in our geometry [Damascelli96].

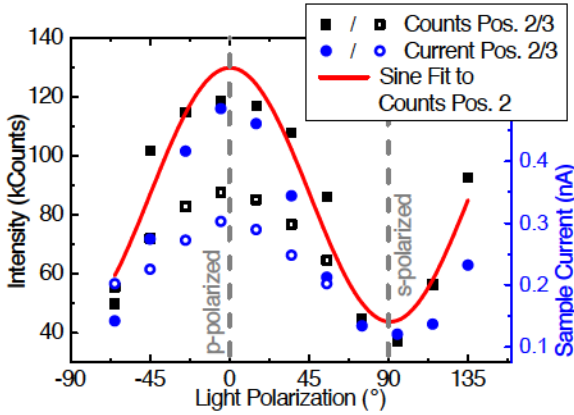


Figure 6.5: Dependence of the pump-induced photoelectron intensity and sample current on the light polarization. The intensity is determined as the sum of counts over the full energy spectrum (see Fig. 6.6). Measurements were performed at position 2 and 3.

The data shown in Fig. 6.5 reveals that the intensity variation due to the light polarization change is larger at position 2 than at position 3. Moreover, the shape of the spectra recorded at position 3 does not show a significant influence of the variation of the light polarization (see left side of Fig. 6.6). In contrast, at position 2 the energy distribution of the pump-induced photoelectrons depends strongly on the light polarization (right side of Fig. 6.6). Here, due to the large variation of created photoelectrons, the linear photoelectron density ρ varies over almost one order of magnitude. Since the amount of high energy photoelectrons changes similarly, VSC effects are again a possible explanation.

The next parameter that was varied is the duration of the pump-pulses using the

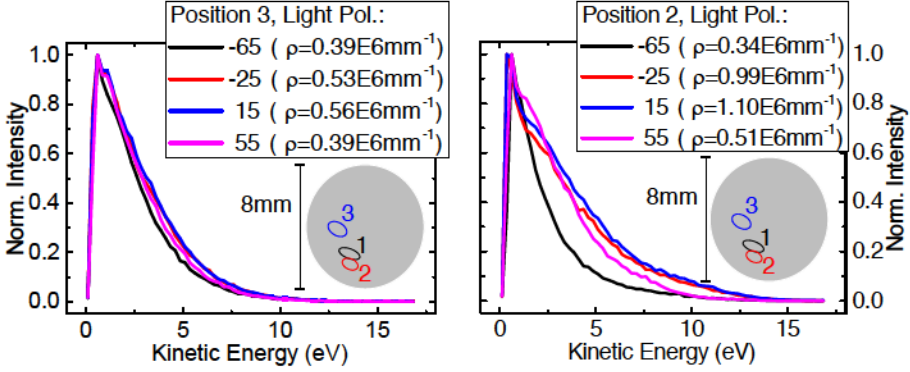


Figure 6.6: Normalized EDCs for different light polarizations at position 3 (left) and 2 (right). The measurements were performed under the same experimental conditions as in Fig. 6.4.

compressor in the laser amplifier system⁸. As shown on the left side of Fig. 6.7, the integrated electron counts decrease with increasing pulse duration as expected for multiphoton photoemission. However, in general an exponential decrease is characteristic for such a process [Musumeci10]. The deviation from the expected behavior can be explained by a suppression of the emission of additional photoelectrons for high yields by the Coulomb repulsion of the already existing photoelectron cloud [Riffe93]. In general, an influence of VSC effects is also supported by the shape of the energy distribution of the photoelectrons (see right side of Fig. 6.7), because the number of fast photoelectrons is scaling with the total number of electrons. The data supports our assumption that (propagating) surface-plasmons do not play a major role for our measurements because this would result in an increased amount of fast photoelectrons for long pulses [Kuperszttych01]. In pump-probe experiments, we adjusted the duration of the pump-pulses by passing them through additional pieces of glass. This avoids changes in the duration of the probe-pulses, which would occur for an adjustment using the compressor of the laser amplifier system.

Finally, the power of the pump-beam was varied in order to measure the resulting effect on the photoelectron spectrum. The left side of Fig. 6.8 shows the normalized electron counts at a kinetic energy of $E_{kin} = 15.1\text{eV}$ (open blue circles) as well as integrated over the full spectrum (filled black squares), both plotted as a function of the laser fluence. Moreover, the corresponding EDCs are presented on the right side. For a pure multiphoton process, an increase of the integrated counts with the laser intensity to the power of the number of involved photons is expected [Yen80]. Furthermore, the exponent can be even higher in the case of a thermally assisted

⁸All values given for the pulse duration have been measured at the same reference position before the vacuum chamber. Because a lens and a borosilicate vacuum window are placed between this position and the sample, the actual duration at the sample can differ by a few femtoseconds.

6.2. PUMP-INDUCED PHOTOELECTRONS & RESULTING SPACE-CHARGE CONTRIBUTION

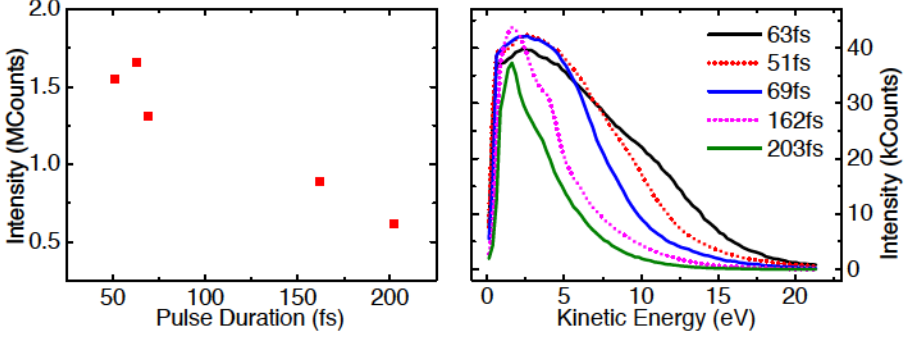


Figure 6.7: Left: Dependence of the pump-induced photoemission intensity on the pulse duration. The total number of counts in the spectra was added up. All measurements were performed on thin Co(001) films.

mechanism [Damascelli96]. Such an exponential increase is not observed. Similar to the pulse length dependence, the almost linear behavior might be related to an increasing suppression of photoelectron emission by VSC effects for denser electron clouds [Riffe93]. The non-linear behavior of the electron counts at $E_{kin} = 15.1$ eV is caused by a shift of the electron distribution towards higher kinetic energies. This interpretation is supported by the measured spectra.

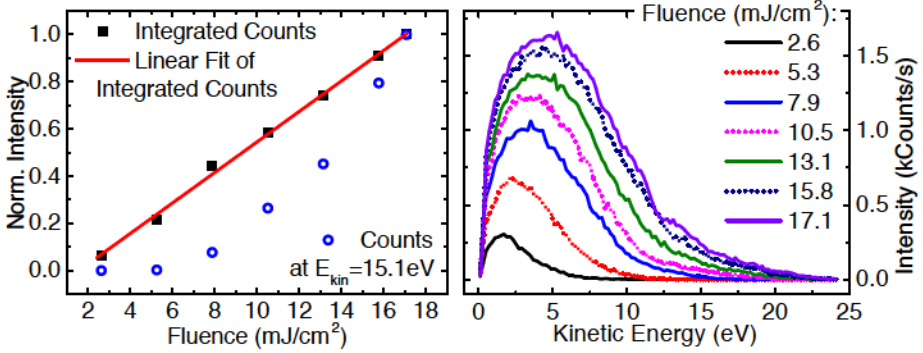


Figure 6.8: Dependence of the pump-induced photoemission intensity on the laser fluence. The pump-pulses were s-polarized and had a duration of 176 fs. Thin Co(001) films were used as the sample and the spot size was $A = 1.27 \text{ mm}^2$.

In conclusion, we found that several parameters determine the properties of the photoelectrons excited by the NIR pump-pulses. Our results show that the photoelectron yield as well as their energy distribution strongly vary over the parameter range that we studied. In order to decrease the amount of photoelectrons generated

by the NIR beam, a careful adjustment of the pump-pulse duration to the desired temporal resolution is necessary. Moreover, our experiments show a clear dependence of the photoelectron yield on the spot position. Scanning over the sample to find a suited spot is therefore essential before starting time-resolved measurements.

6.2.2 Vacuum Space-Charge Contribution from Pump-Induced Photoelectrons

After characterizing the yield and the energy distribution of the pump-induced photoelectrons for different conditions, the following subsection will describe the effect of these electrons on the results in pump-probe measurements⁹. In particular, the pump-induced electron cloud interacts via Coulomb repulsion with the photoelectrons excited by the XUV probe-pulse. This results in an additional VSC contribution, which depends on the delay between both pulses and thus the electron clouds.

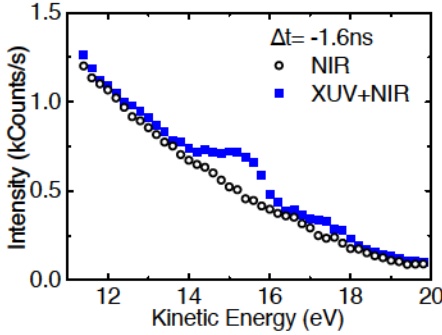


Figure 6.9: Subtraction of the pump-induced photoemission background. The black open circles represent the electron counts from only the NIR beam, and the blue filled squares the sum of counts from the NIR and the XUV light. The kinetic energy range is in the vicinity of the $3d$ Cu(001) peak. (Adapted from [Plötzing16] with permission of AIP Publishing. The CC license does not apply.)

In order to investigate the interaction between the two electron clouds, photoemission spectra from the $3d$ valence bands of Cu(001) were recorded in normal emission. For the excitation, the HHG source in BDM was used at a repetition rate of 5 kHz, while the NIR pump-beam emitted additional photoelectrons from the probed sample position. The measurement position was not optimized for a small photoemission yield from the NIR pulses and the pump fluence was adjusted to $\approx 8 \text{ mJ/cm}^2$ resulting in a ≈ 20 times higher electron yield from the NIR pump- than from the XUV probe-beam. In this test situation, the influence of the pump-induced electron cloud on the probe-induced electrons has been significant, whereas we assume that the opposite effect is negligible. By subtracting the results of subsequent measurements with only the NIR pump-beam and both the XUV probe- and the NIR pump-beam impinging on the sample, the counts from electrons excited by the XUV light were extracted. Typical spectra for both measurements are shown in Fig. 6.9.

⁹Note that parts of this subsection are also subject of [Plötzing16].

6.2. PUMP-INDUCED PHOTOELECTRONS & RESULTING SPACE-CHARGE CONTRIBUTION

As described in Sec. 5.3, VSC effects induce an energy shift of spectral features in photoemission. In order to study the dependence of this shift on the delay between both pulses, the relative arrival time has been varied. The left side of Fig. 6.10 shows the energy distribution of the electrons created from the Cu(001) 3d bands by the XUV light for three chosen characteristic delays. In addition, a reference spectrum of the peak without NIR pump-beam is plotted (black filled triangles).

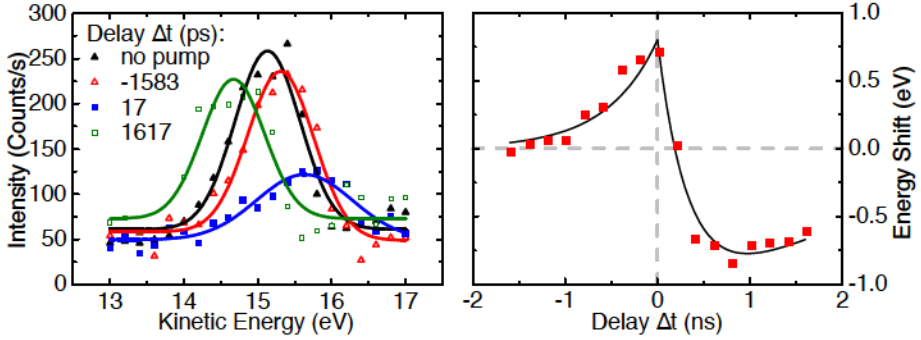


Figure 6.10: Left: Normal emission spectra of the Cu(001) valence bands measured with XUV pulses in the presence of NIR pulses. The background counts from the NIR beam were subtracted (see Fig. 6.9) and the delay Δt between the pulses was varied for the different measurements. The lines represent Gaussian peak function fits. (Adapted from [Plötzting16] with permission of AIP Publishing. The CC license does not apply.) Right: Delay-dependence of the peak shift. The peak position was extracted from spectra as shown on the left side by Gaussian peak function fits. The line serves as a guide to the eye.

For negative delays, meaning that the XUV probe-pulses arrive at the sample earlier than the NIR pump-pulses, the peak is shifted towards higher kinetic energies (red open triangles). An even stronger shift is observed close to the ZD and even for small positive delays (blue filled squares). For higher positive delays, however, the peak is shifted towards negative kinetic energies (green open squares).

From Gaussian peak function fits to EDCs measured over a broader delay range, a detailed delay-dependence of the energetic position of the 3d peak can be extracted. The results are plotted on the right side of Fig. 6.10. Up to now, studies of the influence of pump-induced photoelectrons on photoemission spectra via VSC in a pump-probe scheme are only rarely reported in literature. The experiments that are closest to our conditions were performed by Oloff *et al.* using free-electron laser (FEL) radiation [Oloff14]. For negative delays, the authors observe a behavior, which qualitatively agrees with our data. However, for positive delays no negative shifts are present. In contrast, the reported measurements show a similar decay as for the negative delays but with a different characteristic constant. Oloff *et al.* were

able to describe their results with a model based on the idea that the pump-induced electron cloud can be simulated by the electrostatic potential of a two-dimensional disk of charges. The latter is given, on the symmetry axis at a distance z , by [Siwick02]

$$V(z) = \frac{e}{\pi\epsilon_0} \cdot \frac{N_{pulse}}{d_{FWHM}^2} \cdot \left(\sqrt{z^2 + d_{FWHM}^2} - z \right), \quad (6.2)$$

where N_{pulse} is the number of photoelectrons generated per laser pulse, d_{FWHM} is the diameter of the photoelectron disk and the constants e and ϵ_0 have their standard meaning as the elementary charge and the vacuum permittivity, respectively. The model used by Oloff *et al.* assumes that the probe-induced electrons are created within this potential and reach the spectrometer in field-free space. In their case, the latter assumption is justified because the detected (probe-induced) photoelectrons are significantly faster (several keV) than the pump-induced electron cloud. Due to energy conservation, the energy gain of the probe-induced electrons is then given by their potential energy when both clouds are simultaneously present for the first time. In general, the potential energy of the probe-induced electrons at this time depends on their distance to the pump-induced electron cloud. For negative delays, the probe-induced electrons are generated first and travel a part of the distance to the spectrometer before the pump-induced electrons are emitted. For positive delays, the situation is opposite. Because of the different kinetic energies and thus velocities of the pump- and probe-induced electrons, this results in different distances at the first simultaneous appearance of both clouds for positive and negative delays. Therefore, the characteristic constants of the decays are different.

In contrast to these findings, the assumption that the probe-induced electrons reach the spectrometer far in front of the pump-induced electron cloud is not fulfilled in our experiments since here both clouds have similar kinetic energies. Consequently, the potential energy of the probe-induced electrons at the time when they reach the spectrometer has to be additionally considered. For this purpose, we performed simulations with a simple model that is also based on the potential in Eq. 6.2. Here, the positions of the pump-induced electron cloud and one probe electron are calculated for subsequent time steps using a fixed delay between the arrival time of both light pulses. The pump-induced photoelectron cloud is modeled as several two-dimensional disks created at the arrival of the pump-pulse on the sample and having the size of the laser spot. Each disk propagates with a different kinetic energy and consists of an amount of charges representing in total a Gaussian energy distribution matching the total number of electrons extracted from the sample current ($I = 0.9$ nA). The shape of the distribution ($E_0 = 5$ eV and $FWHM \approx 16.5$ eV) is motivated by the results shown in Fig. 6.7. All internal interactions in the pump-induced electron cloud were neglected. At the arrival of the XUV beam, the probe electron is created with an initial kinetic energy of $E_{HHG} = 15$ eV.

At the time when both pulses have arrived at the sample, the total energy of the

6.2. PUMP-INDUCED PHOTOELECTRONS & RESULTING SPACE-CHARGE CONTRIBUTION

probe electron is calculated by the sum of its original kinetic energy and its energy in the potential of the pump-induced disks. For the following time step, the new positions of the probe electron as well as the pump-induced electron disks are calculated. Afterwards, the new potential energy of the probe electron in the field of the pump-induced electron disks is determined using these positions. The difference of the total energy and this potential energy defines then the new kinetic energy of the probe electron, which is again used to calculate its position for the next time step. This procedure is repeated until the probe electron has traveled the distance to the spectrometer entrance ($l = 2.5$ cm). Finally, the difference of the kinetic energy compared to the undisturbed case is determined at the spectrometer entrance position. The simulation can be performed for several delays between the pump- and probe-pulse reproducing the measurements plotted on the right side of Fig. 6.10. The corresponding MATLAB source code is presented in the Appendix.

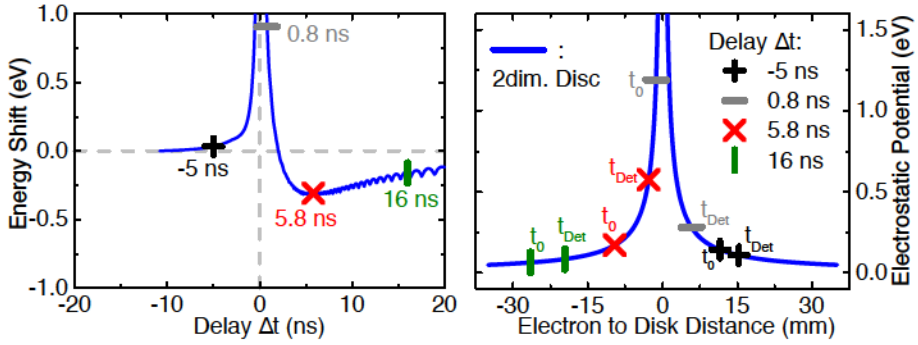


Figure 6.11: Left: Result of a simulation of the energy shift of the Cu(001) valence bands due to vacuum space-charge generated by pump-induced photoelectrons. The parameters of the simulation correspond to the experimental situation for the data shown in Fig. 6.10. The oscillations of the curve visible for positive delays are generated by the discrete kinetic energy values of the disks used to describe the pump-induced electron cloud. Details of the simulation are described in the text. Right: Electrostatic potential of a two-dimensional disk. For the four delays that are marked on the left side, the distance of the probe electron from the weighted mean of the pump-induced electron cloud is marked for the first time when both clouds coexist (t_0) and the time when the probe electron arrives at the distance of the spectrometer entrance (t_{Det}). (Adapted from [Plötzing16] with permission of AIP Publishing. The CC license does not apply.)

The energy shifts calculated using the values for I , E_0 , FWHM, E_{HHG} , and l given in the text above are plotted on the left side of Fig. 6.11. The results show that the simulation qualitatively describes our experimental findings: the increase of the peak shift from high negative delays to the ZD ($\Delta t = 0$), the fast drop and change of sign of the shift for $\Delta t > 0$ and the slow convergence towards the undisturbed case for increasing positive delays are reproduced.

For a more detailed interpretation of the result, the situation at the four delays marked in the plot and representing typical experimental situations will be described in the following. For this purpose, the potential of a single disk carrying all pump-induced electrons¹⁰ is plotted on the right side of Fig. 6.11. This potential represents the interaction of the pump-induced electron cloud with the probe electron. The distance between the probe electron and this single, pump-induced disk¹¹ is marked for the four representative delays at two situations: (1) at the first time when both pulses have arrived at the sample and (2) at the time when the probe electron reaches the distance of the spectrometer entrance. In addition, Fig. 6.12 shows the traveled distance from the sample as a function of time for the probe electron (black line), an undisturbed reference electron (green squares) and selected disks of the pump-induced electron cloud (separation: 2 eV, red lines) for the delays discussed.

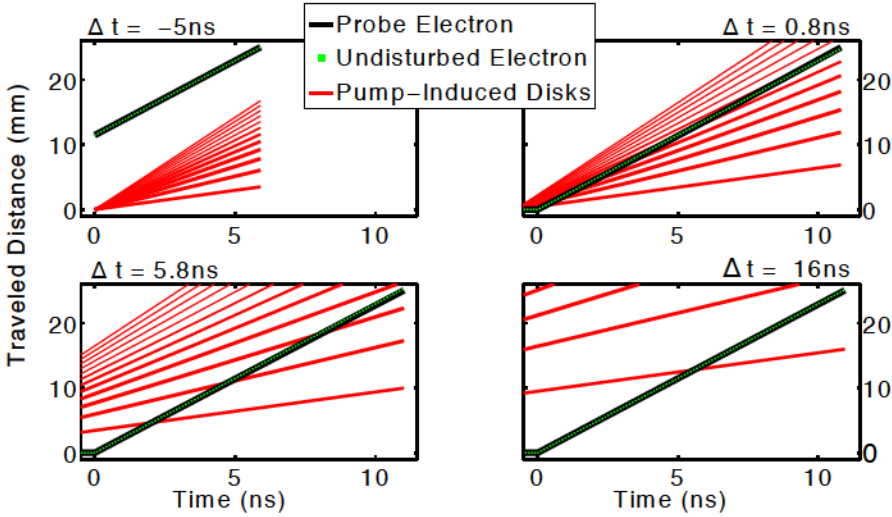


Figure 6.12: Propagation of electrons in the simulation. The time $t = 0$ marks the situation when the second of the either pump- (for $\Delta t < 0$) or probe-pulse (for $\Delta t > 0$) arrives at the sample. For the pump-induced disks, the line thickness of the plots represents the amount of electrons in the corresponding disk. The delays for the situations shown here are marked in the plots of Fig. 6.11.

¹⁰The separation into several, split disks with different kinetic energies as used in the simulation is not considered in this illustration for the sake of simplicity.

¹¹The trajectory of the probe electron is calculated using the simulation with the full kinetic energy distribution of the pump-induced electron cloud. The values then represent the distance of the probe electron to an electron disk propagating with a kinetic energy determined by the weighted mean over the pump-induced electron cloud.

6.2. PUMP-INDUCED PHOTOELECTRONS & RESULTING SPACE-CHARGE CONTRIBUTION

For negative delays (see black crosses in Fig. 6.11), the probe electron has already propagated away from the sample at the time when the pump-pulse arrives there (see top left of Fig. 6.12). Since most of the pump-induced electrons are slower than the probe electron, it stays in front and even increases the distance to the majority of the pump-induced cloud. Therefore, the potential energy is smaller at the position of the spectrometer entrance than at t_0 and the energy shift is positive (meaning towards higher kinetic energies). This situation describes all negative delays. However, the energy shift is increasing for decreasing Δt because smaller delays result in a shorter distance that the probe electron can propagate from the sample before the arrival of the pump-pulse. For small positive delays (gray horizontal lines in Fig. 6.11), the situation is still similar. The main difference is now that the probe electron is generated behind the pump-induced cloud (top right side of Fig. 6.12). Nevertheless, the probe electron is still able to overtake a large number of the electrons in the pump-induced cloud and reaches the spectrometer entrance significantly in front of most of them with only a small influence of the corresponding field. This leads to positive shifts of the energy of the probe electron. However, for larger positive delays the distance of the pump-induced cloud and thus the potential energy of the probe electron at its generation is decreasing. In parallel, the interaction of the probe electron with the pump-induced electrons at t_{Det} is increasing, because the probe electron arrives at the spectrometer entrance position with the majority of the cloud (bottom left side of Fig. 6.12). At some point, the potential energy of the probe electron at t_{Det} becomes stronger than its potential energy at t_0 and the probe electron is in total decelerated (red tilted crosses in Fig. 6.11). With further increasing positive delays, the probe electron is not able to catch up with the majority of the pump-induced electrons anymore and stays behind most of the cloud (bottom right side of Fig. 6.12). Then, the repulsive force is still slowing down the probe electron, but due to the higher distances the interaction and thus the negative shift is smaller (green vertical lines in Fig. 6.11).

Altogether, the simulation allows a qualitative interpretation of our experimental findings. Nevertheless, quantitatively the results of the simulation and the experiment differ. First, the model predicts stronger positive peak shifts around $\Delta t = 0$. A possible explanation for this discrepancy are positive mirror-charges created by the pump-induced photoelectrons in the sample, which are neglected in the simulation (see also Sec. 5.3). For the first tens of femtoseconds after the creation of the pump-induced electron cloud [Campillo00], the sample surface layers are positively charged due to the emission of the photoelectrons. On longer time scales, a screening of the electrostatic field of the pump-induced electron cloud in the metallic sample is present. Both effects generate an additional potential that decelerates the probe electron in the vicinity of the sample. In addition, the simulated negative shifts are smaller than the measured values. The most important difference is, however, that the characteristic constants of the decays for both negative and positive delays are significantly overestimated by the simulation as indicated by the time scales

of the plots in Fig. 6.10 and Fig. 6.11, which differ by a factor of 10. In general, the simulation is very simplified and several aspects are not yet properly taken into account. As mentioned earlier, all interactions within the pump-induced electron cloud as well as the influence of the probe-induced electrons on the pump-induced cloud are neglected. Furthermore, in the simulation all electrons are restricted to a propagation along the normal emission direction, which is again a simplification of the real situation. Other properties that are neglected, like the inner structure of the photoelectron clouds, are in particular important during the overtaking process. Finally, the interaction of the photoelectrons on their way inside the spectrometer is not taken into account. An advanced simulation considering these effects may be able to explain the measurement results also quantitatively.

Besides explaining the experimental results, the model that is used can suggest critical parameters for upcoming studies. As shown in Fig. 6.13, the influence of the pump-induced photoelectrons on the measurements via VSC, and especially the position of the change of sign, depends strongly on the distance between the sample and the spectrometer entrance. It has to be noted that this distance was only roughly estimated up to now and has to be measured more precisely for upcoming measurements. In addition, this quantity can be varied in the future in order to verify our model. Moreover, the shape of the delay-dependence is strongly influenced by the spectrum of the pump-induced electron cloud. As shown in Sec. 6.2.1, the latter can significantly vary, *e.g.*, for different sample positions or fluences. The full energy distribution of these photoelectrons has to be measured for the particular conditions in order to allow a proper simulation of the experiment situation.

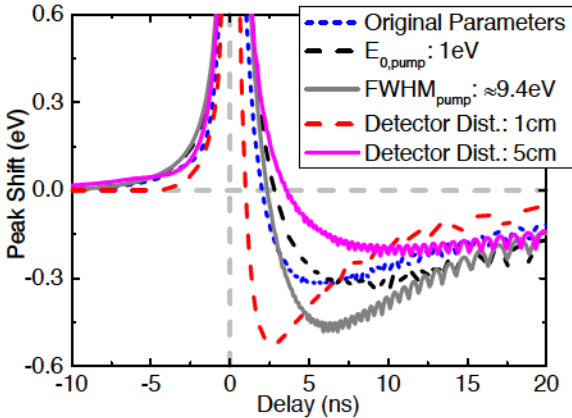


Figure 6.13: Results of the simulation of vacuum space-charge effects caused by pump-induced electrons for varying parameters. The dashed black and solid gray curve illustrate the influence of a change of the Gaussian energy distribution of the pump-induced photoelectrons by changing the central energy and the width, respectively. For the red dashed and magenta solid curve, the distance that the probe electron propagates was changed. For the blue dashed line, the same parameters as on the left side of Fig. 6.11 were used.

As our results show, the pump-induced VSC effects occur on a pico- to nanosecond time scale. Although they can influence the investigation of magnetization dynam-

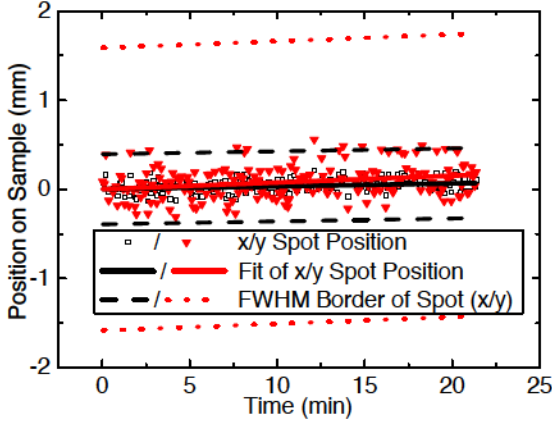


Figure 6.14: Drift of the HHG spot with time. The data was extracted from pictures similar to Fig. 6.3 by fitting a rotated two-dimensional Gaussian peak function (see Sec. 5.3). The black open squares and red filled triangles illustrate the extracted x- and y-coordinates of the peak positions, respectively. Moreover, the thick lines represent corresponding linear fits to these values and the dashed/dotted lines the average FWHM of the spot.

ics, the effects can therefore be treated as a constant shift for processes happening within several hundreds of femtoseconds like electron-dynamics or ultrafast demagnetization.

6.3 Temporal Stability of the Beam Spot Position

For measurements of the ultrafast magnetization dynamics in a pump-probe scheme, the stability of the beam position is a crucial parameter because the overlap between pump- and probe-beam needs to be stable over the full acquisition time. Therefore, several measurements to identify the stability conditions in our setup were performed. First, the temporal drift of the spot of the XUV light created with the HHG source in BDM was monitored (see Fig. 6.14). From a linear fit to the beam position, a movement of $3.3 \mu\text{m}/\text{min}$ in x- and $7.6 \mu\text{m}/\text{min}$ in y-direction can be determined. Especially for the x-position, this leads to a total drift that exceeds the spot size of $FWHM_x = 0.39 \text{ mm}$ within the typical acquisition time of a time-resolved measurement lasting over several hours and can thus lead to a loss of the spatial overlap between pump- and probe-beam. This effect is even more relevant because in ultrafast time-resolved measurements the spot size is ideally reduced to $\approx 100 \mu\text{m}$ in order to minimize the creation of pump-induced photoelectrons.

Another property of our HHG source is that the photon flux drops due to a change of the pointing of the driving laser beam. This is mainly related to small deviations of the laboratory conditions even though the laser system and the HHG source are housed in a temperature-stabilized box. The difference in the laser pointing then leads to a reduced coupling of the beam into the Ar-filled waveguide and the source has to be readjusted. In order to investigate the influence of the readjustments, the

position and the drift of the 390 nm beam¹² were monitored for several consecutive alignments of the HHG source. The results are shown in Fig. 6.15. They clearly show that an offset of several 100 μm can be induced by the realignment since the position of the capillary and thus the light source imaged by the optics in the beamline changes. In addition, the strength of the drift is changing for the different alignments by two orders of magnitude and is not even always following a linear behavior.

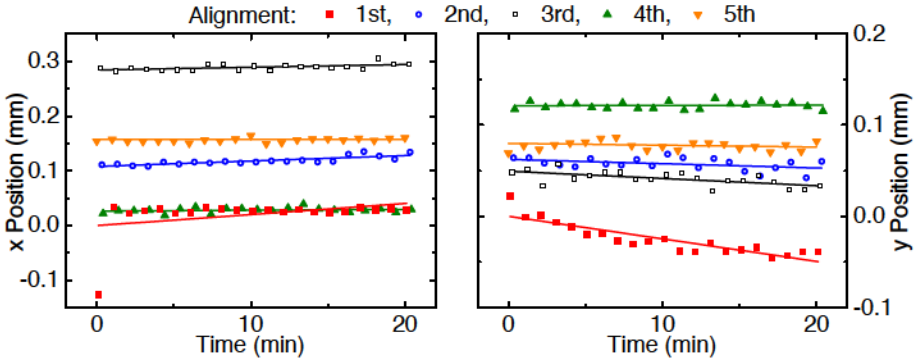


Figure 6.15: Position of the driving beam after changing the alignment of the HHG source and its drift with time. The beam position was determined as in Fig. 6.14, but using the blue driving laser beam. On the left side, the x-component of the coordinates is shown, whereas the right side illustrates the y-component.

Altogether, the pump-probe overlap has to be realigned using fluorescent material after each readjustment of the HHG source. Moreover, the time period which provides stable conditions can not be predicted because of the varying drift of the pointing of the laser light. Therefore, pump-probe experiments were only infrequently possible with our setup, especially for measurements that need long acquisition times.

However, this limitation can be addressed by actively compensating long-term drifts of the laser [Emmerich15]. For this purpose, an active beam stabilization was introduced in our setup within the last months [von Witzleben15]. It consists of two piezo-driven actuators to steer the laser beam position as well as its pointing and two CCD cameras that record the beam afterwards. A feedback loop between the cameras and the actuators is then used to compensate beam movements.

The left side of Fig. 6.16 shows the change of the (horizontal) position of the laser beam with time if the beam stabilization is turned off and if it is turned on. Without active stabilization (black line), the beam shows strong drifts on a time scale of sev-

¹²It is assumed that this beam propagates in a similar way as the XUV light and is also sensitive to the waveguide position.

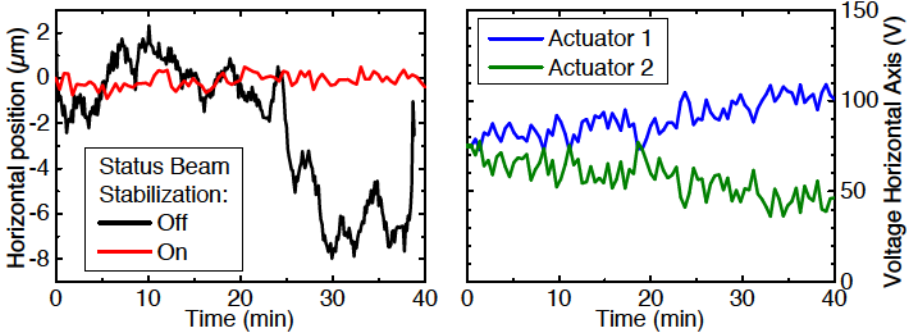


Figure 6.16: Left: Horizontal displacement of the laser beam as a function of time with and without active beam stabilization. The data was extracted from one of the CCD cameras that monitor the beam for the stabilizatoin. The values are smoothened over a range of 10 data points to reduce noise due to short-term fluctuations. Note that the black line has a higher density of data points. Right: Voltage applied to the piezo-driven actuators that compensate the beam movements. The data corresponds to the stabilized situation shown on the left side of the figure. (results are in both cases taken from [von Witzleben15])

eral minutes¹³. In contrast, the position of the laser beam is only slightly fluctuating around the original position if it is stabilized (red line). Moreover, the values for the voltages applied to the piezo-driven actuators are significantly changing during this time (see right side of Fig. 6.16), which proves that the incoming laser beam had changed its pointing and position, but that the changes were compensated. A detailed description and testing of the beam stabilization as well as further information about the presented characterization can be found in [von Witzleben15].

¹³The scale of the y-axis represents the position on one of the beam stabilization CCD camera and can not be directly compared to the beam position on the sample, which is shown in Fig. 6.14 and Fig. 6.15.

7 Photoemission Studies of the Electron- and Spin-Dynamics in Thin Co Films During Ultrafast Demagnetization

As discussed at the end of the last section (see Sec. 6.3), high requirements for the temporal stability of the laser pointing and the high-order harmonic generation (HHG) source have to be satisfied for pump-probe measurements with long acquisition times. To ensure the best possible HHG beam stability, we joined our spin-resolved photoelectron detection system (cylindrical sector analyzer (CSA) spectrometer and FERRUM spin detector) with an experimental setup that is well-established for time- and angle-resolved photoemission at the University of Kaiserslautern (AG Aeschlimann) [Mathias07, Eich14]. This enabled an efficient progress of the project, which was in addition substantially accelerated due to the combination of the experience with time-resolved photoemission using the HHG source of the group in Kaiserslautern and our knowledge about spin-resolved experiments with pulsed extreme ultraviolet (XUV) light. Moreover, the joint experiment allowed a direct comparison of angle-resolved studies of the electron-dynamics using the already installed hemispherical analyzer (Phoibos 150, SPECS Surface Nano Analysis GmbH) with results obtained with the spin-resolved detection scheme on the same samples. A sketch of the resulting setup is shown in Fig. 7.1.

The HHG source¹ used for the measurements, which will be presented in the following sections, is similar to the blue-driven mode (BDM) described in Sec. 3.2. It is based on a regenerative laser amplifier system (Wyvern, KMLabs) that was operated at a repetition rate of 10 kHz at a central wavelength of $\lambda = 790$ nm. Furthermore, the laser pointing has been actively stabilized to be constant at the entrance of the capillary waveguide [Emmerich15]. Ten percent of the fundamental light intensity was separated for the pump-beam and the pulse duration in this part

¹Further information can be found in, *e.g.*, [Eich14, Emmerich15].

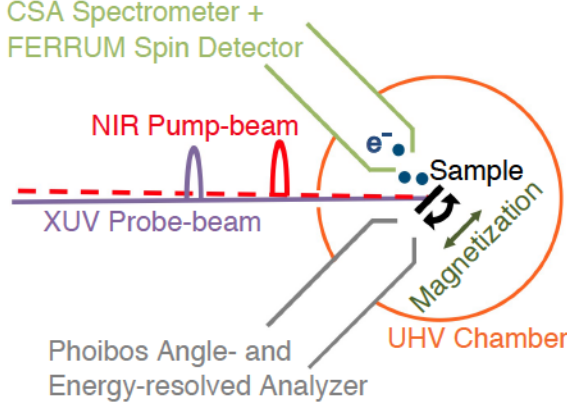


Figure 7.1: Sketch of the experimental setup for the ultrafast demagnetization measurements. A pump-probe technique is used to allow for sub-picosecond temporal resolution. Depending on the sample angle, a detection system enabling either angle- or spin-resolved photoelectron spectroscopy can be used.

was adjusted to $t^2 \approx 74$ fs at the sample position using the dispersion in a calcite crystal in order to minimize photoemission induced by the near-infrared (NIR) pump-pulses (see Sec. 6.2). The remaining light was frequency-doubled leading to a pulse intensity of ≈ 0.3 mJ/cm² at $\lambda = 395$ nm and later used for triggering the HHG process. Furthermore, the XUV photon flux at the sample was increased by using Kr gas for the energy-upconversion and by coating the SiO₂ mirror in the beamline with B₄C resulting in a higher reflectivity. The spot diameter³ of the 395 nm laser beam at the sample position, which gives an upper limit for the size of the XUV beam, was determined using a knife-edge method to be $FWHM_x = 207$ μ m and $FWHM_y = 225$ μ m in x- and y-direction, respectively. Similarly, $FWHM_x = 245$ μ m and $FWHM_y = 440$ μ m was obtained for the size of the NIR pump-beam.

As shown in Fig. 7.1, the entrance lenses of the photoelectron spectrometers were mounted at an angle of $\pm 45^\circ$ with respect to the direction of the incoming HHG light. In contrast to the configuration described in Sec. 3.2.1, the CSA was mounted with a vertically oriented dispersive plane making the FERRUM sensitive to the out-of-plane and the horizontal in-plane direction of the sample.

The following chapter will, first, give an overview of the laser-induced electron-dynamics that we observed in Co(001) (Sec. 7.1). In the second part, the feasibility of spin-, energy- and time-resolved experiments will be demonstrated and results

²The pulse duration was determined from the autocorrelation signal of frequency-doubling in a β -BaB₂O₄ (BBO) crystal to 62 fs. Afterwards, it still passes through a lens and a vacuum window before it arrives at the sample.

³The diameter values do not consider the enlargement of the spot in x-direction due to the rotation of the sample that leads to off-normal light incidence. However, this effect is considered in the determination of the pump fluences.

allowing new insights into the spin-dynamics of Co will be presented (Sec. 7.2).

7.1 Ultrafast Electron-Dynamics Probed with Time- and Angle-Resolved Photoelectron Spectroscopy

Using the Phoibos detector, angle-resolved photoelectron spectroscopy (ARPES) maps have been recorded. A typical example is shown in Fig. 7.2, measured on a Co(001) film with p-polarized XUV pulses. Between $E_B = 0$ and $E_B = 1.5$ eV, the d -bands of Co are visible. In general, electrons from a majority $\Delta_{2\uparrow}$ -band, a minority $\Delta_{5\downarrow}$ -band and a surface resonance contribute to the peak (see Sec. 4.2). Nevertheless, the individual contributions can not be clearly separated without spin resolution.

In addition, the results show strong intensity deviations that are not symmetric with respect to $k_{\parallel} = 0$, for example the small spot at $k_{\parallel} = -0.23 \text{ \AA}^{-1}$ and $E_B = 0.35$ eV or the region between $E_B = 1$ eV and $E_B = 3.5$ eV for $k_{\parallel} > 0.15 \text{ \AA}^{-1}$. These can be explained by inhomogeneities in the micro-channel detection plate. However, the detector imperfections have only minor relevance in the following because for the time-resolved measurements presented from now on only the difference of the signal compared to the undisturbed case (delay $\Delta t < 0$, before the pump-pulse arrives) is analyzed. This subtraction compensates most of the inhomogeneities⁴.

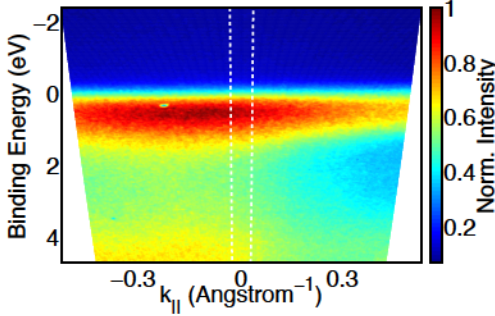


Figure 7.2: Photoemission intensity from a Co(001) film. The data is plotted against the electron binding energy and the wave vector (calculated using Eq. 2.22). $E_B = 0$ is determined from the Fermi level in a fitted Fermi-Dirac distribution. The white, dashed lines mark the area that is integrated for the determination of the zero delay using the laser-assisted photoelectric effect (see Fig. 7.3).

The count rate in measurements employing the Phoibos analyzer allows a live observation of both the broadening and shift of the $3d$ bands induced by vacuum space-charge (VSC) (see Sec. 5.3). These effects were suppressed with a careful reduction of the XUV photon flux by decreasing the intensity of the driving laser light

⁴See the right side of Fig. 7.4, which will be discussed later, for an example of a difference ARPES map.

using an adjustable aperture. This adjustment was done prior to all measurements, including the spin-resolved studies discussed in Sec. 7.2, using the Phoibos analyzer. Moreover, the yield of photoemission from the NIR pump-beam was minimized by scanning different positions on the sample before time-resolved measurements were performed in order to decrease the background signal and influence of VSC (see Sec. 6.2).

Based on the position of the temporal overlap between the 790 nm pump-pulses and the 395 nm pulses used for driving the HHG process (see Sec. 6.1), the exact zero delay (ZD) between the NIR pump- and the XUV probe-pulses at the sample surface was determined using the laser-assisted photoelectric effect (LAPE). This effect creates sidebands of spectral features with an energy separation on the order of the photon energy of the NIR pump-beam [Miaja-Avila06]. In agreement with [Saathoff08], we observed a LAPE signal only for a p-polarized pump-beam that has a field component perpendicular to the surface. In order to determine the ZD, a scan over several pump-probe delays Δt with a pump fluence⁵ of $F \approx 12.5 \text{ mJ/cm}^2$ has been performed while recording photoemission intensity maps. The ARPES maps for each delay were then integrated over the wave vector range between the two white dashed lines in Fig. 7.2. In order to emphasize the changes induced by the pump-pulse, the average intensity of the first two time steps, which are not disturbed, is subtracted from the data for each following delay. The resulting (normalized) intensity difference is plotted on the left side of Fig. 7.3. During the time when both pulses are present, the LAPE induces a decrease of the intensity at the $3d$ bands and an increase at energies that differ by the photon energy of the NIR pump-pulse ($\Delta E \approx \pm 1.6 \text{ eV}$). The ZD is determined by the maximum of the effect, which can be extracted from the delay-dependence of the signal generated in the unoccupied region at $E_B < 0$ (see right side of Fig. 7.3).

Furthermore, the duration of the LAPE signal, $\text{FWHM} = 73 \text{ fs}$, corresponds approximately⁶ to the temporal resolution of the experiment. The transient time is of the order of the NIR pump-pulse duration which suggests that the latter limits the temporal resolution.

In general, the measurements presented above are dominated by the LAPE signal but also show a contribution from hot electrons excited by the pump-pulse. The electron dynamics can be, nevertheless, distinguished since it is not symmetric with respect to $\Delta t = 0$. In contrast, it shows a decay for positive delays that exceeds the duration of the NIR laser pulse. The excitation of electrons to $E_B < 0$ is indicated by the small difference in the background intensity for positive and negative delays

⁵All pump fluences are calculated for a situation, where the full power is absorbed within the full width at half maximum (FWHM). This results in an overestimation of the real values.

⁶The sidebands scale almost linearly with the NIR laser fluence for the case of small LAPE signals [Saathoff08]. This is fulfilled because we observe maximum heights of the sidebands below 15% of the original peak.

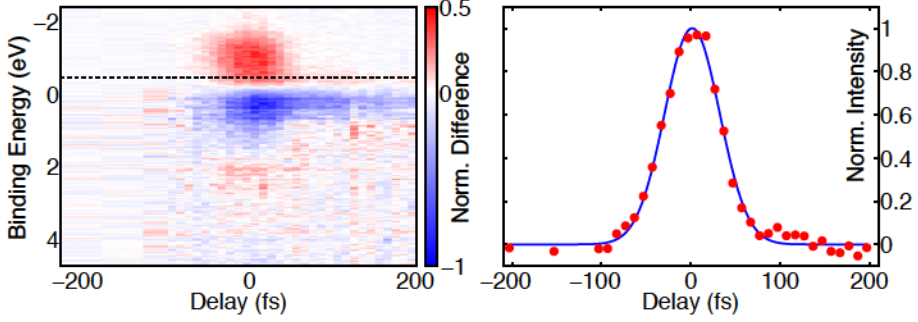


Figure 7.3: Change of the photoelectron intensity during a measurement of the laser-assisted photoelectric effect using a p-polarized pump-beam. Left: The difference map shows the k_{\parallel} -integrated (see Fig. 7.2) intensity enhancement (red) and decrease (blue) induced by the pump-pulse as a function of the electron binding energy and the delay between the pulses. Right: The red dots show the change of the intensity, integrated over the energy range above the black dashed line shown in the left plot of the figure and plotted against the delay. The blue curve is a Gaussian peak function fit.

of the cross-correlation signal plotted on the right side of Fig. 7.3. Moreover, the long-living depletion and population enhancement around $E_B = 0$ for $\Delta t > 100$ fs visible in the left plot in Fig. 7.3 suggest the dynamics of hot electrons, which is, however, significantly weaker than the signal from the LAPE at $\Delta t = 0$.

Consequently, it is useful to avoid the LAPE by using an s-polarized pump-beam for a detailed investigation of the electron dynamics. The time-dependence obtained from such a measurement using a pump fluence of $F \approx 25 \text{ mJ/cm}^2$ and p-polarized XUV light is shown on the left side of Fig. 7.4. Again, the intensity difference is plotted for each delay, but in this case calculated using the average of the first five time steps. In addition, the data is integrated over a larger wave vector space (see right side of Fig. 7.4).

The results on the left side of Fig. 7.4 show an increase of the photoemission intensity for $E_B < 0 \text{ eV}$ and a decrease at the binding energy of the $3d$ bands after the arrival of the pump-pulse. This observation can be assigned to an excitation of electrons into states that were initially empty. Afterwards, the electrons decay again on a time scale of several tens to hundreds of femtoseconds as can be seen from the reduction of the intensity enhancement for the energies above the line marking $E_B = 0 \text{ eV}$.

On the right side of Fig. 7.4, the wave vector-dependence of the excited electrons is presented. For this purpose, photoemission intensity maps of three time steps around the maximum of the effect ($\Delta t = 30, 45, 60 \text{ fs}$) are averaged. Then, the difference to the initial situation is again calculated as for the results on the left

side of Fig. 7.4. The result shows that electrons are equally excited over the full range of wave vectors, which is measured. This is in contrast to, *e.g.*, measurements on correlated materials like TiSe_2 , where electrons are excited only at certain points in the BZ [Eich14]. However, in our experiments only a small part of the Brillouin zone (BZ) was probed and the initial $3d$ states have a low curvature in the excited wave vector interval (see Fig. 7.2 and [Miyamoto08a]). This can explain the homogeneous excitation. Nevertheless, for a better understanding of the electron-dynamics, measurements over a broader wave vector range have to be performed and compared to corresponding band structure calculations. The latter need to include the final states above the Fermi level, which can be reached by the excitation with NIR pulses. Besides, information about the spin structure of the states would be useful in such a calculation in order to gain knowledge about the spin polarization of the excited electrons. Using the band structure shown in Fig. 2.3 [Chiang10], a clear identification of final states for a resonant transition with $h\nu = 1.6\text{ eV}$ is not possible.

Note that the previous arguments are based on an equilibrium band structure calculation and can thus in general only provide a limited understanding of the optically induced non-equilibrium state. Moreover, the assumption of a weak perturbation by the light, which allows an interpretation of the optical excitations within a framework based on Fermi's golden rule, is not fully justified anymore for the laser intensities in the pump-pulses (see step 1 in Sec. 2.2.1).

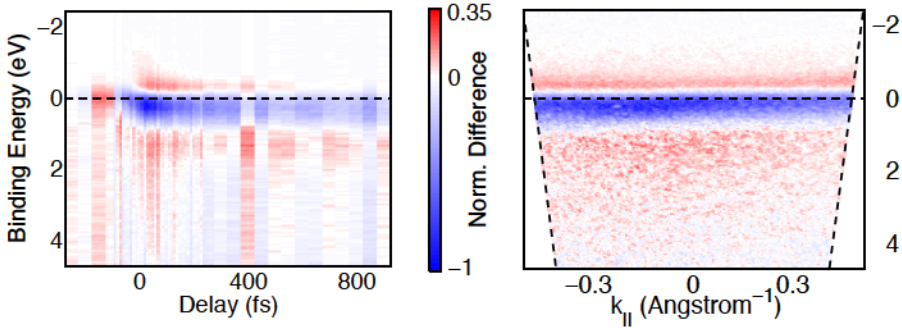


Figure 7.4: Pump-induced excitation of electrons. The plots show the enhancement (red) and depletion (blue) of the photoemission signal caused by an s-polarized pump-pulse. The black horizontal lines mark the Fermi level ($E_B = 0$) in both plots. Left: The x- and y-axis represent the temporal delay and the electron binding energy, respectively. The wave vector integration range is marked with the black tilted lines in the right plot of the figure. Right: The intensity difference shortly after the arrival of the pump-pulse is plotted as a function of the electron binding energy and wave vector.

7.2 Ultrafast Spin-Dynamics Probed with Time- and Spin-Resolved Photoelectron Spectroscopy

Based on the knowledge from the ARPES data that electrons are excited in the region around $k_{\parallel} = 0$, spin-resolved measurements were performed at this point of the BZ. Results for samples grown under the same conditions as in Sec. 7.1 are shown in Fig. 7.5, Fig. 7.6 and Fig. 7.7. The data is obtained using s-polarized light for the NIR pump-beam to avoid the LAPE and with a pump fluence of $F \approx 25 \text{ mJ/cm}^2$. The XUV light was this time also adjusted to s-polarization in order to suppress photoemission from the surface resonance resulting in only one majority and one minority spin contribution to the spectrum in the vicinity of E_F (see Sec. 5.2). We note that the acquisition time for the presented data was 16 h. In order to keep the influence of sample degradation on the results for the temporal evolution small, spectra over the full range of delays were recorded within 13 min. This cycle was repeated 76 times to increase the signal to noise ratio.

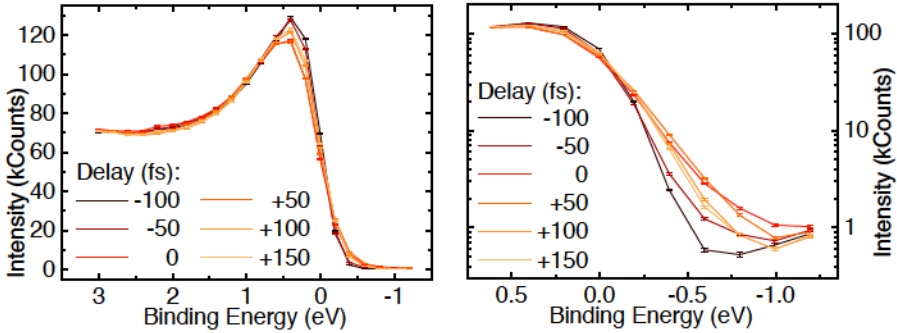


Figure 7.5: Spin-integrated photoemission intensity for different pump-probe delays. The data is measured on Co(001) and presented as a function of the electron binding energy. $E_B = 0$ corresponds again to the Fermi level determined by a fit of a Fermi-Dirac distribution to the undisturbed spectrum. Left: The plot shows the full valence band spectrum. Right: The intensity in the vicinity of $E_B = 0$ is magnified in semi-logarithmic scale.

The left side of Fig. 7.5 shows the photoelectron intensity integrated over both spin channels. As in the ARPES measurements (see left side of Fig. 7.4), an excitation of electrons by the pump-pulse from $E_B > 0$ to states above the Fermi level is observed (reduction of the intensity around $E_B = 0.4 \text{ eV}$ and increase of the intensity at $E_B < 0$ between $\Delta t = -100 \text{ fs}$ and $\Delta t = 0 \text{ fs}$). For $\Delta t > 100 \text{ fs}$, a relaxation of the excited electrons is found. The hot electrons above $E_B = 0 \text{ eV}$ can be clearly seen on the right side of Fig. 7.5, where the same data is plotted with

a logarithmically scaled y-axis. It shows that electrons are excited to $E_B \leq -1$ eV at $\Delta t = 0$ fs. Then, the electron system starts to thermalize and the shape of the spectrum around E_F approaches a broadened Fermi-Dirac distribution, which is in agreement with results published for other metals [Fann92, Rhie03]. Furthermore, the data plotted on the left side of Fig. 7.5 shows no significant intensity change over the full measured delay range for $E_B > 1$ eV.

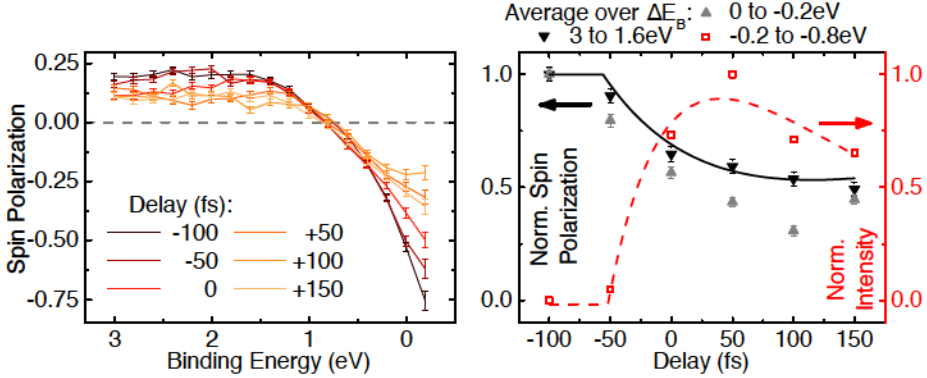


Figure 7.6: Spin polarization for different pump-probe delays. Left: The plot shows the spin polarization as a function of the electron binding energy. Right: Spin polarization values (left axis) averaged over the featureless region ($E_B > 1.6$ eV, black down-pointing triangles) and for $E_B < 0$ eV (gray up-pointing triangles) are plotted against the pump-probe delay. In addition, the spin-integrated photoelectron intensity in the region of hot electron excitation is presented (right axis, red open squares). The black solid/red dashed line is a guide to the eye (see text/footnote) for the black down-pointing triangles/red open squares that illustrates the typical temporal evolution of the quantity during an ultrafast demagnetization process.

On the left side of Fig. 7.6, the spin polarization P from the same measurement is presented, showing a clear quenching on a sub-picosecond time scale after the arrival of the pump-pulse ($\Delta t = 0$). The time evolution of P shows the typical behavior for ultrafast demagnetization, which is illustrated by the black down-pointing triangles⁷ on the right side of Fig. 7.6. These triangles represent an average value over the featureless high binding energy region. Moreover, no significant retardation is present between the start of the excitation of hot electrons (red open

⁷The curves used as guides for the eye have been calculated using

$$y = y_0 - \mathcal{H}(\Delta t - t_0) \cdot \left(A_1 \cdot \left(1 - \exp\left(\frac{\Delta t - t_0}{\tau_m}\right) \right) \cdot \exp\left(\frac{\Delta t - t_0}{\tau_E}\right) \right).$$

Here, $\mathcal{H}(x)$ represents the Heaviside step function, t_0 accounts for the beginning of the process, τ_m defines the characteristic time constant of the initial rise/decay and τ_E of the recovery.

squares) and the beginning of the reduction of P within the temporal resolution and experimental uncertainties. The energy-dependence of the spin polarization reveals that the demagnetization starts simultaneously over the full range of E_B that was measured. This is confirmed by the demagnetization curve of the P values averaged over binding energies close to E_F (gray up-pointing triangles), which however shows a higher quenching. The latter might be a consequence of the electron excitation in this region as will be discussed later. It is particularly surprising that an instantaneous quenching is observed for $E_B > 1.6 \text{ eV} = h\nu_{\text{NIR}}$, where the pump-pulse has no direct influence by single photon excitations and no change of the total intensity was observed (see Fig. 7.5). A possible explanation is the strong correlation of the electron system for this binding energy region (see Sec. 4.2) that leads, with respect to the temporal resolution, to an immediate propagation of the changes of P throughout the entire spin system.

The corresponding partial intensities for both spin directions are shown in Fig. 7.7. The data reveals a strong pump-induced drop of the intensity for the minority $\Delta_{5\downarrow}$ -band ($E_B \approx 0.4 \text{ eV}$), which is significantly lower for $\Delta t = 0$ compared to the situation before the NIR pulse arrives. In contrast, only a small decrease of the electron count rate is observed at the majority $\Delta_{2\uparrow}$ -band. A direct conclusion from this result concerning the spin-dependence of the excitation is difficult. In particular, it appears that the intensity of the hot electrons for both spin directions is not supporting this finding because it shows more majority spin electrons. These two observations are in strong contrast if a conservation of the spin is assumed during the optical excitation. A possible explanation is discussed at the end of this section.

Similar to the integrated photoemission intensity, both spin channels show a relaxation of the hot electrons for $\Delta t > 100 \text{ fs}$. A difference in the life times of the excited states for both spin directions, as observed in [Aeschlimann97], is not clearly detected in our experiment for the given signal-to-noise ratio, temporal resolution and step size of Δt . As expected from the spin polarization distribution, the partial intensity is reduced for the majority spin direction at $E_B > 1.5 \text{ eV}$, whereas it is increased for the minority spin direction in this energy range. Here, no relaxation has been observed up to $\Delta t = 150 \text{ fs}$.

As illustrated in Sec. 2.1, the Stoner-model suggests a direct relation between the magnetization M and the exchange splitting through the electron imbalance Δn (see Eq. 2.7). Besides the debate about such a behavior in static heating experiments for 3d ferromagnets (see Chap. 1), Rhie *et al.* have seen evidence for a laser-induced ultrafast quenching of the exchange splitting in Ni [Rhie03]. In addition, Müller *et al.* suggest this quenching as a mechanism that supports ultrafast demagnetization through spin-flip scattering [Mueller13].

In the probed part of the band structure of our samples, a reduction of the exchange

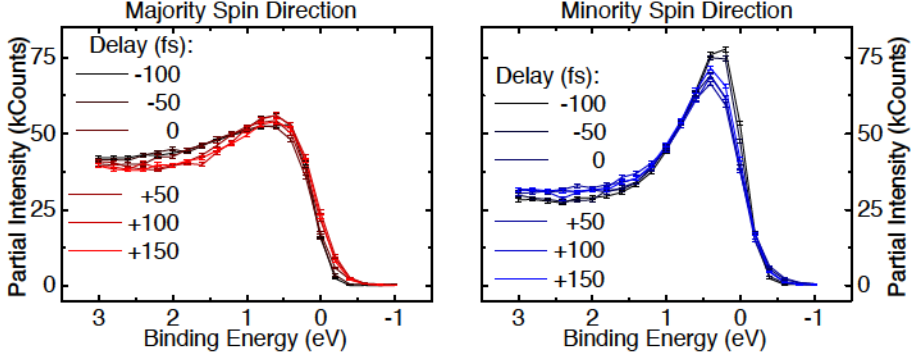


Figure 7.7: Partial intensities for different electron binding energies and pump-probe delays recorded on fct Co/Cu(001). Left: The plot shows the results for the majority spin direction. Right: Data obtained for the minority spin channel.

splitting would cause a shift of the majority $\Delta_{2\uparrow}$ -band to lower binding energies because its exchange-split counterpart is located at $E_B < 0$. At the same time, the $\Delta_{5\downarrow}$ -band would shift to higher binding energies since the corresponding majority band is located at⁸ $E_B \approx 2$ eV (see Fig. 2.3 [Chiang10]). However, in the partial intensities in Fig. 7.7 no indication of a change of the energetic position of the peaks has been detected within the (total) energy resolution of⁹ $\Delta E = 0.43 \pm 0.01$ eV. Furthermore, a shift of the peaks could create variations in the shape of the spin polarization distribution, for example leading to a different energetic position for the change of sign. This effect has not been observed either (see Fig. 7.6).

In order to test this finding, we performed measurements on hcp Co that was grown on Au(111). Here, the peak from the minority spin band is located further from $E_B = 0$ for $k_{\parallel} = 0$ and can be thus better separated from the Fermi edge making an identification of its position and shape more reliable. The resulting partial intensities are plotted in Fig. 7.8. A preliminary analysis of this data also reveals no evidence for peak shifts confirming the findings for fct Co.

Based on our observations, we conclude that the exchange splitting is not strongly quenched in Co during the ultrafast demagnetization process in the part of the BZ, which we probe.

⁸It is not observable as a peak in the results due to electron correlation effects (see Sec. 4.2).

⁹The energy resolution is determined as described in Sec. 5.2. Relative changes like peak shifts can also be detected if they are significantly smaller than this value. The measurement has been performed with $E_{pass} = 8$ eV in order to increase the count rate. Since the value for the energy resolution has approximately twice the size as for the result measured with the He lamp at $E_{pass} = 4$ eV (see Sec. 5.2), it can be deduced that ΔE is dominated by the spectrometer contribution, which scales with E_{pass} (see Eq. 3.1).

7.2. ULTRAFAST SPIN-DYNAMICS PROBED WITH TIME- AND SPIN-RESOLVED PHOTOELECTRON SPECTROSCOPY

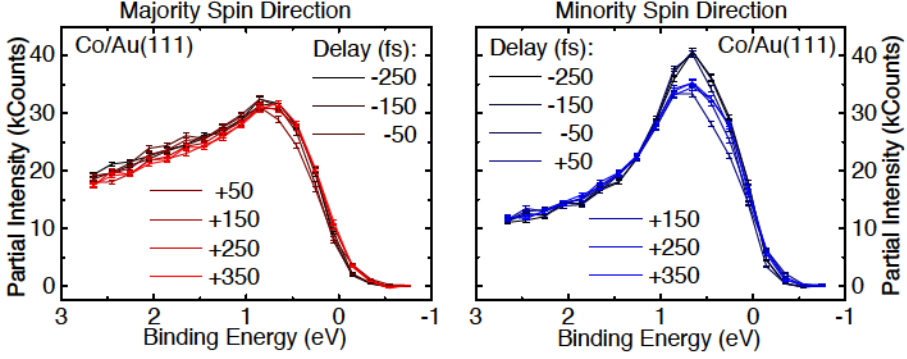


Figure 7.8: Time evolution of the energy distribution of the partial intensities in hcp Co/Au(111). The sample was excited by a NIR laser pulse at $\Delta t = 0$ and the binding energy is calculated with respect to the Fermi level (before excitation). On the left (right) side, the results for the majority (minority) spin direction are shown.

Moreover, the simultaneous and instantaneous quenching of the spin polarization over the energy range not affected by the pump-pulse suggests an interpretation based on two coexisting demagnetization mechanisms. The first mechanism changes¹⁰ the spin polarization during the phase of hot electron dynamics in the energy range around E_F . The additional quenching of P for small E_B in fct Co (see right side of Fig. 7.6) is an indication for such a contribution. In the second possible mechanism, an energy-independent fraction of the photoemission intensity is "transferred" from the dominating to the opposite spin channel at each E_B . This effect is not directly correlated with the hot electron dynamics. Evidence for such a behavior can be found in the quenching of the spin polarization and the correlated change of the partial intensities at $E_B > 1.6$ eV, where no (linear) excitation of the electrons by the pump-pulse takes place. In addition, the latter mechanism might explain the discrepancy between the partial intensities in the depleted energy region ($0 < E_B < 1$ eV) and of the hot electrons, which is observed in the data plotted in Fig. 7.7 and was also briefly discussed earlier. Since the measured intensity for $E_B < 0$ is only created by excited electrons, a projection effect would have no influence in this region. Here, the partial intensity seems to be higher for the majority spin electrons, meaning that more of them are excited. Assuming a conservation of the spin during the excitation, this means that also more majority spin electrons leave the energy range below the Fermi edge. In contrast, the minority spin channel is stronger reduced than the majority spin channel at $E_B \approx 0.4$ eV.

¹⁰The underlying physical process can be, for example, spin-flip scattering or spin-dependent transport.

This contradictory observation can be explained by an additional projection effect for $E_B > 0$ because it supports the reduction of the minority spin intensity leading to the strong drop, but at the same time counteracts the decrease of the majority spin intensity.

Further support for such a "projection" of parts of the band structure is given by static heating experiments on Co that investigate the magnetic behavior above T_C [Schneider91b]. The authors find that the magnetization is vanishing without peak shifts and that the band structure is not changing to the shape observed for $3d$ paramagnets, which does not agree with the Stoner-model. The results in [Schneider91b] are explained by a disappearance of the long-range magnetic order while small regions keep an exchange-split band structure. This can result in the observed spin mixing [Kisker84].

The interpretation suggested in the last paragraph remains, however, very preliminary on the basis of the present results and data analysis.

8 Summary & Outlook

The work presented in this thesis paves the way for a direct observation of the spin-dynamics in extended parts of the electronic band structure on femtosecond time scales using spin-resolved photoelectron spectroscopy (PES). For this purpose, an experimental setup including a highly efficient spin detector and a femtosecond-pulsed extreme ultraviolet (XUV) light source based on high-order harmonic generation (HHG) was developed and commissioned (see Chap. 3). Our photoemission setup and the *in situ* sample preparation capabilities were tested using thin Co films grown on Cu(001). The results that we achieved using static photoemission with a continuous wave (cw) light source agree with published data, which confirms the good performance of the setup (see Chap. 4). Afterwards, static measurements were performed with the femtosecond XUV pulses in order to investigate the suitability of two different modes of operation of the HHG source for pump-probe experiments. Furthermore, vacuum space-charge (VSC) effects, one of the main aspects limiting the performance, were studied. Based on the observation, experimental conditions that are suitable for time- and spin-resolved PES studies have been found (see Chap. 5). The analysis of the VSC effects was further extended by investigations of the influence of the near-infrared (NIR) pump-pulses on the measurement results. We observed an effect on time scales that are far longer than the processes in ultrafast magnetization dynamics. In addition, the stability conditions in our setup were estimated and improved to fulfill the needs of pump-probe measurements (see Chap. 6). Finally, the feasibility of simultaneous time-, energy- and spin-resolved measurements covering the full binding energy range of the valence bands was demonstrated leading to new insights into the dynamics of the band structure during ultrafast demagnetization. In particular, no indication of a quenching of the exchange splitting has been found (see Chap. 7).

Based on the findings in the last chapter, several pump-induced changes in the photoemission spectra that were observed need a clarification in future experiments. For example, a verification of the k_{\parallel} -independence of the electron excitation (see right side of Fig. 7.4) for a broader range of wave vectors is necessary and needs to be compared to corresponding band structure calculations. The latter can be also used to understand the evolution of the hot electron distribution in more

detail. From experimental side, in particular a higher temporal resolution, which is easily achievable using shorter pump-pulses, and a concentration on the energy range around $E_B = 0$ to increase the statistics would allow spin-resolved studies of the relaxation dynamics in order to identify, *e.g.*, spin-flip processes. This can go along with a change of the wave vector which is probed and thus provide direct insights into the influence of differences in the band hybridization on the spin-flip probabilities [Pickel08].

Moreover, the simultaneous change of the spin polarization over the full measured energy range needs further investigations. Demagnetization curves with smaller delay steps compared to the results shown on the right side of Fig. 7.6 can study possible variations in the demagnetization-onset time and the overall demagnetization time for different electron binding energies. This is expected to test the suggestion of a mechanism inducing a constant, parallel quenching of the spin polarization. Here, a better temporal resolution would be again helpful and possible delays of the energy range that is not directly excited by the NIR pump-beam are especially interesting.

Another aspect, which has to be still further validated, is the absence of peak shifts in our results. For a clearer analysis of the experimental results, a better separation of the minority peak from the cut-off at E_F for Co(001) would be helpful. This can be achieved by, *e.g.*, varying the emission angle and therefore k_{\parallel} (see Fig. 4.4). Upcoming time- and spin-resolved measurements would also profit from a better energy resolution (for example by decreasing E_{pass}) because smaller peak shifts can be determined.

In order to identify the role of fluctuating regions with a locally conserved band structure, static studies of the equilibrium¹ situation for temperatures approaching T_C are necessary. However, for thin films of Co grown on Cu(001) or Au(111) a non-transient heating generally leads to diffusion of the substrate material to the surface. Therefore, static photoemission measurements of the influence of equilibrium heating on the band structure are challenging. However, additional information about the relation between the equilibrium and non-equilibrium situation in 3d ferromagnets might come from measurement on, *e.g.*, Fe on MgO or Ni on W. In general, the main goal of the thesis was to prove the concept of our experimental approach. The setup still allows for technical optimizations including improvement of the spin detector efficiency. The efficiency enhancement can be used for a better energy resolution, as discussed above, or for the investigation of a wider parameter space, for example by increasing the density or range of delay steps. It might also enable time-resolved experiments using the HHG source in red-driven mode (RDM), which allows a variation of the k_{\perp} direction in the Brillouin zone (BZ) (see Sec. 3.1). This is especially interesting, because the $\Delta_{5\downarrow}$ band in face-centered tetragonal (fct) Co is located at larger binding energies for an excitation with higher photon energies

¹Here, equilibrium means that the electron system is in equilibrium with the lattice.

and therefore leaves the vicinity of the Fermi edge (see Fig. 5.3). Higher count rates might even allow for spin- and time-resolved resonant photoemission at the $3p$ core levels of $3d$ ferromagnets (see Sec. 3.1), which can be directly related to results obtained with the transverse magneto-optical Kerr effect (MOKE) at the M-absorption edges.

At present, a differentiation between processes that locally occur at the place of excitation (*e.g.* spin-flips) and mechanisms that transport the magnetic moment away from the excited area (*e.g.* spin-currents) is difficult in our experiment. A combined investigation of a sample with surface-sensitive PES and the more bulk-sensitive transverse MOKE using HHG radiation (or alternatively x-ray magnetic circular dichroism (XMCD) with synchrotron femtoslicing) might help to disentangle such effects. Furthermore, non-local (transport) effects can be studied by separating the optical excitation and the probing, for example in an experimental geometry allowing the pump-beam to arrive from the back of the sample through a transparent substrate². If the sample system is thick enough to absorb the intensity of the pump-beam but still transmits spin-currents, *i.e.* several tens of nm [Eschenlohr13], probing the front of the sample by PES can deliver information purely about transport effects.

Moreover, our setup can be applied to expand the view on other materials with interesting spin properties like $4f$ ferromagnets or MoS_2 , as already discussed in the introduction (see Chap. 1).

²Au/Fe bilayers grown on MgO can serve as a possible sample system for such studies [Melnikov11].

Appendix

Symmetry Properties of Electronic States

| | Basis Functions | E | C_4^2 | C_4 | JC_4^2 | JC_2 |
|-------------|--------------------------|-----|---------|-------|----------|--------|
| Δ_1 | $1, z, 2z^2 - x^2 - y^2$ | 1 | 1 | 1 | 1 | 1 |
| Δ_2 | $x^2 - y^2$ | 1 | 1 | -1 | 1 | -1 |
| Δ_2' | xy | 1 | 1 | -1 | -1 | 1 |
| Δ_1' | $xy(x^2 - y^2)$ | 1 | 1 | 1 | -1 | -1 |
| Δ_5 | x, y, xz, yz | 2 | -2 | 0 | 0 | 0 |

Basis functions and character table for the Δ -direction in the simple cubic lattice. The first column shows the irreducible representations of the group, which are associated with the wave functions of the electronic states. Next to it basis functions are shown that transform accordingly (the \hat{z} - corresponds to the Δ -direction). In the right part, the first row gives the symmetry operations of the group (C_{4v}) in Schoenflies-notation, whereas a J indicates that the operation is followed by an inversion. The entries represent the so-called "characters". Their values give information about the degeneracy of the state, and the signs represent the parity of the wave function under the transformation. (adapted from [Dresselhaus08], where a lot of additional details can be found)

MATLAB Source Code for Simulations of Pump-induced Vacuum Space-charge Effects

```
% This script simulates the movement of the pump-induced electron cloud
% and an interacting probe electron
% 1. step: calculate the positions of the slices of the pump-induced
%   electron cloud/the probe electron after their creation up to the
%   time, when both pulses have arrived at the sample
% 2. step: calculate the total energy (kinetic + potential energy) of
%   the probe electron at the first time (m=1) when the pump-induced
%   electrons as well as the probe electron are present
% 3. step: for each subsequent time step: calculate the new position of
%   the probe electron using the kinetic energy from the step before;
```

APPENDIX

```
% calculate the new positions of the pump-induced electron slices =>
% calculate the new potential energy of the probe electron in the
% field of the pump-induced electron cloud => calculate the new
% kinetic energy of the probe electron by subtracting the new
% potential energy from the total energy (energy conservation, Etot
% from step 2)
% 4. step: repeat step 3 until the probe electron has propagated the
% distance to the spectrometer entrance
% the position of an undisturbed HHG reference electron is always
% calculated as well for comparison

clear; close all;
% START ----- DEFINE INPUT PARAMETERS -----
d=0.9e-3; % spot diameter of the pump beam in m
rep_rate=5000; % laser repetition rate in Hz
% distance between sample and detector in m:
distance_to_detector = 25e-3;
% sample current generated by the pump-beam:
sample_current=0.9e-9; % in A
% kinetic energy of the probe electron:
E_HHG=15; % in eV

% mean kinetic energy (gauss_b) and width (gauss_c) of the pump-induced
% electron cloud; assuming a Gaussian distribution:
gauss_b=5; % in eV
gauss_c=7; % in eV
% kinetic energies of the slices that model the pump-induced electron
% cloud:
E_pump=0.2:0.2:28; % in eV

% (approx.) number of time steps that are simulated for each delay
% (used to determine step size):
calculation_time_steps=500;

% maximum/minimum delay that is simulated and number of steps in
% between:
delay_min=-13e-9; % in s
delay_max=20e-9; % in s
delay_steps=330; % in s

% general constants:
eps=8.85e-12; % (A s)/(V m)
e=1.6e-19; % in C
c=3e8; % in m/s
m_e=9.11e-31; % in kg
% END ----- DEFINE INPUT PARAMETERS -----

% START ----- CALCULATE GENERAL PARAMETERS -----
r=d/2; % calculate the spot radius (from the spot diameter)
% calculate the number of pump-induced electrons from the sample
```

```

% current:
N_pump=sample_current./(e.*rep_rate);
% create the pump-induced electron cloud:
int_E_pump=exp(-(((E_pump-gauss_b)./gauss_c).^2)./2);
% normalize the pump-induced electron cloud to the number of pump-
% induced electrons:
int_E_pump=int_E_pump.*N_pump./sum(int_E_pump);
% calculate the velocity for each slice of the pump-induced electron
% cloud:
for j=1:length(E_pump)
    v_pump(j)=sqrt(2*(E_pump(j).*e)./m_e);
end;
% create a list of delays:
delay_l=delay_min:((delay_max-delay_min)./delay_steps):delay_max;

% calculate the velocity of the undisturbed HHG reference electron:
v_HHG_out=sqrt(2*(E_HHG*e)./m_e);
% calculate the time that the undisturbed HHG reference electron needs
% to reach the distance of the spectrometer entrance:
t_max = (distance_to_detector./v_HHG_out);
% calculate the corresponding size of the time steps for the
% simulation:
diff_t=(t_max./calculation_time_steps);
% END ----- CALCULATE GENERAL PARAMETERS -----

% START ----- SIMULATION -----
% repeat the simulation for each delay:
for n=1:length(delay_l)
    delay=delay_l(n);
    % display progress of the delay list in percent:
    (n./(length(delay_l))*100
    % set the number of time steps that are already simulated for this
    % delay (pump-induced electron cloud and probe electron are present)
    % to zero:
    m=0;
    % repeat the simulation for this delay until the probe electron
    % reaches the distance of the spectrometer entrance (each repetition
    % simulates a time steps):
    for i=1:inf
        % set the potential energy of the probe electron in the field of the
        % pump-induced electron cloud at the actual time step to zero
        % (initialize):
        pot_ges(i)=0;
        % calculate the 'time after excitation' for the pump-induced electron
        % cloud for the current time step; t_IR=0: pump-pulse arrives at
        % the sample:
        t_IR(i)=((i-1).*diff_t);
        % calculate the 'time after excitation' for the probe electron for
        % the current time step; t_HHG=0: probe-pulse arrives at the
        % sample:

```


APPENDIX

```
t_HHG(i)=t_IR(i)-delay;
% calculate the position of the pump-induced electron slices for the
% current time step, if the pump-pulse has already arrived at the
% sample:
if (t_IR(i)>=0)
    for j=1:1:length(E_pump)
        x_pump(i,j)=v_pump(j).*(t_IR(i));
    end;
end;
% if both pulses have arrived at the sample, start to calculate their
% interaction:
if (t_HHG(i)>=0)&&(t_IR(i)>=0)
    % increase the internal index m:
    m=m+1;

    if m==1
        % For the first time step, when both the probe electron and the
        % pump-induced electron cloud are created (first time, when
        % t_HHG>0 and t_IR>0), the total energy (Etot=Epot+Ekin) is
        % calculated. This value is used as a reference (energy
        % conservation) for all subsequent time steps.

        % calculate the velocity of the probe electron (from orig. Ekin):
        v_HHG(i)=sqrt(2*e*E_HHG./m_e);
        % calculate the position of the probe electron:
        x_HHG(i)=v_HHG(i)*t_HHG(i);
        % calculate the velocity of the undisturbed HHG reference electron:
        v_HHG_und(i)=sqrt(2*e*E_HHG./m_e);
        % calculate the position of the undisturbed reference HHG electron:
        x_HHG_und(i)=v_HHG_und(i)*t_HHG(i);
        for j=1:1:length(E_pump)
            % for each slice of the pump-induced electron cloud...
            % ...calculate the distance to the probe electron:
            x_diff(i,j)=x_pump(i,j)-x_HHG(i);
            % ...then calculate the resulting potential energy of the probe
            % electron in the field of this slice:
            sr=(sqrt(x_diff(i,j).^2+r.^2)-abs(x_diff(i,j)));
            pot(i,j)=int_E_pump(j)*e./(2*pi*eps)*1/(r.^2)*sr;
            % ... and sum the potential energy up for all slices:
            pot_ges(i)=pot_ges(i)+pot(i,j);
        end;
        % calculate the total energy of the probe electron:
        Eges=pot_ges(i)+E_HHG;
        % set the kinetic energy of the probe electron after this time step
        % (assumed as being still the original E_HHG):
        Ekin_after(i)=E_HHG;
        % set the kinetic energy of the undisturbed HHG reference electron
        % after this time step (is always the original E_HHG):
        E_und_after(i)=E_HHG;
    end;
```

```

if m>1
% For every time step after the first one, the new positions of the
% probe electron and all pump-induced electron slices is
% calculated from the corresponding positions in the previous
% time step using the kinetic energy (and thus the velocity)
% after the previous time step. Then, a new kinetic energy is
% calculated for the probe electron.

% calculate the velocity of the probe electron after the previous
% time step (Ekin from i-1):
v_HHG(i)=sqrt(2.*e.*Ekin_after(i-1)./m_e);
% use this velocity to calculate the new position of the probe
% electron:
x_HHG(i)=(t_HHG(i)-t_HHG(i-1)).*v_HHG(i) + x_HHG(i-1);
% calculate the velocity of the undisturbed HHG reference electron
% after the previous time step:
v_HHG_und(i)=sqrt(2.*e.*E_und_after(i-1)./m_e);
% use this velocity to calculate the new position of the
% undisturbed HHG reference electron:
x_HHG_und(i)=(t_HHG(i)-t_HHG(i-1)).*v_HHG_und(i) + x_HHG_und(i-1);
for j=1:1:length(E_pump)
% for each slice of the pump-induced electron cloud...
% ...calculate the distance to the probe electron at the current
% time step:
x_diff(i,j)=x_pump(i,j)-x_HHG(i);
% ...then calculate the resulting potential energy of the probe
% electron:
sr=(sqrt(x_diff(i,j).^2+r.^2)-abs(x_diff(i,j)));
pot(i,j)=int_E_pump(j)*e./(2*pi*eps)*1/(r.^2)*sr;
% ... and sum the potential energy up for all slices:
pot_ges(i)=pot_ges(i)+pot(i,j);
end;
% calculate the new kinetic energy of the probe electron after this
% time step by subtracting its new potential energy from its
% total energy at the beginning (energy conservation: loss of
% Epot => acceleration, gain of Epot => deceleration):
Ekin_after(i)=Eges-pot_ges(i);
% set the kinetic energy of the undisturbed HHG reference electron
% after this time step (is always the original E_HHG):
E_und_after(i)=E_HHG;
end;

% save the position of the probe electron when it reaches the
% distance of the spectrometer entrance and the corresponding
% index of the time step in the simulation (for the calculation
% of the final Ekin):
last_i_HHG(n)=i;
last_x_HHG(n)=x_HHG(i);
else

```

APPENDIX

```
% fill the position arrays with zeros for time steps, when not both
%   pulses have arrived at the sample yet
x_HHG(i)=0;
x_HHG_und(i)=0;
x_diff(i,j)=0;
end;
% stop the simulation when the probe electron propagated the distance
%   to the spectrometer entrance:
if x_HHG(i)>=distance_to_detector
    break
end;
clear sr;
end;
% save the final kinetic energy at the spectrometer entrance distance
%   for this delay...
% ...for the probe electron:
Ekin_final(n)=Ekin_after(last_i_HHG(n));
% ...and the undisturbed HHG reference electron:
E_und_final(n)=E_und_after(last_i_HHG(n));
end;

% END ----- SIMULATION -----
```

List of Abbreviations

| | |
|--------------|---|
| AC | absorbed electron current |
| AES | Auger electron spectroscopy |
| ARPES | angle-resolved photoelectron spectroscopy |
| BBO | β -BaB ₂ O ₄ |
| BDM | blue-driven mode |
| BZ | Brillouin zone |
| CCD | charge-coupled device |
| CSA | cylindrical sector analyzer |
| cw | continuous wave |
| EAL | effective attenuation length |
| EDC | energy distribution curve |
| fct | face-centered tetragonal |
| FEL | free-electron laser |
| FoM | figure of merit |
| FWHM | full width at half maximum |
| HAMR | heat-assisted magnetic recording |
| HHG | high-order harmonic generation |
| IMFP | inelastic mean free path |
| IPES | inverse photoelectron spectroscopy |
| IT | information technology |

LIST OF ABBREVIATIONS

| | |
|---------------|--|
| LAPE | laser-assisted photoelectric effect |
| LEED | low-energy electron diffraction |
| MOKE | magneto-optical Kerr effect |
| NIR | near-infrared |
| PES | photoelectron spectroscopy |
| RC | reflected electron current |
| RDM | red-driven mode |
| SHG | second harmonic generation |
| SOC | spin-orbit coupling |
| SPLEED | spin-polarized low-energy electron diffraction |
| TBP | time bandwidth product |
| RT | room temperature |
| UHV | ultrahigh vacuum |
| UPS | ultraviolet photoelectron spectroscopy |
| VLEED | very low-energy electron diffraction |
| VSC | vacuum space-charge |
| XMCD | x-ray magnetic circular dichroism |
| XUV | extreme ultraviolet |
| ZD | zero delay |

Bibliography

- [Aeschlimann95] M Aeschlimann, C A Schmuttenmaer, H E Elsayed-Ali, R J D Miller, J Cao, Y Gao, and D A Mantell. *Observation of surface enhanced multiphoton photoemission from metal surfaces in the short pulse limit*. J. Chem. Phys. **102**(21), 8606 (1995). 78, 80
- [Aeschlimann97] M Aeschlimann, M Bauer, S Pawlik, W Weber, R Burgermeister, D Oberli, and HC Siegmann. *Ultrafast spin-dependent electron dynamics in fcc Co*. Phys. Rev. Lett. **79**(25), 5158 (1997). 6, 103
- [Allmers11] T Allmers and M Donath. *Controlling Cu diffusion in Co films grown on Cu (001)*. Surf. Sci. **605**(21), 1875 (2011). 8, 55
- [ALS] *ALS - Beamline directory*. <http://www-als.lbl.gov/index.php/beamlines/beamlines-directory/106-601.html>. [accessed 04-Mar-2015]. 33
- [Andres15] B Andres, M Christ, C Gahl, M Wietstruk, M Weinelt, and J Kirschner. *Separating Exchange Splitting from Spin Mixing in Gadolinium by Femtosecond Laser Excitation*. Phys. Rev. Lett. **115**, 207404 (2015). 8
- [Banfi03] G P Banfi, G Ferrini, M Peloi, and F Parmigiani. *Anomalous photoemission from Ag (100) in the femtosecond regime*. Phys. Rev. B: Condens. Matter **67**(3), 035428 (2003). 79, 80
- [Battiato10] M Battiato, K Carva, and P M Oppeneer. *Superdiffusive spin transport as a mechanism of ultrafast demagnetization*. Phys. Rev. Lett. **105**(2), 027203 (2010). 6
- [Bauer05] M Bauer. *Femtosecond ultraviolet photoelectron spectroscopy of ultra-fast surface processes*. J. Phys. D: Appl. Phys. **38**(16), R253 (2005). 43
- [Beaurepaire96] E Beaurepaire, J C Merle, A Daunois, and J-Y Bigot. *Ultrafast spin dynamics in ferromagnetic nickel*. Phys. Rev. Lett. **76**(22), 4250 (1996). 5, 6, 7

BIBLIOGRAPHY

- [Bertacco99a] R Bertacco and F Ciccacci. *Oxygen-induced enhancement of the spin-dependent effects in electron spectroscopies of Fe (001)*. Phys. Rev. B: Condens. Matter **59**(6), 4207 (1999). 30, 31, 51
- [Bertacco99b] R Bertacco, D Onofrio, and F Ciccacci. *A novel electron spin-polarization detector with very large analyzing power*. Rev. Sci. Instrum. **70**(9), 3572 (1999). 31
- [BESSY] *BESSY II - List of beamlines*. http://www.helmholtz-berlin.de/pubbin/igama_output?modus=einzel&sprache=en&gid=1642&typoid=50740. [accessed 04-Mar-2015]. 33
- [Bigot09] J-Y Bigot, M Vomir, and E Beaurepaire. *Coherent ultrafast magnetism induced by femtosecond laser pulses*. Nat. Phys. **5**(7), 515 (2009). 6, 7
- [Burnett93] K Burnett, V C Reed, and P L Knight. *Atoms in ultra-intense laser fields*. J. Phys. B: At., Mol. Opt. Phys. **26**(4), 561 (1993). 18
- [Campillo00] I Campillo, A Rubio, J M Pitarke, A Goldmann, and P M Echenique. *Hole dynamics in noble metals*. Phys. Rev. Lett. **85**(15), 3241 (2000). 70, 89
- [Carley12] R Carley, K Döbrich, B Frietsch, C Gahl, M Teichmann, O Schwarzkopf, P Wernet, and M Weinelt. *Femtosecond Laser Excitation Drives Ferromagnetic Gadolinium out of Magnetic Equilibrium*. Phys. Rev. Lett. **109**(5), 057401 (2012). 7, 68
- [CC-BY] *Creative Commons Attribution (CC BY) license*. <https://creativecommons.org/licenses/?lang=en>. [accessed 03-Aug-2016]. 52, 53
- [Chiang10] C-T Chiang, A Winkelmann, P Yu, J Kirschner, and J Henk. *Spin-orbit coupling in unoccupied quantum well states: Experiment and theory for Co/Cu (001)*. Phys. Rev. B: Condens. Matter **81**(11), 115130 (2010). 21, 59, 65, 67, 100, 104
- [Chiang12] C-T Chiang, A Blättermann, M Huth, J Kirschner, and W Widra. *High-order harmonic generation at 4 MHz as a light source for time-of-flight photoemission spectroscopy*. Appl. Phys. Lett. **101**(7), 071116 (2012). 33
- [Clarke87] A Clarke, G Jennings, R F Willis, P J Rous, and J B Pendry. *A LEED determination of the structure of cobalt overlayers grown*

- on a single-crystal Cu (001) substrate. *Surf. Sci.* **187**(2), 327 (1987). 55
- [Clemens92] W Clemens, T Kachel, O Rader, E Vescovo, S Blügel, C Carbone, and W Eberhardt. *Quantum size effects and the enhancement of the exchange splitting in ultrathin Co overlayers on Cu (100)*. *Solid State Commun.* **81**(9), 739 (1992). 20, 58
- [Corkum93] P B Corkum. *Plasma perspective on strong field multiphoton ionization*. *Phys. Rev. Lett.* **71**(13), 1994 (1993). 34
- [Crangle71] J Crangle and G M Goodman. *The magnetization of pure iron and nickel*. In *Proceedings of the Royal Society of London A: Mathematical, Physical and Engineering Sciences*, volume 321, pages 477–491. The Royal Society, (1971). 15
- [Damascelli96] A Damascelli, G Gabetta, A Lumachi, L Fini, and F Parmigiani. *Multiphoton electron emission from Cu and W: An angle-resolved study*. *Phys. Rev. B: Condens. Matter* **54**(9), 6031 (1996). 81, 83
- [Damascelli04] A Damascelli. *Probing the electronic structure of complex systems by ARPES*. *Phys. Scr.* **2004**(T109), 61 (2004). 24, 26
- [Day12] P R Day. *Emission and scattering techniques: studies of inorganic molecules, solids, and surfaces*, volume 73. Springer Science & Business Media, (2012). 25
- [De Miguel91] J J De Miguel, A Cebollada, J M Gallego, R Miranda, C M Schneider, P Schuster, and J Kirschner. *Influence of the growth conditions on the magnetic properties of fcc cobalt films: from monolayers to superlattices*. *J. Magn. Magn. Mater.* **93**, 1 (1991). 55
- [Diels06] J-C Diels and W Rudolph. *Ultrashort laser pulse phenomena*. Academic press, (2006). 68
- [Dietz79] E Dietz and F J Himpsel. *Photoemission via Bloch states and evanescent band gap states for Cu (110)*. *Solid State Commun.* **30**(4), 235 (1979). 24
- [Dombi13] P Dombi, A Hörl, P Rácz, I Márton, A Trügler, JR Krenn, and U Hohenester. *Ultrafast strong-field photoemission from plasmonic nanoparticles*. *Nano Lett.* **13**(2), 674 (2013). 79

BIBLIOGRAPHY

- [Donath89] M Donath and V Dose. *Temperature Behaviour of a Magnetic Band in Nickel*. Europhys. Lett. **9**(8), 821 (1989). 8
- [Dresselhaus08] M S Dresselhaus, G Dresselhaus, and A Jorio. *Applications of Group Theory to the Physics of Solids*, (2008). 20, I
- [Eberhardt80] W Eberhardt and F J Himpsel. *Dipole selection rules for optical transitions in the fcc and bcc lattices*. Phys. Rev. B: Condens. Matter **21**(12), 5572 (1980). 20, 21
- [Eich14] S Eich, A Stange, AV Carr, J Urbancic, T Popmintchev, M Wiesenmayer, K Jansen, A Ruffing, S Jakobs, T Rohwer, et al. *Time-and angle-resolved photoemission spectroscopy with optimized high-harmonic pulses using frequency-doubled Ti: Sapphire lasers*. J. Electron. Spectrosc. Relat. Phenom. (2014). 18, 41, 45, 68, 95, 100
- [Ellguth15] M Ellguth. *A spin- and momentum-resolved photoemission study of strong electron correlation in Co/Cu(001)*. PhD thesis, Martin-Luther-Universität Halle-Wittenberg, (2015). 59
- [Emmerich15] S Emmerich. *Aufbau und Inbetriebnahme einer hohen harmonischen Lichtquelle für die zeit- und winkelaufgelöste Photoemission*. Master's thesis, Technische Universität Kaiserslautern, (2015). 92, 95
- [Eschenlohr13] A Eschenlohr, M Battiato, P Maldonado, N Pontius, T Kachel, K Holldack, R Mitzner, A Föhlisch, P M Oppeneer, and C Stamm. *Ultrafast spin transport as key to femtosecond demagnetization*. Nat. Mater. **12**(4), 332 (2013). 6, 7, 109
- [Escher11] M Escher, N B Weber, M Merkel, L Plucinski, and C M Schneider. *FERRUM: A New Highly Efficient Spin Detector for Electron Spectroscopy*. e-J. Surf. Sci. Nanotech. **9**, 340 (2011). 51, 52, 53
- [Falcão-Filho10] E L Falcão-Filho, C-J Lai, K-H Hong, V-M Gkortsas, S-W Huang, L-J Chen, and F X Kärtner. *Scaling of high-order harmonic efficiencies with visible wavelength drivers: A route to efficient extreme ultraviolet sources*. Appl. Phys. Lett. **97**(6), 061107 (2010). 38, 41, 45, 74
- [Fann92] W S Fann, R Storz, H W K Tom, and J Bokor. *Electron thermalization in gold*. Phys. Rev. B: Condens. Matter **46**(20), 13592 (1992). 102

- [Ferrini09] G Ferrini, F Banfi, C Giannetti, and F Parmigiani. *Non-linear electron photoemission from metals with ultrashort pulses*. Nucl. Instr. Meth. Phys. Res. A **601**(1), 123 (2009). 78, 79
- [FLASH] *FLASH parameters*. http://photon-science.desy.de/facilities/flash/flash_parameters/index_eng.html. [accessed 04-Mar-2015]. 33
- [Foc09] Focus GmbH. *Instruction Manual: CSA200 / CSA 300*, 3.0 edition, (2009). 49, 50, 51
- [Fognini14] A Fognini, T U Michlmayr, G Salvatella, C Wetli, U Ramsperger, T Bähler, F Sorgenfrei, M Beye, A Eschenlohr, N Pontius, et al. *Ultrafast reduction of the total magnetization in iron*. Appl. Phys. Lett. **104**(3), 032402 (2014). 7
- [Fremerey99] J K Fremerey. *Residual gas: traditional understanding and new experimental results*. Vacuum **53**(1), 197 (1999). 60
- [Frietsch13] B Frietsch, R Carley, K Döbrich, C Gahl, M Teichmann, O Schwarzkopf, P Wernet, and M Weinelt. *A high-order harmonic generation apparatus for time-and angle-resolved photoelectron spectroscopy*. Rev. Sci. Instrum. **84**(7), 075106 (2013). 69, 73
- [Frietsch15] B Frietsch, J Bowlan, R Carley, M Teichmann, S Wienholdt, D Hinzke, U Nowak, K Carva, P M Oppeneer, and M Weinelt. *Disparate ultrafast dynamics of itinerant and localized magnetic moments in gadolinium metal*. Nat. Commun. **6** (2015). 8, 33
- [Gantz12] J Gantz and D Reinsel. *The digital universe in 2020: Big data, bigger digital shadows, and biggest growth in the far east*. IDC iView: IDC Analyze the Future **2007**, 1 (2012). 5
- [Gay92] T J Gay and F B Dunning. *Mott electron polarimetry*. Rev. Sci. Instrum. **63**(2), 1635 (1992). 16
- [Gehlmann15] M Gehlmann, G Bihlmayer, I Aguilera, E Mlynczak, M Eschbach, S Döring, P Gospodarcic, S Cramm, B Kardynal, L Plucinski, et al. *Quasi 2D electronic states with high spin-polarization in centrosymmetric MoS₂ bulk crystals*. arXiv preprint arXiv:1510.04101 (2015). 9
- [Gibson04] E A Gibson, A Paul, N Wagner, R Tobey, S Backus, I P Christov, M M Murnane, and H C Kapteyn. *High-order harmonic*

BIBLIOGRAPHY

- generation up to 250 eV from highly ionized argon. *Phys. Rev. Lett.* **92**(3), 033001 (2004). 36
- [Gierz13] I Gierz, J C Petersen, M Mitrano, C Cacho, IC E Turcu, E Springate, A Stöhr, A Köhler, U Starke, and A Cavalleri. *Snapshots of non-equilibrium Dirac carrier distributions in graphene*. *Nat. Mater.* **12**(12), 1119 (2013). 7, 33
- [Gkortsas11] V-M Gkortsas, S Bhardwaj, C-J Lai, K-H Hong, E L Falcão-Filho, and F X Kärtner. *Interplay of multiphoton and tunneling ionization in short-wavelength-driven high-order harmonic generation*. *Phys. Rev. A: At. Mol. Opt. Phys.* **84**(1), 013427 (2011). 36
- [Gobeli64] G W Gobeli, F G Allen, and E O Kane. *Polarization Evidence for Momentum Conservation in Photoelectric Emission from Germanium and Silicon*. *Phys. Rev. Lett.* **12**(4), 94 (1964). 24
- [Gohle05] C Gohle, T Udem, M Herrmann, J Rauschenberger, R Holzwarth, H A Schuessler, F Krausz, and T W Hänsch. *A frequency comb in the extreme ultraviolet*. *Nature* **436**(7048), 234 (2005). 33
- [Grechnev07] A Grechnev, I Di Marco, M I Katsnelson, A I Lichtenstein, J Wills, and O Eriksson. *Theory of bulk and surface quasiparticle spectra for Fe, Co, and Ni*. *Phys. Rev. B: Condens. Matter* **76**(3), 035107 (2007). 59
- [Grubisic Cabo15] A Grubisic Cabo, J A Miwa, S S Grønborg, J M Riley, J C Johannsen, C Cacho, O Alexander, R T Chapmann, E Springate, M Grioni, et al. *Observation of Ultrafast Free Carrier Dynamics in Single Layer MoS₂*. *Nano Lett.* (2015). 9
- [Grychtol14] P Grychtol, O Kfir, R Knut, E Turgut, D Zusin, D Popmintchev, T Popmintchev, H Nembach, J M Shaw, A Fleischer, et al. *Magnetic Circular Dichroism probed using High Harmonics*. In *International Conference on Ultrafast Phenomena*, page 10. Optical Society of America, (2014). 33
- [Guillot77] C Guillot, Y Ballu, J Paigné, J Lecante, K P Jain, P Thiry, R Pinchaux, Y Petroff, and L M Falicov. *Resonant photoemission in nickel metal*. *Phys. Rev. Lett.* **39**(25), 1632 (1977). 48
- [Hädrich14] S Hädrich, A Klenke, J Rothhardt, M Krebs, A Hoffmann, O Pronin, V Pervak, J Limpert, and A Tünnermann. *High photon*

- flux table-top coherent extreme-ultraviolet source*. Nat. Photonics 8(10), 779 (2014). 33
- [Heckmann94] O Heckmann, H Magnan, P Le Fevre, D Chandesris, and J J Rehr. *Crystallographic structure of cobalt films on Cu (001): elastic deformation to a tetragonal structure*. Surf. Sci. 312(1), 62 (1994). 18, 47, 55
- [Hellmann09] S Hellmann, K Rossnagel, M Marczynski-Bühlow, and L Kipp. *Vacuum space-charge effects in solid-state photoemission*. Phys. Rev. B: Condens. Matter 79(3), 035402 (2009). 69, 70, 71, 73
- [Hellmann12] S Hellmann, T Ott, L Kipp, and K Rossnagel. *Vacuum space-charge effects in nano-ARPES*. Phys. Rev. B: Condens. Matter 85(7), 075109 (2012). 7, 73
- [Henke93] B L Henke, E M Gullikson, and J C Davis. *X-ray interactions: photoabsorption, scattering, transmission, and reflection at E= 50-30,000 eV, Z= 1-92*. At. Data Nucl. Data Tables 54(2), 181 (1993). 46
- [Hillebrecht90] F U Hillebrecht, R Jungblut, and E Kisker. *Spin polarization of the metallic Fe 3s photoemission spectrum*. Phys. Rev. Lett. 65(19), 2450 (1990). 30
- [Hofmann12] S Hofmann. *Auger-and X-ray photoelectron spectroscopy in materials science: a user-oriented guide*, volume 49. Springer Science & Business Media, (2012). 23, 56
- [Hohlfeld97] J Hohlfeld, E Matthias, R Knorren, and K H Bennemann. *Nonequilibrium magnetization dynamics of nickel*. Phys. Rev. Lett. 78(25), 4861 (1997). 7
- [Hopster83] H Hopster, R Raue, G Güntherodt, E Kisker, R Clauberg, and M Campagna. *Temperature dependence of the exchange splitting in Ni studied by spin-polarized photoemission*. Phys. Rev. Lett. 51(9), 829 (1983). 7, 8
- [Huang84] H Huang, X-Y Zhu, and J Hermanson. *Ni overlayer on a Cu {100} substrate: Magnetism and surface states*. Phys. Rev. B: Condens. Matter 29(4), 2270 (1984). 77
- [Huang93] D-J Huang, J-Y Lee, J-S Suen, G A Mulhollan, A B Andrews, and J L Erskine. *Adapting a compact Mott spin polarimeter to a large commercial electron energy analyzer for spin-polarized electron spectroscopy*. Rev. Sci. Instrum. 64(12), 3474 (1993). 29

BIBLIOGRAPHY

- [Huang02] D J Huang, W P Wu, J Chen, C F Chang, S C Chung, M Yuri, H-J Lin, P D Johnson, and C T Chen. *Performance of a Mott detector for undulator-based spin-resolved spectroscopy*. Rev. Sci. Instrum. **73**(11), 3778 (2002). 29
- [Hüfner95] S Hüfner. *Photoelectron Spectroscopy*. Springer, Berlin, (1995). 17, 22, 24, 27, 48
- [Ibach02] H Ibach and H Lüth. *Festkörperphysik Einführung In Die Grundlagen*. Springer Science & Business, (2002). 13, 15
- [Johnson07] P D Johnson and G Güntherodt. *Spin-polarized Photoelectron Spectroscopy as a Probe of Magnetic Systems*. Wiley Online Library, (2007). 29
- [Kämper90] K-P Kämper, W Schmitt, and G Güntherodt. *Temperature and wave-vector dependence of the spin-split band structure of Ni (111) along the Γ -L line*. Phys. Rev. B: Condens. Matter **42**(16), 10696 (1990). 8
- [Keeler08] J Keeler and P Wothers. *Chemical structure and reactivity: an integrated approach*. Oxford University Press, (2008). 25
- [Kessler85] J Kessler. *Polarized electrons*, volume 1. Springer Science & Business Media, (1985). 29
- [Kfir15] O Kfir, P Grychtol, E Turgut, R Knut, D Zusin, D Popmintchev, T Popmintchev, H Nembach, J M Shaw, A Fleischer, et al. *Generation of bright phase-matched circularly-polarized extreme ultraviolet high harmonics*. Nat. Photonics **9**(2), 99 (2015). 33
- [Kief93] M T Kief and W F Egelhoff Jr. *Growth and structure of Fe and Co thin films on Cu (111), Cu (100), and Cu (110): A comprehensive study of metastable film growth*. Phys. Rev. B: Condens. Matter **47**(16), 10785 (1993). 55
- [Kirschner88] J Kirschner and E Langenbach. *Temperature dependence of the exchange splitting in Ni studied by spin-polarized electron-energy-loss spectroscopy*. Solid State Commun. **66**(7), 761 (1988). 8
- [Kisker84] E Kisker. *Photoemission and finite temperature ferromagnetism of Fe and Ni*. J. Magn. Magn. Mater. **45**(1), 23 (1984). 7, 106
- [Koopmans10] B Koopmans, G Malinowski, F Dalla Longa, D Steiauf, M Fähnle, T Roth, M Cinchetti, and M Aeschlimann. *Explaining*

- the paradoxical diversity of ultrafast laser-induced demagnetization*. Nat. Mater. **9**(3), 259 (2010). 6, 7
- [Krams92] P Krams, F Lauks, R L Stamps, B Hillebrands, and G Güntherodt. *Magnetic anisotropies of ultrathin Co (001) films on Cu (001)*. Phys. Rev. Lett. **69**(25), 3674 (1992). 55
- [Kuch95] W Kuch, M-T Lin, K Meinel, C M Schneider, J Noffke, and J Kirschner. *Spin-resolved substrate band mapping in Fe/Cu (100): Application of the spin-filter effect*. Phys. Rev. B: Condens. Matter **51**(18), 12627 (1995). 59
- [Kuch01] W Kuch and C M Schneider. *Magnetic dichroism in valence band photoemission*. Rep. Prog. Phys. **64**(2), 147 (2001). 21
- [Kulander93] K C Kulander, K J Schafer, and J L Krause. *Proceedings of the Workshop, Super Intense Laser Atom Physics (SILAP) III*, (1993). 34
- [Kupersztzych01] J Kupersztzych, P Monchicourt, and M Raynaud. *Ponderomotive acceleration of photoelectrons in surface-plasmon-assisted multiphoton photoelectric emission*. Phys. Rev. Lett. **86**(22), 5180 (2001). 79, 82
- [Kutnyakhov13] D Kutnyakhov, P Lushchik, A Fognini, D Perriard, M Kolbe, K Medjanik, E Fedchenko, S A Nepijko, H J Elmers, G Salvatella, et al. *Imaging spin filter for electrons based on specular reflection from iridium (001)*. Ultramicroscopy **130**, 63 (2013). 32
- [La-O-Vorakiat09] C La-O-Vorakiat, M Siemens, M M Murnane, H C Kapteyn, S Mathias, M Aeschlimann, P Grychtol, R Adam, C M Schneider, J M Shaw, et al. *Ultrafast demagnetization dynamics at the M edges of magnetic elements observed using a tabletop high-harmonic soft x-ray source*. Phys. Rev. Lett. **103**(25), 257402 (2009). 45
- [Lambert14] C-H Lambert, S Mangin, B C S Varaprasad, Y K Takahashi, M Hehn, M Cinchetti, G Malinowski, K Hono, Y Fainman, M Aeschlimann, et al. *All-optical control of ferromagnetic thin films and nanostructures*. Science **345**(6202), 1337 (2014). 6
- [Li90] H Li and B P Tonner. *Structure and growth mode of metastable fcc cobalt ultrathin films on Cu (001) as determined by angle-resolved x-ray photoemission scattering*. Surf. Sci. **237**(1), 141 (1990). 55

BIBLIOGRAPHY

- [Malinowski08] G Malinowski, F Dalla Longa, J H H Rietjens, P V Paluskar, R Huijink, H J M Swagten, and B Koopmans. *Control of speed and efficiency of ultrafast demagnetization by direct transfer of spin angular momentum*. Nat. Phys. 4(11), 855 (2008). 6
- [Marcatili64] E A J Marcatili and R A Schmeltzer. *Hollow metallic and dielectric waveguides for long distance optical transmission and lasers*. Bell Syst. Tech. J. 43(4), 1783 (1964). 40
- [Mathias07] S Mathias, L Miaja-Avila, M M Murnane, H C Kapteyn, M Aeschlimann, and M Bauer. *Angle-resolved photoemission spectroscopy with a femtosecond high harmonic light source using a two-dimensional imaging electron analyzer*. Rev. Sci. Instrum. 78(8), 083105 (2007). 33, 45, 95
- [Mathias12] S Mathias, C La-O-Vorakiat, P Grychtol, P Granitzka, E Turgut, J M Shaw, R Adam, H T Nembach, M E Siemens, S Eich, et al. *Probing the timescale of the exchange interaction in a ferromagnetic alloy*. Proc. Natl. Acad. Sci. U.S.A. 109(13), 4792 (2012). 7
- [Melnikov11] A Melnikov, I Razdolski, T O Wehling, E T Papaioannou, V Roddatis, P Fumagalli, O Aktsipetrov, A I Lichtenstein, and U Bovensiepen. *Ultrafast transport of laser-excited spin-polarized carriers in Au/Fe/MgO (001)*. Phys. Rev. Lett. 107(7), 076601 (2011). 6, 109
- [Miaja-Avila06] L Miaja-Avila, C Lei, M Aeschlimann, J L Gland, M M Murnane, H C Kapteyn, and G Saathoff. *Laser-assisted photoelectric effect from surfaces*. Phys. Rev. Lett. 97(11), 113604 (2006). 77, 98
- [Miyamoto08a] K Miyamoto, K Iori, K Sakamoto, A Kimura, S Qiao, K Shimada, H Namatame, and M Taniguchi. *Spin-dependent electronic band structure of Co/Cu (001) with different film thicknesses*. J. Phys.: Condens. Matter 20(22), 225001 (2008). 47, 58, 60, 100
- [Miyamoto08b] K Miyamoto, K Iori, K Sakamoto, H Narita, A Kimura, M Taniguchi, S Qiao, K Hasegawa, K Shimada, H Namatame, et al. *Spin polarized d surface resonance state of fcc Co/Cu (001)*. New J. Phys. 10(12), 125032 (2008). 60
- [Monastra02] S Monastra, F Manghi, C A Rozzi, C Arcangeli, E Wetli, H-J Neff, T Greber, and J Osterwalder. *Quenching of majority-channel quasiparticle excitations in cobalt*. Phys. Rev. Lett. 88(23), 236402 (2002). 59

- [Mueller13] B Y Mueller, A Baral, S Vollmar, M Cinchetti, M Aeschlimann, H C Schneider, and B Rethfeld. *Feedback effect during ultrafast demagnetization dynamics in ferromagnets*. Phys. Rev. Lett. 111(16), 167204 (2013). 7, 103
- [Musumeci10] P Musumeci, L Cultrera, M Ferrario, D Filippetto, G Gatti, M S Gutierrez, J T Moody, N Moore, J B Rosenzweig, C M Scoby, et al. *Multiphoton photoemission from a copper cathode illuminated by ultrashort laser pulses in an RF photoinjector*. Phys. Rev. Lett. 104(8), 084801 (2010). 82
- [Nolting02] W Nolting. *Grundkurs Theoretische Physik 5 Quantenmechanik, Teil 1: Grundlagen*. Springer-Verlag, (2002). 24
- [Nolting13] W Nolting. *Grundkurs Theoretische Physik 5 Quantenmechanik: Teil 2: Methoden und Anwendungen*. Springer-Verlag, (2013). 29
- [Okuda08] T Okuda, Y Takeichi, Yi Maeda, A Harasawa, I Matsuda, T Kinoshita, and A Kakizaki. *A new spin-polarized photoemission spectrometer with very high efficiency and energy resolution*. Rev. Sci. Instrum. 79(12), 123117 (2008). 31
- [Oloff14] L P Oloff, M Oura, K Rossnagel, A Chainani, M Matsunami, R Eguchi, T Kiss, Y Nakatani, T Yamaguchi, J Miyawaki, et al. *Time-resolved HAXPES at SACLA: probe and pump pulse-induced space-charge effects*. New J. Phys. 16(12), 123045 (2014). 85
- [Opel04] M Opel. *lecture notes: Magnetismus (PH-E23-6) im WS 2004/2005*. University lecture at the TU München, (2004). 13
- [Osterwalder06] J Osterwalder. *Spin-polarized photoemission*. In *Magnetism: A Synchrotron Radiation Approach*, page 95. Springer, (2006). 27
- [Passlack06] S Passlack, S Mathias, O Andreyev, D Mittnacht, M Aeschlimann, and M Bauer. *Space charge effects in photoemission with a low repetition, high intensity femtosecond laser source*. J. Appl. Phys. 100(2), 024912 (2006). 69, 70
- [Pfau12] B Pfau, S Schaffert, L Müller, C Gutt, A Al-Shemmary, F Büttner, R Delaunay, S Düsterer, S Flewett, R Frömter, et al. *Ultrafast optical demagnetization manipulates nanoscale spin structure in domain walls*. Nat. Commun. 3, 1100 (2012). 7

BIBLIOGRAPHY

- [Pfeifer06] T Pfeifer, C Spielmann, and G Gerber. *Femtosecond x-ray science*. Rep. Prog. Phys. **69**(2), 443 (2006). 34, 35, 37, 38, 40
- [Pickel08] M Pickel, A B Schmidt, F Giesen, J Braun, J Minár, H Ebert, M Donath, and M Weinelt. *Spin-orbit hybridization points in the face-centered-cubic cobalt band structure*. Phys. Rev. Lett. **101**(6), 066402 (2008). 6, 7, 8, 20, 108
- [Pietzsch08] A Pietzsch, A Föhlisch, M Beye, M Deppe, F Hennies, M Nagasono, E Suljoti, W Wurth, C Gahl, K Döbrich, et al. *Towards time resolved core level photoelectron spectroscopy with femtosecond x-ray free-electron lasers*. New J. Phys. **10**(3), 033004 (2008). 69
- [Plötzing11] M Plötzing. *Ultrafast Demagnetization Dynamics in Ni_xPd_{1-x} alloys*. Master's thesis, RWTH Aachen University, (2011). 14
- [Plötzing16] M Plötzing, R Adam, C Weier, L Plucinski, S Eich, S Emmerich, M Rollinger, M Aeschlimann, S Mathias, and C M Schneider. *Spin-resolved photoelectron spectroscopy using femtosecond extreme ultraviolet light pulses from high-order harmonic generation*. Rev. Sci. Instrum. **87**(4), 043903 (2016). 43, 44, 46, 47, 58, 61, 62, 66, 67, 70, 72, 84, 85, 87
- [Popmintchev12] T Popmintchev, M-C Chen, D Popmintchev, P Arpin, S Brown, S Ališauskas, G Andriukaitis, T Balčiūnas, O D Mücke, A Pugzlys, et al. *Bright coherent ultrahigh harmonics in the keV X-ray regime from mid-infrared femtosecond lasers*. Science **336**(6086), 1287 (2012). 33
- [Qiao97] S Qiao and A Kakizaki. *Monte Carlo calculations for the design of Mott scattering spin polarimeters*. Rev. Sci. Instrum. **68**(11), 4017 (1997). 29
- [Quast07] T Quast, A Firsov, K Holldack, S Khan, and R Mitzner. *Upgrade of the BESSY femtoslicing source*. In *Particle Accelerator Conference, 2007. PAC. IEEE*, page 950. IEEE, (2007). 33
- [Radu09] I Radu, G Woltersdorf, M Kiessling, A Melnikov, U Bovensiepen, J-U Thiele, and C H Back. *Laser-induced magnetization dynamics of lanthanide-doped permalloy thin films*. Phys. Rev. Lett. **102**(11), 117201 (2009). 7
- [Rausch13] T Rausch, J D Trantham, A S Chu, H Dakroub, J W Riddering, C P Henry, J D Kiely, E C Gage, and J W Dykes. *HAMR drive*

- performance and integration challenges.* IEEE Trans. Magn. 49(2), 730 (2013). 5
- [Rhie03] H-S Rhie, H A Dürr, and W Eberhardt. *Femtosecond Electron and Spin Dynamics in Ni/W (110) Films.* Phys. Rev. Lett. 90(24), 247201 (2003). 7, 8, 80, 102, 103
- [Riffe93] D M Riffe, R M More, X Y Wang, M C Downer, D L Fisher, T Tajima, and J L Erskine. *Femtosecond thermionic emission from metals in the space-charge-limited regime.* J. Opt. Soc. Am. 10(8), 1424 (1993). 78, 79, 82, 83
- [Risley72] J S Risley. *Design parameters for the cylindrical mirror energy analyzer.* Rev. Sci. Instrum. 43(1), 95 (1972). 50
- [Rogers08] E T F Rogers. *Modelling of capillary high harmonic generation.* PhD thesis, University of Southampton, (2008). 38, 39
- [Rohwer11] T Rohwer, S Hellmann, M Wiesenmayer, C Sohrt, A Stange, B Slomski, A Carr, Y Liu, L M Avila, M Källäne, et al. *Collapse of long-range charge order tracked by time-resolved photoemission at high momenta.* Nature 471(7339), 490 (2011). 7, 33
- [Rubio-Zuazo11] J Rubio-Zuazo and G R Castro. *First principle study of the properties of a Cylindrical Sector Analyzer: Complete calculation of the electron trajectory.* J. Electron. Spectrosc. Relat. Phenom. 184(8), 440 (2011). 50
- [Rudolf12] D Rudolf, C La-O-Vorakiat, M Battiato, R Adam, J M Shaw, E Turgut, P Maldonado, S Mathias, P Grychtol, H T Nembach, et al. *Ultrafast magnetization enhancement in metallic multilayers driven by superdiffusive spin current.* Nat. Commun. 3, 1037 (2012). 6, 7, 45
- [Saathoff08] G Saathoff, L Miaja-Avila, M Aeschlimann, M M Murnane, and H C Kapteyn. *Laser-assisted photoemission from surfaces.* Phys. Rev. A: At. Mol. Opt. Phys. 77(2), 022903 (2008). 98
- [SACLA] *SACLA parameters.* http://www.lightsources.org/sites/default/files/legacy/posters/facility/Poster_SACLA_SRI_A0.pdf. [accessed 04-Mar-2015]. 33
- [Sakurai94] J J Sakurai. *Modern Quantum Mechanics.* Wesley Publishing Company, (1994). 19

BIBLIOGRAPHY

- [Schäfers96] F. Schäfers. *REFLEC: A Program to Calculate VUV/X-ray Optical Elements and Synchrotron Radiation Beamlines*. Technischer Bericht: Berliner Elektronenspeicherring-Gesellschaft für Synchrotronstrahlung. BESSY, (1996). 45
- [Schattke08] W Schattke and M A Van Hove. *Solid-state photoemission and related methods: theory and experiment*. John Wiley & Sons, (2008). 18
- [Schmid92] A K Schmid and J Kirschner. *In situ observation of epitaxial growth of Co thin films on Cu (100)*. *Ultramicroscopy* 42, 483 (1992). 55
- [Schneider90a] C M Schneider. *Electronic Structure and Magnetic Properties Of Ultrathin Epitaxial Films: fcc-Cobalt on Cu(100)*. PhD thesis, Freie Universität Berlin, (1990). 57
- [Schneider90b] C M Schneider, P Bressler, P Schuster, J Kirschner, J J De Miguel, and R Miranda. *Curie temperature of ultrathin films of fcc-cobalt epitaxially grown on atomically flat Cu (100) surfaces*. *Phys. Rev. Lett.* 64(9), 1059 (1990). 55
- [Schneider91a] C M Schneider, P Schuster, M Hammond, H Ebert, J Noffke, and J Kirschner. *Spin-resolved electronic bands of FCT cobalt*. *J. Phys.: Condens. Matter* 3(24), 4349 (1991). 58, 59
- [Schneider91b] C M Schneider, P Schuster, M S Hammond, and J Kirschner. *Spin-polarized photoemission from fcc-cobalt above the Curie temperature: evidence of short-range magnetic order*. *Europhys. Lett.* 16(7), 689 (1991). 8, 106
- [Schneider10] C M Schneider. *Ultrakurze Laserimpulse: Erzeugung, Handhabung, Nachweis*. In *FEMTOSEKUNDEN UND NANO-EV: DYNAMIK IN KONDENSIRTER MATERIE*. Institut für Festkörperforschung, Forschungszentrum Jülich, (2010). 17, 18
- [Schneider12] C M Schneider, C Wiemann, M Patt, V Feyer, L Plucinski, I P Krug, M Escher, N Weber, M Merkel, O Renault, et al. *Expanding the view into complex material systems: From micro-ARPES to nanoscale HAXPES*. *J. Electron. Spectrosc. Relat. Phenom.* 185(10), 330 (2012). 26, 48
- [Scholl97] A Scholl, L Baumgarten, R Jacquemin, and W Eberhardt. *Ultrafast spin dynamics of ferromagnetic thin films observed by fs*

- spin-resolved two-photon photoemission*. Phys. Rev. Lett. **79**(25), 5146 (1997). 7
- [Shalaev96] V M Shalaev, C Douketis, T Haslett, T Stuckless, and M Moskovits. *Two-photon electron emission from smooth and rough metal films in the threshold region*. Phys. Rev. B: Condens. Matter **53**(16), 11193 (1996). 80
- [Siwick02] B J Siwick, J R Dwyer, R E Jordan, and R J D Miller. *Ultrafast electron optics: Propagation dynamics of femtosecond electron packets*. J. Appl. Phys. **92**(3), 1643 (2002). 86
- [SLAC] *SLAC User FAQ*. https://portal.slac.stanford.edu/sites/lclscore_public/Lists/LCLS_FAQ/FAQ.aspx. [accessed 04-Mar-2015]. 33
- [SLS] *SLS FEMTO parameters*. <http://www.psi.ch/femto/femto-endstation>. [accessed 04-Mar-2015]. 33
- [Smith71] N V Smith. *Photoemission properties of metals*. Crit. Rev. Solid State Mater. Sci. **2**(1), 45 (1971). 17
- [Srinivasan03] R Srinivasan, V A Lobastov, C-U Ruan, and A H Zewail. *Ultrafast electron diffraction (UED)*. Helv. Chim. Acta **86**(6), 1761 (2003). 69
- [Stamm07] C Stamm, T Kachel, N Pontius, R Mitzner, T Quast, K Holldack, S Khan, C Lupulescu, E F Aziz, M Wietstruk, et al. *Femtosecond modification of electron localization and transfer of angular momentum in nickel*. Nat. Mater. **6**(10), 740 (2007). 7
- [Stamm10] C Stamm, N Pontius, T Kachel, M Wietstruk, and H A Dürr. *Femtosecond x-ray absorption spectroscopy of spin and orbital angular momentum in photoexcited Ni films during ultrafast demagnetization*. Phys. Rev. B: Condens. Matter **81**(10), 104425 (2010). 6, 7
- [Stanciu07] C D Stanciu, F Hansteen, A V Kimel, A Kirilyuk, A Tsukamoto, A Itoh, and T Rasing. *All-optical magnetic recording with circularly polarized light*. Phys. Rev. Lett. **99**(4), 047601 (2007). 6
- [Stöhr07] J Stöhr and H C Siegmann. *Magnetism: from fundamentals to nanoscale dynamics*, volume 152. Springer, (2007). 11, 16

BIBLIOGRAPHY

- [Strocov96] V N Strocov, H I Starnberg, and P O Nilsson. *Mapping the excited-state bands above the vacuum level with VLEED: principles, results for Cu, and the connection to photoemission*. J. Phys.: Condens. Matter 8(41), 7539 (1996). 24
- [Tamura86] E Tamura and R Feder. *Theory of spin-polarized secondary-electron emission from ferromagnets*. Phys. Rev. Lett. 57(6), 759 (1986). 30
- [Tanuma11] S Tanuma, C J Powell, and D R Penn. *Calculations of electron inelastic mean free paths. IX. Data for 41 elemental solids over the 50 eV to 30 keV range*. Surf. Interface Anal. 43(3), 689 (2011). 22
- [Teichmann15] M Teichmann, B Frietsch, K Döbrich, R Carley, and M Weinelt. *Transient band structures in the ultrafast demagnetization of ferromagnetic gadolinium and terbium*. Phys. Rev. B: Condens. Matter 91(1), 014425 (2015). 7
- [Tillmann89] D Tillmann, R Thiel, and E Kisker. *Very-low-energy spin-polarized electron diffraction from Fe (001)*. Z. Phys. B: Condens. Matter 77(1), 1 (1989). 30
- [Töws15] W Töws and G M Pastor. *Many-body theory of ultrafast demagnetization and angular momentum transfer in ferromagnetic transition metals*. arXiv preprint arXiv:1508.00983 (2015). 6
- [Tudosa04] I Tudosa, C Stamm, A B Kashuba, F King, H C Siegmann, J Stöhr, G Ju, B Lu, and D Weller. *The ultimate speed of magnetic switching in granular recording media*. Nature 428(6985), 831 (2004). 5
- [Turgut13] E Turgut, J M Shaw, P Grychtol, H T Nembach, D Rudolf, R Adam, M Aeschlimann, C M Schneider, T J Silva, M M Murnane, et al. *Controlling the competition between optically induced ultrafast spin-flip scattering and spin transport in magnetic multilayers*. Phys. Rev. Lett. 110(19), 197201 (2013). 7
- [Tusche11] C Tusche, M Ellguth, AA Ünal, C-T Chiang, A Winkelmann, A Krasnyuk, M Hahn, G Schönhense, and J Kirschner. *Spin resolved photoelectron microscopy using a two-dimensional spin-polarizing electron mirror*. Appl. Phys. Lett. 99(3), 032505 (2011). 32

- [Vahaplar09] K Vahaplar, A M Kalashnikova, A V Kimel, D Hinzke, U Nowak, R Chantrell, A Tsukamoto, A Itoh, A Kirilyuk, and T Rasing. *Ultrafast path for optical magnetization reversal via a strongly nonequilibrium state*. Phys. Rev. Lett. **103**(11), 117201 (2009). 5
- [Vasilyev15] D Vasilyev, C Tusche, F Giebels, H Gollisch, R Feder, and J Kirschner. *Low-energy electron reflection from Au-passivated Ir (001) for application in imaging spin-filters*. J. Electron. Spectrosc. Relat. Phenom. **199**, 10 (2015). 32
- [Vodungbo11] B Vodungbo, A Barszczak Sardinha, J Gautier, G Lambert, C Valentin, M Lozano, G Iaquaniello, F Delmotte, S Sebban, J Lüning, et al. *Polarization control of high order harmonics in the EUV photon energy range*. Opt. Express **19**(5), 4346 (2011). 33
- [von Witzleben15] M von Witzleben. *Element-selective studies of magnetization dynamics in Ni_xPd_{1-x} -alloys*. Master's thesis, RWTH Aachen University, (2015). 92, 93
- [Wallauer96] W Wallauer and T Fauster. *Exchange splitting of image states on Fe/Cu (100) and Co/Cu (100)*. Phys. Rev. B: Condens. Matter **54**(7), 5086 (1996). 47, 76, 78
- [Wang15] H Wang, Y Xu, S Ulonska, P Ranitovic, J S Robinson, and R A Kaindl. *Bright high-repetition-rate source of narrowband extreme-ultraviolet harmonics beyond 22 eV*. Nat. Commun. **6**, 7459 (2015). 68
- [Weber11] A Weber, F Pressacco, S Günther, E Mancini, P M Oppeneer, and C H Back. *Ultrafast demagnetization dynamics of thin Fe/W (110) films: Comparison of time-and spin-resolved photoemission with time-resolved magneto-optic experiments*. Phys. Rev. B: Condens. Matter **84**(13), 132412 (2011). 8
- [Weier15] C Weier. *Resonant Magnetic Scattering Studies using Synchrotron Radiation and Laser-Generated Extreme Ultraviolet Light*. PhD thesis, Universität Duisburg-Essen, (2015). 43
- [Williams01] G P Williams. *X-ray data booklet*. X-RAY DATA BOOKLET (2001). 48
- [Winkelmann08] A Winkelmann, D Hartung, H Engelhard, C-T Chiang, and J Kirschner. *High efficiency electron spin polarization analyzer*

BIBLIOGRAPHY

- based on exchange scattering at Fe/ W (001). *Rev. Sci. Instrum.* **79**(8), 083303 (2008). 51, 52
- [Winterfeldt06] C Winterfeldt. *Generation and control of high-harmonic radiation*. PhD thesis, Julius-Maximilians-Universität Würzburg, (2006). 34
- [Yen80] R Yen, J Liu, and N Bloembergen. *Thermally assisted multiphoton photoelectric emission from tungsten*. *Opt. Commun.* **35**(2), 277 (1980). 78, 79, 82
- [Zayets12] V Zayets, H Saito, K Ando, and S Yuasa. *Optical isolator utilizing surface plasmons*. *Materials* **5**(5), 857 (2012). 79
- [Zhang00] G P Zhang and W Hübner. *Laser-induced ultrafast demagnetization in ferromagnetic metals*. *Phys. Rev. Lett.* **85**(14), 3025 (2000). 6
- [Zhao12] K Zhao, Q Zhang, M Chini, Y Wu, X Wang, and Z Chang. *Tailoring a 67 attosecond pulse through advantageous phase-mismatch*. *Opt. Lett.* **37**(18), 3891 (2012). 33
- [Zhou05] X J Zhou, B Wannberg, W L Yang, V Brouet, Z Sun, J F Douglas, D Dessau, Z Hussain, and Z-X Shen. *Space charge effect and mirror charge effect in photoemission spectroscopy*. *J. Electron. Spectrosc. Relat. Phenom.* **142**(1), 27 (2005). 69, 70, 73

Publications and Conference Contributions

- 2016 Review of Scientific Instruments (Article)
Spin-resolved photoelectron spectroscopy using femtosecond extreme ultraviolet light pulses from high-order harmonic generation
M. Plötzing, R. Adam, C. Weier, L. Plucinski, S. Eich, S. Emmerich, M. Rollinger, M. Aeschlimann, S. Mathias, C. M. Schneider
Rev. Sci. Instrum. **87**(4), 043903 (2016)
- 2016 DPG Spring meeting, Regensburg (Talk)
Ultrafast Demagnetization in Co studied with Time-, Energy- and Spin-resolved Photoemission
- 2015 Ultrafast Magnetism Conference, Nijmegen (Talk)
Ultrafast electron- and spin-dynamics in the band structure of Co/Cu(001)
- 2015 RACIRI Summer School, Rügen (Poster)
Spin- and Time-resolved Photoelectron Spectroscopy with Extreme Ultraviolet Pulses from High-order Harmonic Generation
- 2014 DPG Spring meeting, Dresden (Talk)
Spin-resolved photoelectron spectroscopy using femtosecond extreme ultraviolet light pulses
- 2013 DPG Spring meeting, Regensburg (Poster)
A highly efficient spin-resolved photoelectron spectroscopy experiment
- 2012 DPG Spring meeting, Berlin (Poster)
Ultrafast Demagnetization Dynamics in $Ni_{1-x}Pd_x$ alloys

Curriculum Vitae

Personal Details

| | |
|-----------------|---------------------------|
| Name: | Moritz Alexander Plötzing |
| Date of Birth: | 9th October 1985 |
| Place of Birth: | Euskirchen, Germany |

Education

| | |
|-------------|--|
| Since 2011 | PhD student at University of Duisburg-Essen and Forschungszentrum Jülich, PGI-6 Subject: <i>Laser-Induced Ultrafast Electron- and Spin-Dynamics in the Electronic Band Structure of Co(001)</i> |
| 2005 - 2011 | Academic Studies of Physics at RWTH Aachen University |
| 2011 | Diplom |
| 2010 - 2011 | Diplomarbeit at Forschungszentrum Jülich, PGI-6 Subject: <i>Ultrafast Demagnetization Dynamics in NiPd alloys</i> |
| 2008 - 2009 | Year Abroad at Queen Mary, University of London |
| 1996 - 2005 | St.-Michael-Gymnasium, Bad Münstereifel |
| 2005 | Abitur |

CURRICULUM VITAE

Additional Activities

- | | |
|-------------|--|
| 2008 - 2009 | Final Year Project in the Master's Program of Queen Mary Subject: <i>Charge transport in organic semiconductors</i> |
| 2007 - 2008 | Student Assistant at the "Institut für Stromrichtertechnik und Elektrische Antriebe (ISEA)" at RWTH Aachen University Subject: <i>Lead battery technology and redox-flow-cells</i> |
| 1999 - 2004 | Several participations and prices in "Jugend forscht" |
| 2004 | 1st price in the national final for the best interdisciplinary study |

Hiermit erkläre ich, dass ich die vorliegende Arbeit selbstständig und ohne fremde Hilfe verfasst habe. Ferner habe ich außer den angegebenen Quellen keine anderen Hilfsmittel benutzt. Die dem Sinn oder Wortlaut nach entnommenen Textpassagen oder Abbildungen habe ich in jedem Einzelfall kenntlich gemacht. Dieser Dissertation geht weder ein erfolgloser Promotionsversuch voraus, noch wurde sie in einem weiteren Promotionsverfahren eingereicht. Abgesehen von den angegebenen Publikationen sind die Ergebnisse dieser Dissertation unveröffentlicht. Diese Dissertation, die den Doktorgrad "Dr. rer. nat." anstrebt, wurde von Prof. Dr. C. M. Schneider betreut.

Jülich, den 17.12.2015

Moritz Plötzing

Acknowledgements

I would like to express my sincere thanks and appreciation to everyone who made this work possible and the last years an enjoyable time. In particular, I am deeply grateful to:

Prof. **Claus M. Schneider** for giving me the opportunity to do my PhD at his institute, which provided an excellent environment for my research. Thank you for supervising and personally supporting my project and always having an open door.

Prof. **Stefan Mathias** for making the fruitful collaboration with the TU Kaiserslautern possible, for offering to review my work and for his very helpful input during the measurements and discussions.

Dr. **Roman Adam** for accepting me in his group and fostering close relations with the team that also continued outside work. He supervised my research and not only gave essential advice throughout the entire project but also joined me in the lab and proofread the thesis on short notice. Thank you for all the support!

Dr. **Lukasz Plucinski** for his help with the photoemission part of my work. Thank you for introducing me into photoelectron spectroscopy and sharing your knowledge in countless discussions.

I would also like to give a special thanks to Dr. **Christian Weier** for making the work in the laser lab great fun. His efforts and patience in "training the Dragon" were crucial for this work!

Steffen Eich, **Sebastian Emmerich** and **Markus Rollinger** for the stressful, but funny day and night shifts and for always keeping the motivation up during the magnetization dynamics measurements. Furthermore, I am very grateful to the people at the TU Kaiserslautern who made me feel very welcome whenever I visited them and in particular to Prof. **Martin Aeschlimann** for giving me the opportunity to conduct experiments in his labs.

ACKNOWLEDGEMENTS

Bernd Küpper for introducing me to all vacuum-related technology, for his help especially during the first month of my PhD, and for always finding quick solutions for technical problems. Without him, the development and commissioning of the experiment would have been impossible. Thank you!

Jürgen Lauer for writing the measurement software, implementing all desired features, fixing every bug and solving any computer issues.

Heinz Pfeifer, Arnd Bremen and the PGI workshop for greatly mastering all other technical challenges.

Dr. Lukasz Plucinski, Markus Eschbach, Dr. Christian Weier, Marten Patt, Christoph Schmitz, Dr. Carsten Wiemann, Moritz von Witzleben, Markus Rollinger, and Steffen Eich for the helpful feedback and comments on all drafts of the thesis. Thank you for investing your time!

I would also like to thank all members of the PGI-6, the laser group and especially the "Kaffeerunde". The nice atmosphere in Jülich will make this time unforgettable!

My final, special thanks go to all my friends and, in particular, to Sarah and to my family for their general, invaluable support.

Band / Volume 117

First-principles investigation of inelastic magnetic excitations in nanostructures deposited on surfaces

B. J. Schweflinghaus (2016), v, 204 pp

ISBN: 978-3-95806-115-6

Band / Volume 118

Magnetic, structural, and electronic properties of NiFe₂O₄ ultrathin films

M. Hoppe (2016), vii, 118 pp

ISBN: 978-3-95806-122-4

Band / Volume 119

First-principle investigation of displacive response in complex solids

D. A. Klüppelberg (2016), xi, 179 pp

ISBN: 978-3-95806-123-1

Band / Volume 120

Beam Cooling at COSY and HESR – Theory and Simulation – Part 1 Theory

H. Stockhorst, T. Katayama and R. Maier (2016), v, 192 pp

ISBN: 978-3-95806-127-9

Band / Volume 121

Scanning tunneling microscopy of single-molecule magnets and hybrid-molecular magnets: Two approaches to molecular spintronics

V. Heß (2016), x, 127 pp

ISBN: 978-3-95806-128-6

Band / Volume 122

Bulk and surface sensitive energy-filtered photoemission microscopy using synchrotron radiation for the study of resistive switching memories

M. C. Patt (2016), viii, 247 pp

ISBN: 978-3-95806-130-9

Band / Volume 123

Group IV Epitaxy for Advanced Nano- and Optoelectronic Applications

S. Wirths (2016), vi, 116, XXX pp

ISBN: 978-3-95806-132-3

Band / Volume 124

Strained Silicon-Germanium/Silicon Heterostructure Tunnel FETs for Low Power Applications

S. Blaeser (2016), iv, 91, xvii pp

ISBN: 978-3-95806-135-4

Band / Volume 125

Nanocavity Arrays for Extracellular Recording and Stimulation of Electroactive Cell Systems

A. Czeschik (2016), x, 162 pp

ISBN: 978-3-95806-144-6

Band / Volume 126

Band Structure Engineering in 3D Topological Insulators Investigated by Angle-Resolved Photoemission Spectroscopy

M. Eschbach (2016), VIII, 153 pp

ISBN: 978-3-95806-149-1

Band / Volume 127

Dynamics in colloid and protein systems: Hydrodynamically structured particles, and dispersions with competing attractive and repulsive interactions

J. Riest (2016), ix, 226 pp

ISBN: 978-3-95806-153-8

Band / Volume 128

Self-purifying $\text{La}_{2/3}\text{Sr}_{1/3}\text{MnO}_3$ epitaxial films: Observation of surface precipitation of Mn_3O_4 particles for excess Mn ratios

A. Steffen (2016), 154 pp

ISBN: 978-3-95806-162-0

Band / Volume 129

Strain and electric field mediated manipulation of magnetism in $\text{La}_{(1-x)}\text{Sr}_x\text{MnO}_3/\text{BaTiO}_3$ heterostructures

M. Schmitz (2016), VI, 141 pp

ISBN: 978-3-95806-164-4

Band / Volume 130

High-Throughput Live-Cell Imaging for Investigations of Cellular Heterogeneity in *Corynebacterium glutamicum*

S. Helfrich (2016), xvi, 217 pp

ISBN: 978-3-95806-167-5

Band / Volume 131

Laser-Induced Ultrafast Electron- and Spin-Dynamics in the Electronic Band Structure of $\text{Co}(001)$

M. A. Plötzing (2016), ii, 109, XXXIV pp

ISBN: 978-3-95806-168-2

Weitere *Schriften des Verlags im Forschungszentrum Jülich* unter
<http://www.zb1.fz-juelich.de/verlagextern1/index.asp>

Schlüsseltechnologien /
Key Technologies
Band / Volume 131
ISBN 978-3-95806-168-2

